Analysis of the Semileptonic Decay $D^0 \to \overline{K}^0 \pi^- \mu^+ \nu$

by

Ilaria Maria Lucia Segoni

Laurea in Physics, Pavia University, 2000

A thesis submitted to the

Faculty of the Graduate School of the

University of Colorado in partial fulfillment

of the requirements for the degree of

Doctor of Philosophy

Department of Physics

2004

This thesis entitled:
Analysis of the Semileptonic Decay $D^0 \to \overline{K}^0 \pi^- \mu^+ \nu$
written by Ilaria Maria Lucia Segoni
has been approved for the Department of Physics

Prof. John P. Cumalat

Prof. William T. Ford

Date

The final copy of this thesis has been examined by the signatories, and we find that both the content and the form meet acceptable presentation standards of scholarly work in the above mentioned discipline.

Segoni, Ilaria Maria Lucia (Ph.D., Physics)

Analysis of the Semileptonic Decay $D^0 \to \overline{K}^0\pi^-\mu^+\nu$

Thesis directed by Prof. John P. Cumalat

This thesis describes the analysis of the semileptonic decay $D^0 \to \overline{K}^0\pi^-\mu^+\nu$ using FOCUS data. FOCUS is a fixed target experiment at Fermilab that studies the physics of the charm quark. Particles containing charm are produced by photon–gluon fusion from the collision of a photon beam on a BeO target. The experiment is characterized by excellent vertex resolution and particle identification. The spectrometer consists of three systems for track reconstruction (two silicon systems and one multiwire proportional chamber system) and two magnets of opposite polarity. The polarity of the magnet is such that the events of e^+e^- pairs produced in the target (which constitutes the main background) travel through a central opening in the detectors without interactions. Particle momentum is measured from the deflection angle in the magnets. Three multi–cell Čerenkov counters are used for charged particle identification (for e, π, K, and p). Two different tracking systems located after several interaction lengths of shielding material are used for muon identification. The energy of neutral pions and electrons is measured in two electromagnetic calorimeters, while an hadron calorimeter is used for measuring the neutron energy.

During the last four years the FOCUS collaboration provided results on several charm topics: CP violation, D^0–$\overline{D}^0$ mixing, rare and forbidden decays, precision measurements of semileptonic decays, baryon and meson lifetimes, fully hadronic baryon and meson branching ratios, charm spectroscopy, Dalitz analyses of resonant structures, charm anti–charm production, QCD studies involving double charm particles, and pentaquarks.

Semileptonic decays, besides having a clear signature for experiments, provide crucial information for theoretical studies. These decays carry information on the weak coupling of quarks since they can be used for measuring Cabibbo–Kobayashi–Maskawa matrix elements. Although the decay occurs through weak interaction, QCD effects due to quark confinement affect the decay amplitude. These effects can be included through the form factors, which are predicted by different theoretical approaches (quark models, lattice QCD, and sum rules). Experiments can measure form factor ratios, and from the comparison with theory they provide guidance for building a successful theory to describe hadrons.

In this thesis we present the first measurement of the form factor ratios r_v and r_2 for the decay $D^0 \to \overline{K}^0\pi^-\mu^+\nu$. We use a model where the $\overline{K}^0\pi^-$ system is described by a spin 1 component, the $K^*(892)^-$, interfering with a small S-wave component of constant amplitude and phase ($Ae^{i\delta}$). This model was introduced by FOCUS for the analysis of the decay $D^+ \to K^-\pi^+\mu^+\nu$. We measure:

$$r_v = 1.71 \pm 0.68 \pm 0.34 \tag{1}$$

$$r_2 = 0.91 \pm 0.37 \pm 0.10 \tag{2}$$

where the first error is statistical and the second is systematic. After determining the form factor ratios, we measure the amplitude A of the S-wave component. Our sensitivity to the S-wave phase is very limited. Based on isospin symmetry we fix the phase to the value measured by FOCUS for the $D^+ \to K^-\pi^+\mu^+\nu$ decay ($\delta = 0.68$). We measure the amplitude to be:

$$A = 0.35 \pm 0.22 \pm 0.05 \text{ GeV}^{-1} \tag{3}$$

Finally, we measure the exclusive branching ratio $\Gamma(D^0 \to K^*(892)^-\mu^+\nu)/\Gamma(D^0 \to \overline{K}^0\pi^-\pi^+)$ to be:

$$\frac{\Gamma(D^0 \to K^*(892)^-\mu^+\nu)}{\Gamma(D^0 \to \overline{K}^0\pi^-\pi^+)} = 0.337 \pm 0.034 \pm 0.013 \tag{4}$$

None of the measurements presented in this thesis have ever been reported before nevertheless it is possible to determine the expected values. Based on isospin symmetry, the form factor ratios and the S-wave amplitude for the decay we study in this thesis should have the same value as for the decay $D^+ \to K^-\pi^+\mu^+\nu$. There are several measurements of r_v and r_2 for this decay, and in all cases our result is in excellent agreement. The amplitude of the S-wave for the D^+ decay has been measured only by FOCUS. Also in this case the agreement with our measurement is very good. We evaluate the expected value for the branching ratio using results from the CLEO collaboration for the semielectronic channel and using isospin symmetry. This last estimate is derived from the following equality:

$$\frac{\Gamma(D^0 \to K^{*-}\mu^+\nu)}{\Gamma(D^0 \to \overline{K^0}\pi^-\pi^+)} = \frac{\Gamma(D^+)}{\Gamma(D^0)} \times \frac{\Gamma(D^+ \to K^{*0}\mu^+\nu)}{\Gamma(D^+ \to K^-\pi^+\pi^+)} \times \frac{\mathcal{B}(D^+ \to K^-\pi^+\pi^+)}{\mathcal{B}(D^0 \to \overline{K^0}\pi^-\pi^+)}$$

where we use the FOCUS measurement of the semileptonic branching ratio $\Gamma(D^+ \to K^*(892)^0\mu^+\nu)/\Gamma(D^+ \to K^-\pi^-\pi^+)$ and of the D meson lifetimes. For the branching ratio also we find excellent agreement with the expected values.

To my family

Acknowledgements

I would like to thank all the people that helped me and cared for me during these four years in Colorado, and there are many.

The FOCUS collaboration is made up of great people that are at the same time bright scientists and people that are a lot of fun to be with. First of all I want to give a big hug to the Colorado group, with I always felt at ease with and that provides for a wonderful learning environment for a physics student. A lot of thanks to John Cumalat, my advisor, who is a great physicist and group leader, and a person that cares very much for his students and their future. I'd also like to thank John's family, Anita and John Jr., for receiving me in their home on occasion of many nice parties. While I was here many other people have been part of this group. I'd like to thank them all for their friendship and all what I learned working with them: Brian, Caterina, Eduardo, and Kevin. I was happy also to meet with the many visitors we had here: Alberto, Andre, Ignacio, Salvador & Fabiola, and Will. I'd like to thank Will also for the useful discussions on semileptonic decays.

I owe many thanks also to the other FOCUS collaborators: the Pavia group, where I started this journey; Harry Cheung, for being a great teacher and friend while I was at Fermilab; Jim Wiss, who provided a lot of guidance for my thesis work and a lot of fun playing tennis table at the FNAL user's center. Thanks for showing so much care towards FOCUS students to Daniele and Phil. During these years I visited the FOCUS institutions in Brazil, Frascati, Mexico, Puerto Rico, and Tennessee. I'd like to thank

the hosts, it was a pleasure to be visiting you.

I'd like to thank all the friends that I met here, in particular Andrei, Delia, Dafne, Eli, and Stefan. Unfortunately everybody is coming and going, but I am sure that we'll keep in touch. I'd also like to thank my piano teacher, Lisa, I wish I met her much earlier than I did, she is simply awesome!

This thesis is dedicated to my family, mom, dad, and Francesco. They never showed any doubts about my decision of moving so far for so long because they always trusted my judgment, I can feel that, and it's the greatest form of support a family can give.

A lot of thanks also to Lorenzo's family, Ausilia, Eugenio, Celina, and Melissa. You received me warmly since the beginning, eight years ago.

Besides my family, the other greatest supporter I've ever had is Lorenzo. He believes in me more than me! I'm so happy we did this together, so much awaits us....

Grazie di cuore a tutti voi.

Contents

Chapter

Tables

Table

Figures

Figure

Chapter 1

Theoretical Overview

1.1 The Standard Model of Elementary Particles

The Standard Model [1, 2] describes particles and their strong and electroweak interactions. It is currently the model that best describes such phenomena, but it is incomplete in the sense that it requires external input for several parameters that cannot be derived from first principles. New, more self contained models and theories are being developed. Some are extensions to the Standard Model (e.g. the Super Symmetric Standard Model [3]), some are new theories (e.g. the String Theory [4]).

In the Standard Model matter is formed by two species of fundamental particles with 1/2 spin (particles with half integer spin are called *fermions*): leptons and quarks. Both species are divided into three families. For the leptons:

$$\begin{pmatrix} e \\ \nu_e \end{pmatrix}, \begin{pmatrix} \mu \\ \nu_\mu \end{pmatrix}, \begin{pmatrix} \tau \\ \nu_\tau \end{pmatrix}$$

while for the quarks:

$$\begin{pmatrix} u \\ d' \end{pmatrix}, \begin{pmatrix} c \\ s' \end{pmatrix}, \begin{pmatrix} t \\ b' \end{pmatrix}$$

The index $'$ for the "down" type quarks will be explained later. In units of the absolute value of the electron charge, the "up" type leptons (electron, muon and tau)

have charge -1, while the neutrinos have zero charge; the "up" type quarks (up, charm, top) have charge 2/3 while the "down" type quarks (down, strange and bottom) have charge -1/3. The fundamental particles interact through exchange of intermediate particles with integer spin (particles with integer spin are called *bosons*). The intermediate bosons for each interaction are listed along with their properties in Table 1.1.

Intermediate Bosons

Interaction	Boson	Spin	charge	Mass (GeV/c^2)
Weak	$W^{\pm}$	1	± 1	80.425 ± 0.038
"	Z^0	1	0	91.1876 ± 0.0021
Electromagnetic	γ	1	0	0
Strong	g	1	0	0

Table 1.1: Summary of the Properties of the Intermediate Bosons for each interaction. The gluon mass is a theoretical value, a mass of a few MeV/c^2 is not precluded.

For the listing of the intermediate bosons the electroweak interaction has been "split" into the electromagnetic and the weak interactions. In the Standard Model the electroweak interaction is described by a quantum field theory based on a symmetry group for the Lagrangian (the same applies to the strong interaction description). The symmetry is spontaneously broken at low energies, and the interaction occurs in the two different components (electric and weak). Due to the success in the theoretical studies that resulted in the electroweak unification, there are many efforts to investigate the possibility of a description of all the known interactions (strong, electroweak and gravitational interaction) as different manifestations, due to spontaneous symmetry breaking, of the same interaction (Grand Unified Theory [5]).

While the W and Z bosons couple to all fundamental fermions, the photon only couples to fermions with non–zero electric charge, and the gluon only couples to the quarks. Only quarks contain the strong charge, called *color* (six colors exist: *red*, *blue*, *green* and their respective anti–colors). In nature the quarks are confined through the strong interaction in bound states called *hadrons*. The strong coupling between two

quarks increases with the separation distance between the two. As a system of two quarks is being divided (for instance in an accelerator machine), the gluon field between the two quarks increases in strength, and eventually new hadrons are formed with the new quarks that are being created. For this reason no quark (or color–charged particle) has been observed in nature. The hadrons occur in two types, both with zero net color charge: the *mesons* (bound state of a quark and an anti–quark with given color and its anti–color) and the *baryons* (bound state of three quarks with three colors).

In the Standard Model all of the interactions occur within each family. While d', s' and b' are eigenstates for the strong interaction, a rotation in the flavor space is necessary to find the weak eigenstates u, s and d. The rotation is performed through the Cabibbo–Kobayashi–Maskawa (CKM) matrix [6]:

$$\begin{pmatrix} d' \\ s' \\ b' \end{pmatrix} = \begin{pmatrix} V_{ud} & V_{us} & V_{ub} \\ V_{cd} & V_{cs} & V_{cb} \\ V_{td} & V_{ts} & V_{tb} \end{pmatrix} \begin{pmatrix} d \\ s \\ b \end{pmatrix} \tag{1.1}$$

The electroweak interaction therefore couples quarks of the three families:

$$\begin{pmatrix} u \\ d \end{pmatrix}, \begin{pmatrix} c \\ s \end{pmatrix}, \begin{pmatrix} t \\ b \end{pmatrix}$$

and the coupling (whose intensity is given by $|V_{qq'}|^2$) can occur also between quarks of different families (for instance the amplitude for the decay $c \to W^+ d$ is proportional to $|V_{cd}|^2$). The off diagonal elements are much smaller than the diagonal ones (which are close to $\sim$1), therefore decays within the same family are favored over decays that change family. A similar description for the mixing between lepton families is currently under investigation. The neutrino mass measurements are crucial in this field, as non–zero masses are required to allow for mixing.

Table 1.1 summarizes other properties of the fundamental fermions: the mass,

the lepton number, and the baryon number. These last two are conserved quantities in the Standard Model.

Fundamental Fermions

Fermion	Mass	Lepton Number	Baryon Number
e	0.511 MeV/c^2	1	0
μ	105.6 MeV/c^2	1	0
τ	1777 MeV/c^2	1	0
ν_e	<3 eV/c^2	1	0
ν_μ	<0.19 MeV/c^2	1	0
ν_τ	<18.2 MeV/c^2	1	0
u	1.5–4.0 MeV/c^2	0	1/3
d	4–8 MeV/c^2	0	1/3
c	1.15–1.35 GeV/c^2	0	1/3
s	80–130 MeV/c^2	0	1/3
t	174.3±5.1 GeV/c^2	0	1/3
b	4.1–4.9 GeV/c^2	0	1/3

Table 1.2: Summary of the Properties of Leptons and Quarks

1.2 Weak Decay of Charmed Mesons

The weak decay of hadrons occurs through the conversion of a quark within the hadron into a lighter quark and a W. The first weak interaction ever observed is the nuclear β decay. This observation marked the discovery of weak interactions and led to the discovery of the neutrino particle. The underlying process of this decay, where a neutron (udd) within an atomic nucleus decays into a proton (uud) and an $e^-\bar{\nu}_e$ pair, occurs through the conversion of a d quark into an u quark and a W^-: $(udd) \rightarrow (uud)W^-$ (and $W^- \rightarrow e^-\bar{\nu}_e$).

In this thesis we study the decay of the meson D^0 (the ground state of the $c\overline{u}$ system) into a final state that contains a mixture of hadrons and leptons (semileptonic decay): $D^0 \rightarrow \overline{K}^0\pi^-\mu^+\nu$. In analogy to the nuclear β decay, this decay occurs through the conversion of the c quark into an s quark and a W^+. Figure 1.1 shows some possible mechanisms for the D meson decays: *External* and *Internal Spectator* for the

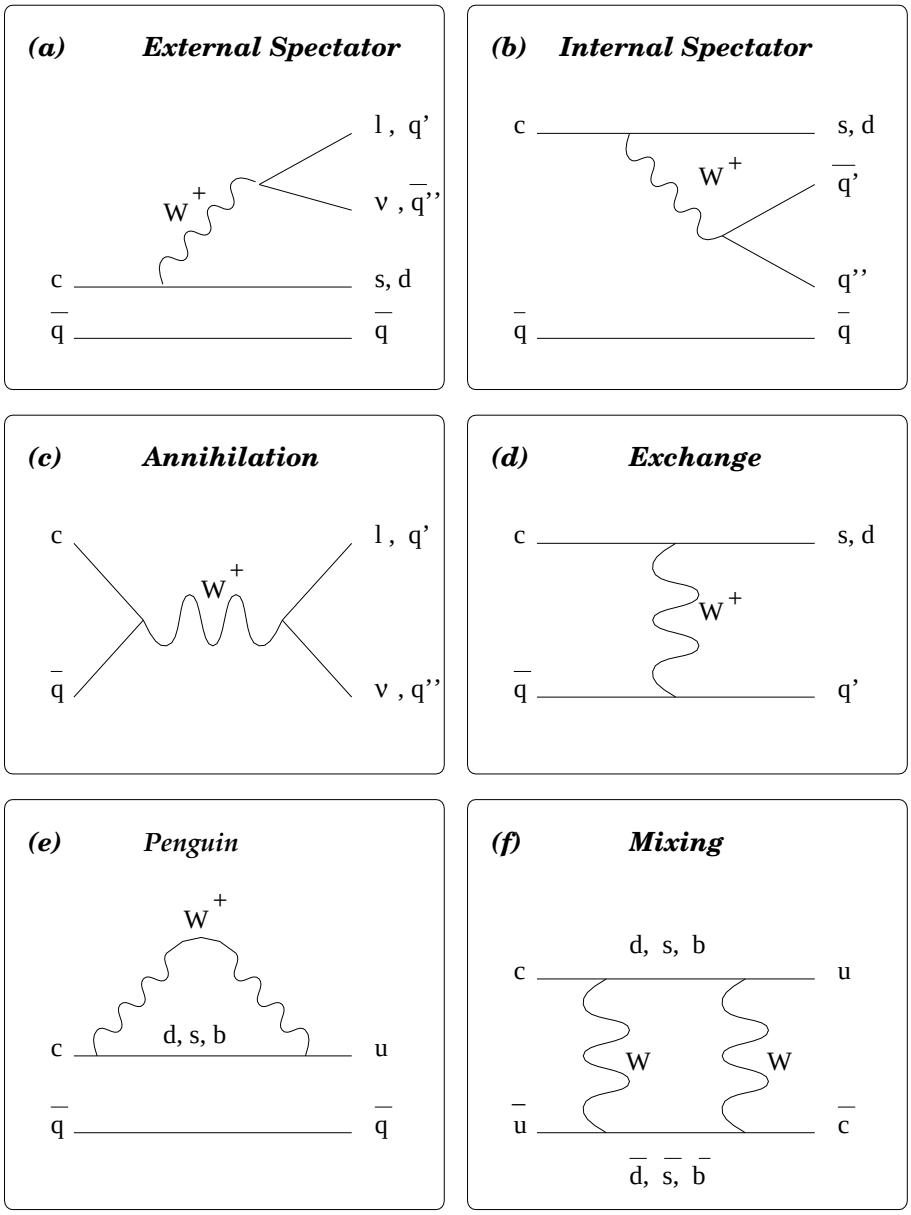

Figure 1.1: Lowest order decay mechanisms for mesons containing a c quark. Semileptonic and leptonic decays can only occur through the External Spectator (a) and Annihilation (c), respectively. The Exchange diagram (d) is suppressed in mesons by a factor $(M_q/M_c)^2$, where q is the light quark from c (either s or u). The mixing mechanism (f) allows for D^0–$\overline{D}^0$ transitions.

tree diagram, *Annihilation*, *Exchange* (which is heavily suppressed in mesons), and *Penguin*. The *Mixing* mechanism, which allows D^0–$\overline{D}^0$ oscillations, is also shown. Since the lepton and baryon numbers must be conserved at each vertex, the semileptonic decay can occur only through *External Spectator* mechanism, while a leptonic decay (where only leptons appear in the final state) can occur only through *Annihilation* mechanism.

The differential decay probability for the decay process can be written using Fermi's golden rule:

$$d\Gamma = \frac{2\pi}{\hbar} |\langle f|M|i\rangle|^2 d\rho_3 \tag{1.2}$$

where the dynamics of the decay are contained in the squared amplitude of the matrix element between the final and the initial states ($|\langle f|M|i\rangle|^2$), and $d\rho_3$, the density of possible final states, contains the kinematic information. The decay amplitude $|M|^2$ can be constructed using the Feynman rules that are derived within a perturbative approach where the transition operator between initial and final states is written as an integral expansion. In this approach the Hamiltonian that describes the free state is perturbed by an interaction Hamiltonian of the form[1] :

$$\mathcal{H}_I \propto g_W \mathcal{J}_\mu \mathcal{W}^\mu \tag{1.3}$$

where $\mathcal{J}_\mu$ is the current of the fermions and $\mathcal{W}^\mu$ is the W field. The order of the expansion is given by the power of the weak coupling constant: $(g_W)^n$. The Feynman rules consist of a prescription of the mathematical terms associated with each element of the decay to construct the decay amplitude. Fig. 1.2 shows a diagram for the decay $c \to sW^+(\mu^+\nu)$. The matrix element between final and initial states is thus written as:

[1] The "interaction operator" perturbative approach was first developed by P.A.M. Dirac in Quantum Electrodynamics, where $\mathcal{H}_I \propto \mathcal{J}_\mu \mathcal{A}^\mu$, J_μ being the leptonic current and A^μ the electromagnetic field.

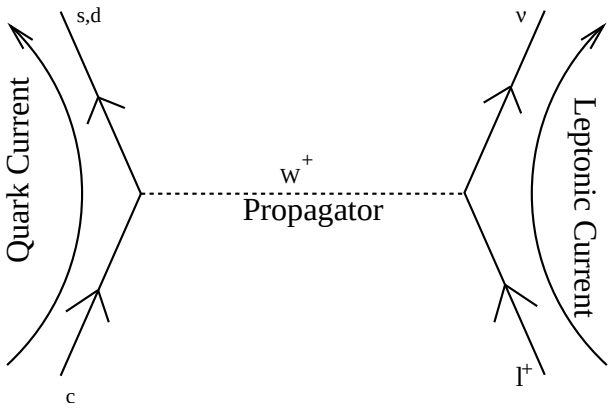

Figure 1.2: A simple schematic for the components of c quark decay is shown.

$$< f|M|i > \sim \underbrace{\overline{u}_c(V_{cs}\frac{-ig_W}{2\sqrt{2}})\gamma^\mu(1-\gamma^5)u_s}_{\text{Quark Current}} \quad \underbrace{\frac{-i(g_{\mu\nu}-q_\mu q_\nu/M_W^2}{q^2-M_W^2}}_{\text{Propagator}} \quad \underbrace{\overline{u}_\ell(\frac{-ig_W}{2\sqrt{2}})\gamma^\nu(1-\gamma^5)u_\nu}_{\text{Leptonic Current}} \tag{1.4}$$

where $q^2 = (P_e + P_\nu)^2$ is the squared mass of the virtual W, q being equal to the four-momentum transferred from the non–leptonic particle in the initial state and the lepton pair in the final state. The currents are built as a vertex factor ($\frac{-ig_W}{2\sqrt{2}}\gamma^\mu(1-\gamma^5)$) between the incoming ($u_p$) and outgoing ($\overline{u}_p$) particles. The quark vertex also includes V_{cs}. There are two important features in this structure. The fermionic currents that couple to the W have a Vector-Axial (V-A) form that reflects the parity non–conservation in weak decays (i.e. the decay is not symmetric with respect to spatial coordinate inversion). The propagator for the virtual W is related to the Fourier transform of a Yukawa potential $V(r) \sim e^{-r\cdot M}/r$, where M is the mass of the exchanged quantum ($M = M_W$). The Fourier transform in four–momentum space is $\sim 1/(q^2 + M_W^2)$. The leptonic and hadronic currents are coupled through the propagator term. If $q^2 << M_W^2$, the propagator assumes the constant form $ig_{\mu\nu}/M_W^2$ and the matrix element can be written as:

$$M = -i\frac{G_F}{\sqrt{2}}V_{cs}\mathcal{L}^{\mu}\mathcal{H}_{\mu} \tag{1.5}$$

where G_F is the Fermi constant. In this approximation[2] the two currents give now completely independent contributions. Complications arise due to the fact that the quarks are confined in the hadron by strong interactions and the hadronic current must be evaluated between hadronic states rather than free quark states:

$$\mathcal{H}_{\mu} = \langle K|J_{\mu}^{HAD}|D\rangle \tag{1.6}$$

The hadronic current cannot be calculated, but it is constructed considering the symmetries of the decay process and using the available four vectors (momenta and polarizations). The current is parameterized through Lorentz invariant coefficients, the *form factors*, that depend on q^2. All the unknown QCD effects are confined to the form factors. Different theoretical approaches (quark models [7, 8, 9, 10, 11, 12, 13], lattice QCD [14, 15, 16, 17, 18], and sum rules [19]) can calculate such coefficients, so from comparison with the experimental measurements, the theoretical techniques that are used in other calculations can be tested. The factorization into two currents is not possible for fully hadronic decays, which are further complicated due to the interactions between the hadrons in the final state (*Final State Interactions*, or FSI). For this reason semileptonic and leptonic decays provide a simple environment for the study of QCD. Experimental study of $D^{0,+}$ semileptonic decays is favored over leptonic decays due to the larger branching fractions[3] .

1.3 The $D^0 \to K^*(892)^-(\overline{K}^0\pi^-)\ell^+\nu$ Decay

We now describe the semileptonic decay $D^0 \to K^*(892)^-(\overline{K}^0\pi^-)\ell^+\nu$, where the vector meson (i.e. spin 1 meson) in the final state decays to a $\overline{K}^0\pi^-$ state. The description applies to any $D \to K^*(K\pi)\ell\nu$ decay.

[2] The approximation is valid in the decay studied for this thesis, since $q^2_{MAX} \simeq 1$ GeV/c^2 $<< M_W^2$.
[3] The rate of leptonic decays is suppressed by a factor proportional to the lepton mass squared.

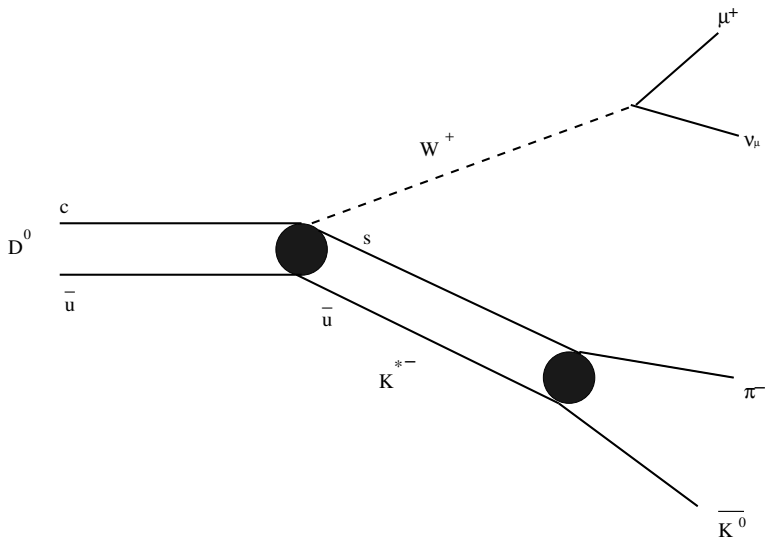

Figure 1.3: Diagram for the decay $D^0 \to \overline{K}^0\pi^-\mu^+\nu$.

1.3.1 The Decay Amplitude

The $D^0 \to K^*(892)^-(\overline{K}^0\pi^-)\ell^+\nu$ decay can be represented by the diagram in Fig. 1.3. The hadronic current $\langle K|V-A|D\rangle$ is constructed using the independent available four vectors of the decay, the D four–momentum P, the K^* four–momentum K, and its polarization ϵ. Only one combination allows us to build the vector component, while there are three ways of building a current with axial properties. For this reason the hadronic current can be parameterized by a "vector" form factor, $V(q^2)$, and three "axial" form factors, $A_{1,2,3}(q^2)$. Following the derivation in [13] (and including the term proportional to m_ℓ^2 that is not included in this reference) we find an expression for the differential decay amplitude on the basis of the four K^* helicity amplitudes $H_{+,-,0,t}$,

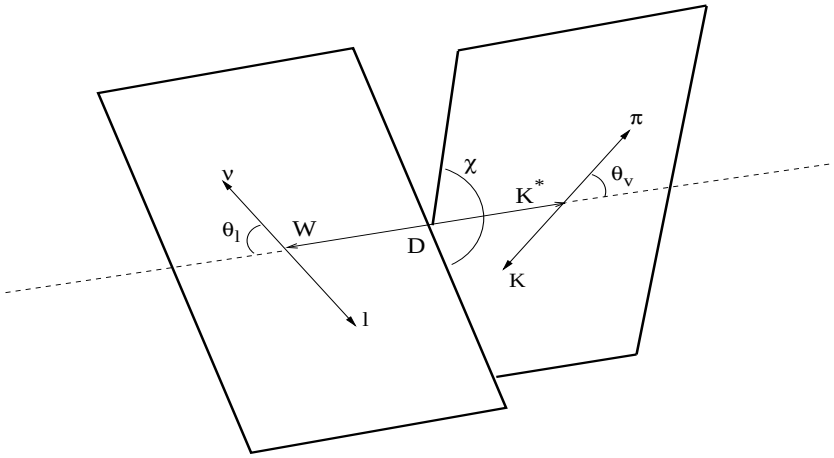

Figure 1.4: Schematic of the decay $D \to K^*\ell^+\nu_\ell$ for the angular variable definitions.

which are linear combinations of V and $A_{1,2,3}(q^2)$:

$$\frac{d^5\Gamma}{dm_{K\pi}dq^2d\cos\theta_V d\cos\theta_\ell d\chi} \sim |\underline{k}|(q^2-m_\ell^2)\{\left|\begin{array}{c}(1+\cos\theta_\ell)\sin\theta_V e^{i\chi}B_{K^{*-}}H_+\\ -(1-\cos\theta_\ell)\sin\theta_V e^{-i\chi}B_{K^{*-}}H_-\\ -2\sin\theta_\ell(\cos\theta_V B_{K^{*-}})H_0\end{array}\right|^2 \tag{1.7}$$

$$+\frac{m_\ell^2}{q^2}\left|\begin{array}{c}\sin\theta_\ell\sin\theta_V B_{K^{*-}}(e^{i\chi}H_+ + e^{-i\chi}H_-)\\ +2\cos\theta_\ell(\cos\theta_V B_{K^{*-}})H_0\\ +2(\cos\theta_V B_{K^{*-}})H_t\end{array}\right|^2\}$$

where $q^2=(P-K)^2=(P_\ell+P_\nu)^2$, $M_{K\pi}=K^\mu K_\mu$, $B_{K^{*-}}$ is a Breit–Wigner distribution that describes the $\overline{K}^0\pi^-$ resonant state, and the three angles, defined in Fig: 1.4 are:

- θ_V: the angle between the $\overline{K}^0$ and the D in the K^* rest frame
- θ_ℓ: the angle between the ℓ^+ and the D in the W rest frame
- χ: the angle between the decay planes of the K^* and the W

As stated before, the form factors $V(q^2)$ and $A_{1,2,3}(q^2)$ are included in the helicity amplitudes:

$$H_{\pm}(q^2) = [(M_D + m_{K\pi})A_1(q^2) \mp \frac{2M_D K}{M_D + m_{K\pi}} V(q^2)] \tag{1.8}$$

$$H_0(q^2) = \frac{1}{2m_{K\pi}\sqrt{q^2}}[(M_D^2 - m_{K\pi}^2 - q^2)(M_D + m_{K\pi})A_1(q^2) - \frac{4M_D^2 K^2}{M_D + m_{K\pi}} A_2(q^2)] \tag{1.9}$$

$$H_t(q^2) = \frac{M_D K}{m_{K\pi}\sqrt{q^2}}[(M_D + m_{K\pi})A_1(q^2) - \frac{M_D^2 - m_{K\pi}^2 + q^2}{M_D + m_{K\pi}} A_2(q^2) + \frac{2q^2}{M_D + m_{K\pi}} A_3(q^2)] \tag{1.10}$$

The dependence of the decay amplitude on the angles θ_V and θ_ℓ can be easily derived in terms of the Wigner d–matrices $d^J_{m_1,m_2}(\cos\theta)$, which express the probability that a spin J has projections m_1 and m_2 along the two directions that define $\cos\theta$. We first determine the angular distribution for the K^* decay, $d^J_{m_1,m_2}(\cos\theta_V)$. The W spin, that defines the spins of the K^* and of the $\ell\nu$ pair, can occur in the three helicity states $m = \vec{p}\cdot\vec{s}/|\vec{p}| = \pm 1, 0$. In order to conserve angular momentum, the K^* must be in the same helicity state, therefore $m_2 = m$, see Fig. 1.5, a). Since the K^* decays into scalars, the spin projection along the pion direction is $m_1 = 0$. The probability for the K^* to be in such state is proportional to $|d^1_{0m}(\cos\theta_V)|^2$. We now move to the W rest frame to determine the dependence on $\cos\theta_\ell$, $d^J_{m_1,m_2}(\cos\theta_\ell)$. We consider the case where the ℓ^+ mass is negligible. Let the W spin be the polarization axis (see Fig. 1.5, b). The W has spin component $m = \pm 1, 0$ along this direction ($m_2 = m$). The neutrino is in a left–handed helicity state, and the charged lepton in our $m_\ell \to 0$ approximation is in a right handed helicity state. For this reason the spin component along the decay axis is $m_1 = 1$, and the decay amplitude of the virtual W is proportional to $|d^1_{1m}(\cos\theta_\ell)|^2$. We have derived the θ_V and θ_ℓ dependence of the decay amplitude for the first term of

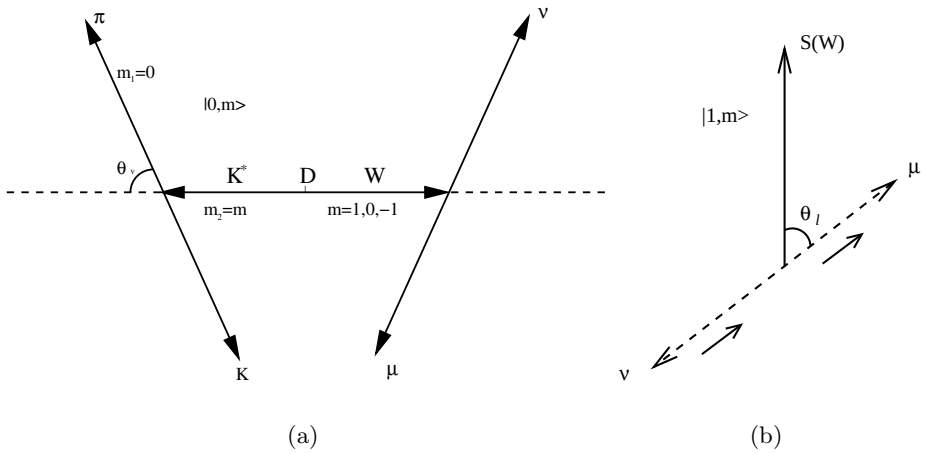

Figure 1.5: Schematic for determining the $\cos\theta_V$ (a) and the $\cos\theta_\ell$ (b) distributions.

Eq. 1.7, where the ℓ^+ is in a right handed helicity state:

$$\frac{d^2\Gamma}{d\cos\theta_V d\cos\theta_\ell} \propto \sum_{m=-1}^{m=1} H_m |d^1_{0m}(\cos\theta_V)|^2 |d^1_{1m}(\cos\theta_\ell)|^2 \tag{1.11}$$

$$\propto \sin^2\theta_V[(1+\cos\theta_\ell)^2 H_+ + (1-\cos\theta_\ell)^2 H_-] + 4\cos^2\theta_V \sin^2\theta_\ell H_0$$

The second term of Eq. 1.7 refers to the case where ℓ^+ is in a left handed helicity state and can be derived with the same procedure. This term is suppressed by a factor m_ℓ^2/q^2, so it is generally negligible when the charged lepton is an electron. This term is taken into account for the decay $D^0 \to K^*(892)^-(\overline{K}^0\pi^-)\mu^+\nu$, where the average q^2 is relatively low and the lepton is a muon[4] .

1.3.2 The Form Factors

The form factor is related to the probability that the quarks in the final states (s and $\overline{u}$ in this case) hadronize. This probability is higher for a small relative velocity between the quarks. This configuration corresponds to maximum q^2. This is easy to picture from figure 1.6 (a). In a simple approximation where we neglect the $\overline{u}$ and we

[4] This term is overwhelmingly important in the semileptonic decays of the B mesons when the charged lepton in the final state is a τ.

imagine the c and s as free quarks, the following holds (in the c rest frame):

$$q^2 = (P_\ell + P\nu)^2 = (P_c - P_s)^2 = M_c^2 + M_s^2 - 2M_c E_s \tag{1.12}$$

so q^2 reaches a maximum when the s momentum is minimum, and this corresponds to a low relative velocity between the s and the $\overline{u}$. The two situations (maximum and minimum q^2) are pictured in Fig. 1.6 b and c. A model that reproduces this behavior is the "vector dominance" model, that uses the pole mass form for the form factors:

$$A_i(q^2) = \frac{A_i(0)}{1 - \frac{q^2}{M_A^2}} \tag{1.13}$$

$$V(q^2) = \frac{V(0)}{1 - \frac{q^2}{M_V^2}} \tag{1.14}$$

This model is based on an approximation where the probability is maximum when the c and s form an excited bound state (with mass $M_{A,V}$) with the same quantum numbers as the W, see Fig 1.7. For the axial and vector component the quantum numbers are $J^P = 1^+$ and $J^P = 1^-$, respectively, so $M_A = M(D_{s1}^+)$=2.5 GeV/c^2 and $M_V = M(D_s^{*+})$=2.1 GeV/c^2. This dependence of the form factors on q^2 is largely used in quark models. With this expression for the form factors, the decay amplitude can be parameterized by $A_1(0)$ and the three ratios $r_v = V(0)/A_1(0)$, $r_2 = A_2(0)/A_1(0)$ and $r_3 = A_3(0)/A_1(0)$.

1.4 Inclusive Decay $D^0 \to \overline{K}^0\pi^-\mu^+\nu$ and the S-wave Component

In this thesis we investigate the inclusive decay $D^0 \to \overline{K}^0\pi^-\mu^+\nu$. There are no previous measurements of this decay, but the considerable data from the experimental study of $D^+ \to K^-\pi^+\mu^+\nu$ provide excellent insight about the D^0 decay [20, 21, 22, 23, 24, 25, 26]. According to isospin symmetry the D^+ and D^0 particles are different isospin[5] states of the same particle (like the proton and the neutron), so the semileptonic

[5] The isospin state I_z of a particle is related to its charge Q baryon number B and strangeness S by: $Q = I_z + \frac{1}{2}(B + S)$.

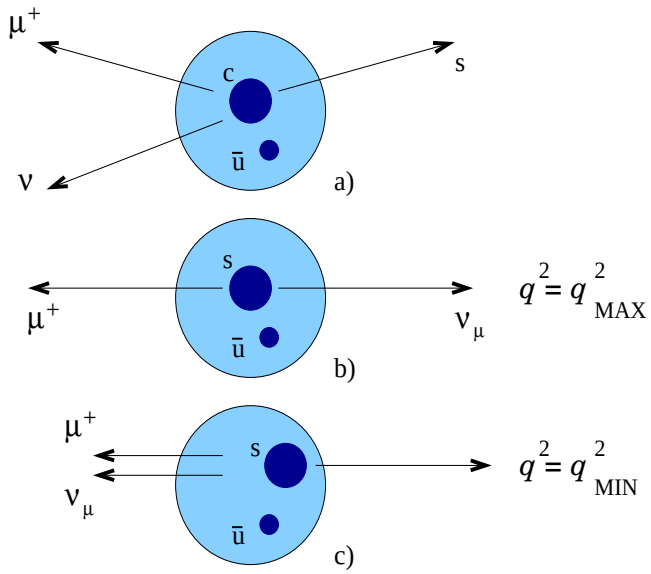

Figure 1.6: Different q^2 configurations for the semileptonic decay: a): generic configuration, b): q^2 maximum, the momentum transferred to the W and the kaon are minimum and the hadronization probability is higher. c): q^2 minimum, the momentum transferred to the W and the kaon are maximum and the hadronization probability is lower.

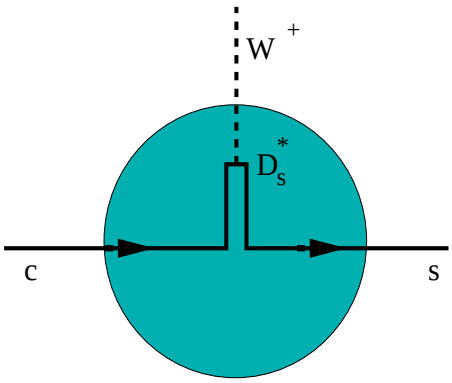

Figure 1.7: Schematic for the argument underlying the choice of the pole masses choice. The decay probability is higher when the q^2 transferred corresponds to the mass of a cs resonance with the same quantum numbers as the W.

decay amplitudes should be the same up to electromagnetic corrections. A recent study of $D^+ \to K^-\pi^+\mu^+\nu$ from the FOCUS experiment has shown that a description in which the $K^-\pi^+$ system is entirely composed of the $K^*(892)^0$ spin 1 resonance [27] agrees poorly with data. A model that includes a small $K^-\pi^+$ component with spin 0 has been proven to be a much better description of the data. The S-wave component is represented by fixed amplitude and phase ($Ae^{i\delta}$) that interferes with the K^*. To account for this component the decay amplitude in Eq. 1.7 must be modified as:

$$\frac{d^5\Gamma}{dm_{K\pi}dq^2d\cos\theta_V d\cos\theta_\ell d\chi} \sim |\underline{k}|(q^2-m_\ell^2)\{\left|\begin{array}{c}(1+\cos\theta_\ell)\sin\theta_V e^{i\chi}B_{K^{*-}}H_+ \\ -(1-\cos\theta_\ell)\sin\theta_V e^{-i\chi}B_{K^{*-}}H_- \\ -2\sin\theta_\ell(\cos\theta_V B_{K^{*-}}+Ae^{i\delta})H_0\end{array}\right|^2 \tag{1.15}$$

$$+\frac{m_\ell^2}{q^2}\left|\begin{array}{c}\sin\theta_\ell\sin\theta_V B_{K^{*-}}(e^{i\chi}H_+ + e^{-i\chi}H_-) \\ +2\cos\theta_\ell(\cos\theta_V B_{K^{*-}}+Ae^{i\delta})H_0 \\ +2(\cos\theta_V B_{K^{*-}}+Ae^{i\delta})H_t\end{array}\right|^2\}$$

1.5 Studies Presented in this Thesis

In this thesis the analysis of the decay $D^0 \to \overline{K}^0\pi^-\mu^+\nu$ using FOCUS data is presented. Using a model that describes the $\overline{K}^0\pi^-$ state as a dominant $K^*(892)^-$ state interfering with a small S-wave component, we measure the form factor ratios r_v and r_2 (our sensitivity is inadequate for the measurement of r_3). The investigation of the S-wave component is also presented, along with measurements of its amplitude. Finally, the inclusive branching ratio measurement $\Gamma(D^0 \to K^*(892)^-\mu^+\nu)/\Gamma(D^0 \to \overline{K}^0\pi^-\pi^+)$ is shown. All the measurements presented in this thesis have never been performed for the D^0 meson. The wealth of data from D^+ analyses from FOCUS and previous experiments provides guidance on the expected values for the different measurements. Fig. 1.8 shows previous measurements of the form factor ratios for

the decay $D^+ \to K^-\pi^+\mu^+\nu$, along with estimates from theory (which are calculated without distinction between the D^0 and the D^+). None of the previous measurements have accounted for S-wave, except for FOCUS. Moreover, for the FOCUS measurement backgrounds at low q^2 were rejected.

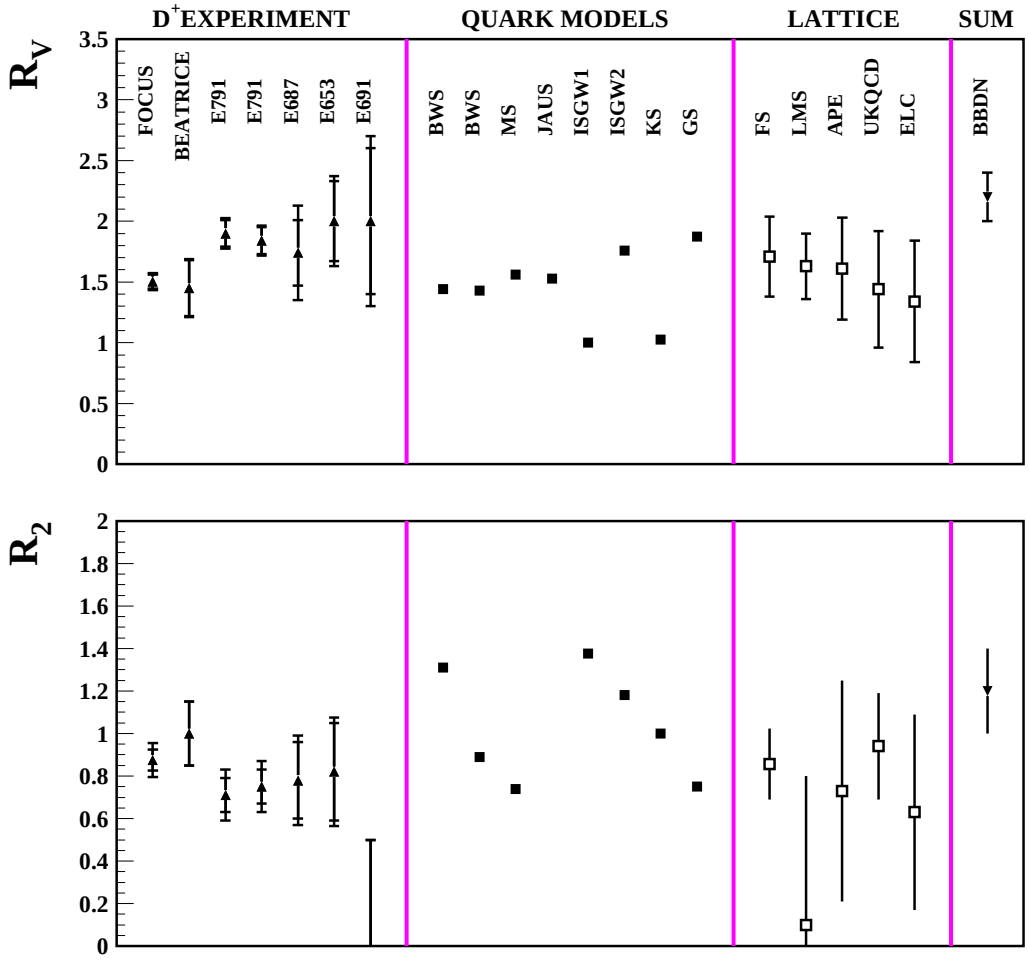

Figure 1.8: Expected values of r_v and r_2 are shown. We plot the measurements [20, 21, 22, 23, 24, 25, 26] for the decay $D^+ \to K^-\pi^+\mu^+\nu$ and the results from different theoretical approaches (quark models [7, 8, 9, 10, 11, 12, 13], lattice QCD [14, 15, 16, 17, 18], and sum rules [19]) which apply to both the D^0 and the D^+. The error bars on the experimental results are reported as the sum in quadrature of statistical and systematic uncertainty. The inner bars indicate the statistical component.

Chapter 2

The FOCUS Spectrometer

2.1 The FOCUS Experiment

FOCUS–E831 (Pho(FO)toproduction of Charm with an Upgraded Spectrometer) is a general purpose fixed target experiment that collected data during the 1996–1997 run at Fermilab. The experiment is an upgrade of the previous experiment E687 [28]. Major improvements led to an increase of about a factor of 10 in charm particles reconstructed (about 10^6 events are fully reconstructed in the "golden modes" $D^0 \to K^-\pi^+\pi^-\pi^+$, $D^0 \to K^-\pi^+$, and $D^+ \to K^-\pi^+\pi^+$) and better vertex resolution. Using an improved target where silicon track detectors interleave the active material, an excellent resolution in lifetime is achieved (about 30 fs for most modes). Charm particles are produced via photo–gluon fusion, which occurs through the collision of a photon beam on a BeO target. In the past four years FOCUS has produced analyses on different charm topics: CP violation, D^0–$\overline{D}^0$ mixing, rare and forbidden decays, precision measurements of semileptonic decays, baryon and meson lifetimes, fully hadronic baryon and meson branching ratios, charm spectroscopy, Dalitz analyses of resonant structures, charm anti–charm production, QCD studies involving double charm particles, and pentaquarks. Fig 2.1 shows a schematic of the FOCUS spectrometer, which will be described in detail in the rest of the chapter. Briefly, two magnets of opposite polarity deflect charged tracks. From the bend angle, which is measured in five stations of multi–wire proportional chambers, the track momentum is determined. A gap in the spectrometer around the

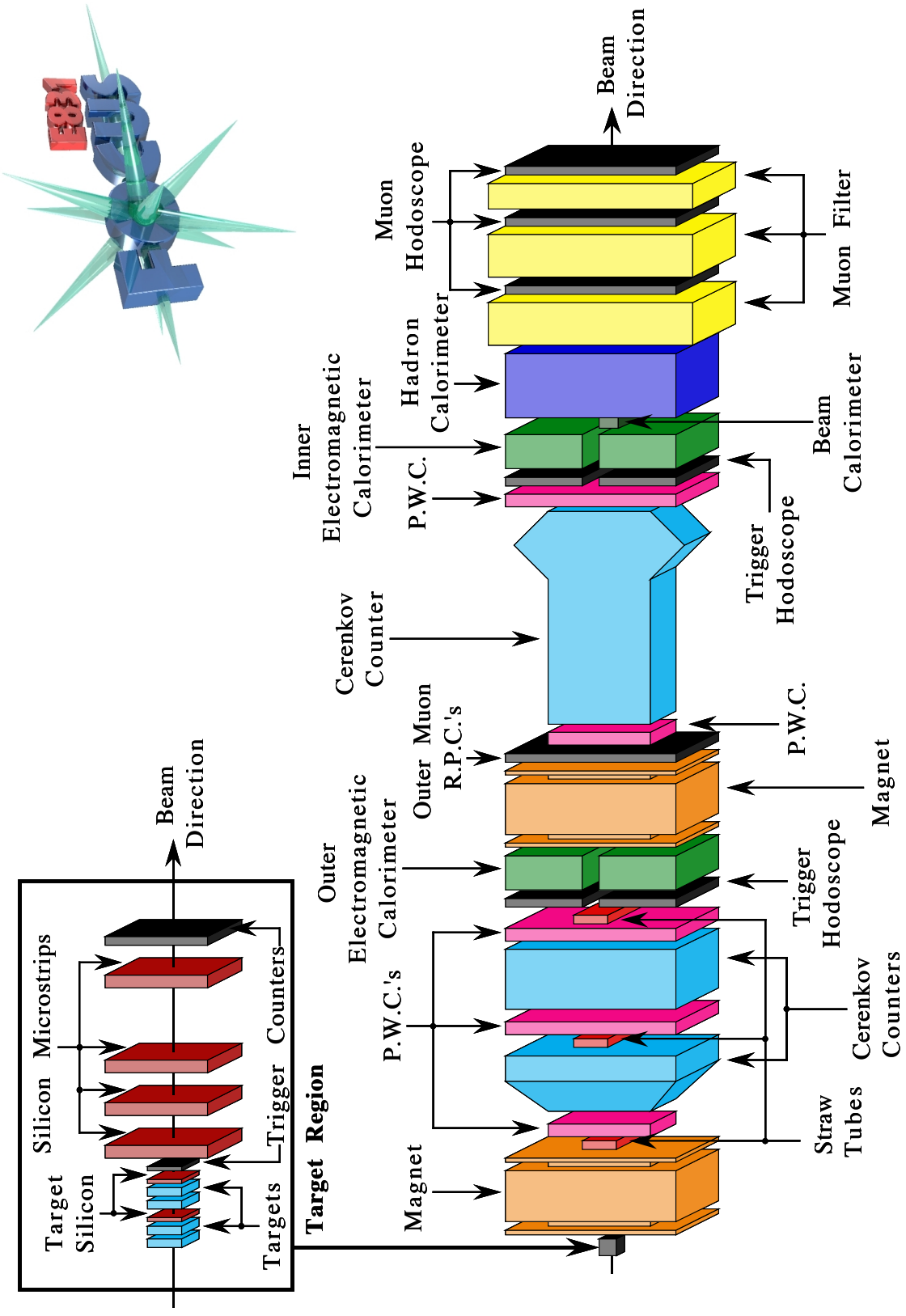

Figure 2.1: The FOCUS Spectrometer.

beam direction allows for the e^+e^- pair to travel through without interactions in the material. The magnetic fields focus the pairs onto a calorimeter which measures their energy and the energy of beam photons that do not interact in the experimental target. Track direction upstream of the magnets is reconstructed using four Silicon Microstrip detectors. Charged particle identification for electrons, pions, kaons, and protons is performed using three multi–cell threshold Čerenkov counters. Neutral pion identification as well as electron and positron identification is determined from the energy deposited in two electromagnetic calorimeters. A hadron calorimeter measures the energy deposited from pions, kaons, protons, and neutrons. Muons are identified by the hits left in tracking systems after several meters of material which absorbs the other particles. An "inner" muon system detects high momentum particles that travel through the whole spectrometer. The active material consists of scintillators with the shielding material containing about 3 m of steel. Muons with low momentum and large aperture angles are identified by the "outer" muon system. This outer muon system consists of RPC chambers, and the first magnet provides the shielding material.

2.2 The Beam Line

2.2.1 The Tevatron Proton Beam

The high energy photon beam of the FOCUS experiment is produced from the 800 GeV/c proton beam extracted from the Tevatron synchrotron accelerator. The proton acceleration is performed in five steps. Hydrogen ions H^- are first accelerated to 750 KeV by the electrostatic accelerator Cockcroft-Walton and inserted in the LINear ACcelerator. The LINAC accelerates the ions to 400 MeV and strips the electrons by sending the beam through a thin carbon foil. The final three steps in the proton acceleration process are performed by three synchrotron accelerators: the Booster (which accelerates protons to 8 GeV/c), the Main Ring (150 GeV/c) and the Tevatron

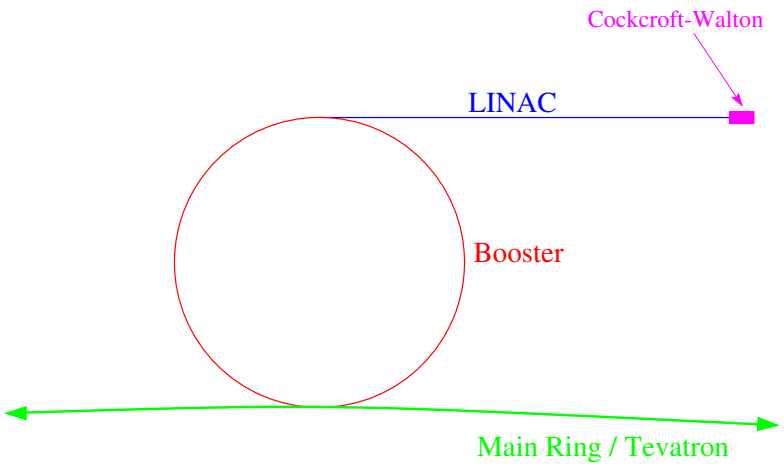

Figure 2.2: The five accelerators that produce 800 GeV/c protons from hydrogen ions H^- are shown. The Main Ring and the Tevatron use the same tunnel. The LINAC linear accelerator is 130 m long, the Booster ring is about 480 m long, and the Tevatron ring is about 6.4 km long.

(800 GeV/c). The five accelerators are shown in Fig. 2.2. The protons (which are grouped into "batches" by the booster), are accelerated in the Tevatron for 40 seconds and, during the fixed target runs, slowly spilled over 20 seconds to the fixed target experiments. The Tevatron works at a radio frequency of 53 MHz, so every 18 ns a new proton batch reaches the interaction area. The proton beam directed to the tunnel can be switched towards different areas, the proton, meson and neutrino area. The FOCUS experiment uses the Wide–Band Photon Beam of the proton area.

2.2.2 The Production of the Photon Beam

The photon beam is produced with a strategy that aims at removing contamination from other neutral particles (e.g. π^0, n, Λ^0, and K^0), and at preserving high energy. The procedure consists of three steps:

(1) Conversion of the proton beam into a neutral beam

(2) Conversion of the neutral beam into an e^+e^- beam

(3) Photon beam production through bremsstrahlung of e^+ and e^-

Three different targets are used for these steps, and the energy and the intensity of the beam are depleted at each step. The distance between the first target for the photon beam production and the experimental target is 350 m. Fig. 2.3 shows the beamline.

The 800 GeV/c protons from the Tevatron collide with a liquid deuterium target ("primary target") which is about 1.6 m long. From hadronic interactions different neutral particles are produced, among them neutral pions that decay into $\gamma\gamma$ pairs. The large A/Z^2 ratio ($\sim$ higher radiation length over interaction length) of the deuterium provides a high cross section for strong interactions while reducing the photon reinteractions.

After emerging from the primary target, charged particles are deflected from the zero–degree beamline. The neutral beam is sent through a half radiation length lead converter. The photons convert to electron–positron pairs, while the other particles have reduced interactions. The target is chosen to be short enough so that, while allowing the photon conversion, the reduction of the electrons average energy though bremsstrahlung is low. Magnet dipoles deflect the e^+ and e^- around a hadronic "dump" that absorbs the neutral beam.

The energy of the charged beam is selected through collimators and magnets. The nominal momentum of the beam is 300 GeV/c. In order to reduce the loss in beam intensity due to the multi–step process, $e^{\pm}$ with a wide momentum spectrum are captured in the beam. The energy distribution has a spread of about 15% around the nominal energy, therefore this beamline is called "Wide Band". After being refocused on the beamline, the $e^{\pm}$ energy is measured in a spectrometer which consists of analysis magnets and a silicon tracking system. Finally, the $e^{\pm}$ beam impacts on a lead radiator where photons are produced through bremsstrahlung. The radiator is approximately 20% of a radiation length long, in order to reduce secondary production of photons, which would make it more difficult to evaluate the photon beam energy.

After the radiator, dipole magnets deflect the electrons and positrons away from the beamline, towards two calorimeters (RESH and POSH) for their energy measurement. The photon beam, which has an average momentum of 180 GeV/c, interacts in the experimental target. A synchrotron radiation background is produced by the electrons in the sweepers. This background is reduced by a lead wall and a lead collimator between the electron dump and the experimental target. The electrons produced in the lead wall are eliminated by other magnets.

The three step process, although causing a decrease of the beam energy and intensity, has many advantages. The main advantage is the production of a beam which has a small amount of hadron contamination. Simulation and calibration studies reveal that a possible background comes from $\Lambda^{0\prime}$ s that decay into the $p\pi^-$ final state. These charged particles are within the acceptance of the $e^{\pm}$ beam line and arrive at the radiator, where they produce neutral hadrons that contaminate the photon beam. According to the studies performed, the contamination in the photon beam of such events is less than one event every 10^5, and the trigger accepts only 1% of events produced by these neutral hadrons colliding on the target. The photon beam production method also allows a good determination of the photon energy (as will be described in the next section). Finally, the beam elements can be varied in order to perform calibration studies. For instance, by removing the radiator and turning off the sweeping dipoles, an $e^{\pm}$ beam is produced.

2.2.3 Determination of the Photon Beam Energy

The energy of the photon colliding on the target of the experiment is given by:

$$E(\gamma) = E(e_i) - E(e_r) - \sum E(\gamma_{sec}) \tag{2.1}$$

where e_i and e_r are the incoming and recoil electron (positron) before and after the radiator, respectively, and the sum is over the photons (γ_{sec}) which are produced from

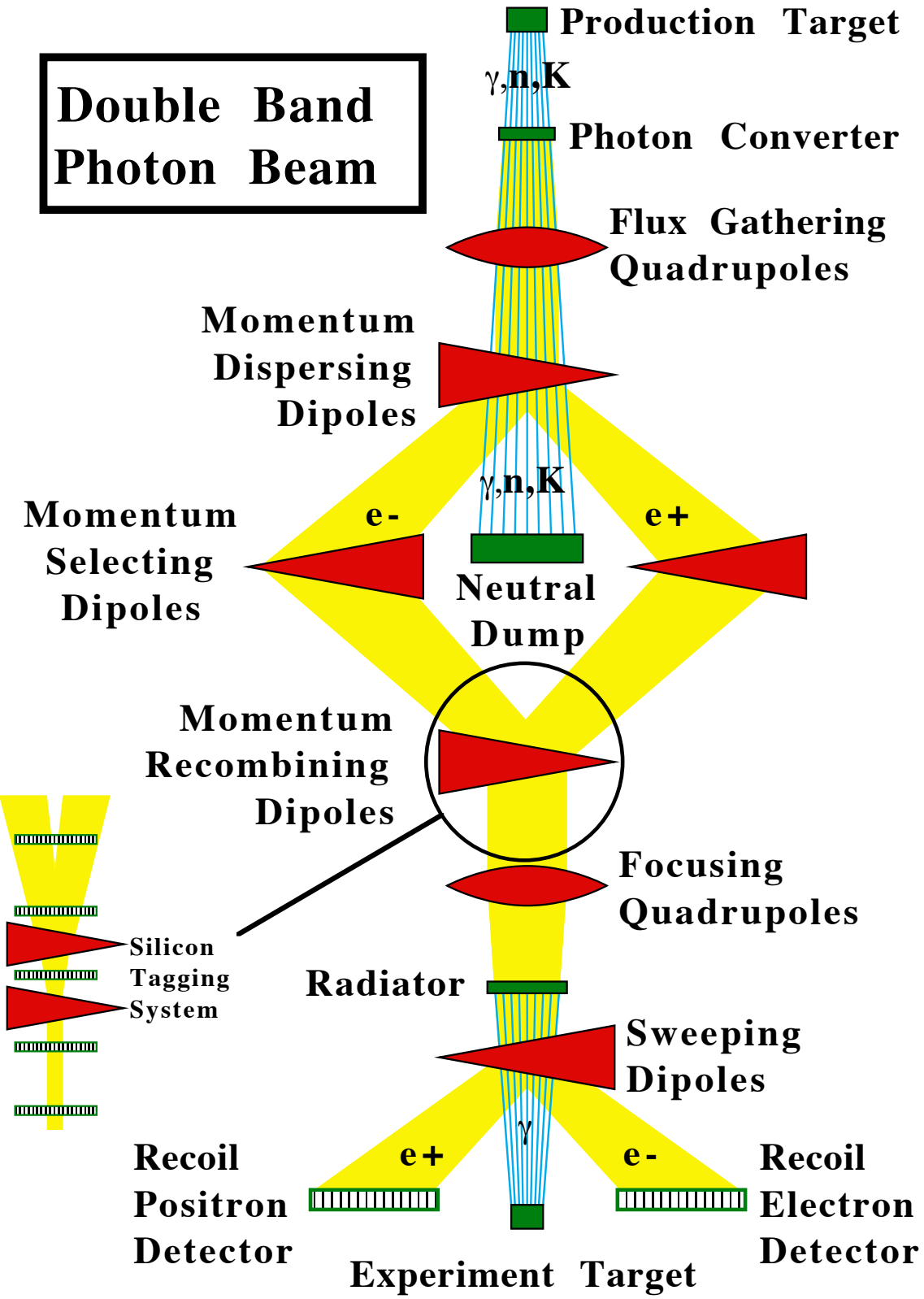

Figure 2.3: Beamline for the photon beam production.

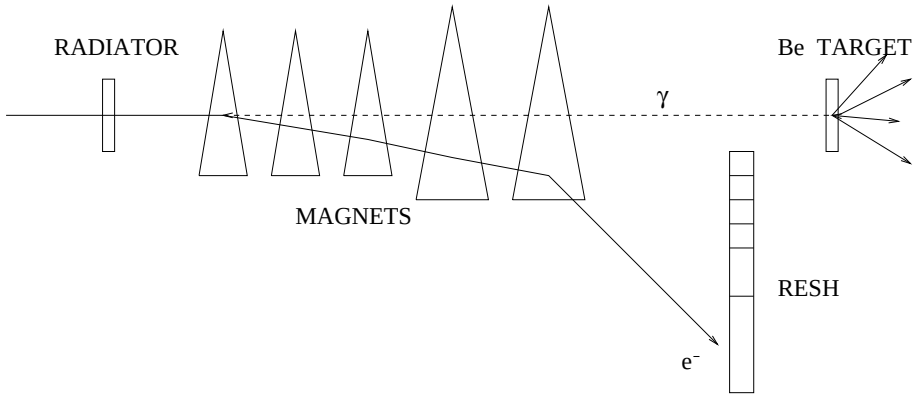

Figure 2.4: Schematic of the Recoil Electron Shower Hodoscope

multiple bremsstrahlung and that either do not interact in the target, or interact electromagnetically. Three different systems measure these three energies.

The energy of the incoming electron is measured by the deflection in the magnetic field of two dipole magnets. Five microstrip planes measure the tracks direction in the horizontal plane (bend plane). Two planes are positioned before the magnets, one in between (to resolve ambiguities in multi–tracks events), and the other two after the magnets. Each plane consists of 256 strips each with a 300 μm pitch and the active area is 7.7 cm wide and 5.7 cm high. The geometric acceptance of the system is about 81%, and it delivers a precision of 2% on the momentum measurement. The spectrometer area is shown in the inset in Fig. 2.3.

The energy of the recoil $e^{\pm}$ emerging from the radiator is measured from the bend angle in the magnetic field, but in this case the deflection is determined using electromagnetic calorimeters: a Recoil Electron Shower Hodoscope (RESH) for electrons, and a recoil POsitron Shower Hodoscope (POSH) for positrons. A schematic of the RESH detector is shown in Fig. 2.4. Dipole magnets placed along the beamline deflect the electrons (positrons) towards the RESH (POSH). Both RESH and POSH are composed of 13 sampling calorimeters, where the passive material is lead and the detectors are scintillators. The length of the calorimeters is 24 radiations lengths. The impact point of

the electron (positron), which determines the bend angle and therefore the momentum, is given by the nominal position of the hit calorimeter, or the average of the positions if more than one is hit. The energy of the track measured by the calorimeter must agree with the momentum measurement from the bend angle. The acceptance of the system lies within the range $\sim 0.35 < E_\gamma/E_e < 0.9$, which corresponds to photon momenta between 122 GeV/c and 315 GeV/c.

The energy of non–interacting photons is measured by the Beam Gamma Monitor (BGM). The BGM is a small acceptance calorimeter (23 cm $\times$ 23 cm) located downstream of the FOCUS spectrometer. The BGM measures the electromagnetic energy in a small cone around the beam line. The detector is a 24 radiation lengths long sampling calorimeter with 24 layers of alternating lead and scintillator. The photons that do not interact in the target travel through the entire FOCUS detector and reach the BGM. About 20% of the time the photons interact electromagnetically in the target and produce e^+e^- pairs. These pairs are focused on the BGM by the analysis magnets of the experiment. The e^+e^- energy is also measured in the BGM.

2.3 The Target Region

The photon beam is directed on the target of the experiment. There are three different target configurations used in FOCUS. About 2/3 of the data has been collected with the most upgraded configuration.

The initial target configurations consisted of Berillyum. This material was chosen for the low atomic number Z reduces the background from e^+e^- production (the cross section for this event is proportional to Z^2), relative to charm photoproduction. During the course of the E687 experiment, it was discovered that an excellent background rejection is achieved by requiring that the decay of the charmed particle to occur outside of the target material. This requirement reduces contamination from events where a hadronic reinteraction in the material is misidentified as a charm decay. In order

to increase the percentage number of decays "in air", the target was longitudinally segmented. With this configuration most of the background comes from other charm decays, that are better understood and easier to simulate than hadronic reinteractions.

The second target configuration consisted of four layers of BeO. The greater density of BeO permits the use of thinner segments and increases the number of decays outside the material. Each target segment was 6.75 mm thick and had an area of $(25.4 \text{ mm})^2$ in the plane transverse to the beam direction.

The final target configuration transforms the target region into an active track reconstruction system by introducing silicon strip planes between the target segments. The Target Silicon system (TSSD) is composed of two stations, one (TSSD1) between the second and the third slabs, and the other (TSSD2) downstream of the last slab. Each station contains two planes with different views ($\pm 45^0$ from the horizontal). Each plane is 300 μm thick and has 1024 instrumented strips each with a pitch of 25 μm. Each strip measures 50 μm $\times$ 25 μm. The target region is shown in Fig. 2.5. In Fig. 2.6 the distribution of reconstructed primary and secondary vertices for background subtracted D decays are shown. From the distribution of the secondary vertex one observes how the target configuration allows for most of the decays to occur in air. The target silicon detector is described in more detail in Reference [29].

2.4 Tracking Systems Downstream the Target

The track reconstruction of charged particles downstream of the target is performed by three systems: Silicon Strip Detectors (SSD), Multi–Wire Proportional Chambers (MWPC), and Straw Tubes.

2.4.1 Silicon Strip Detectors

High resolution tracking in the region between the target and the first magnet is performed by the Silicon Strip Detector (SSD). The charged particles that cross the

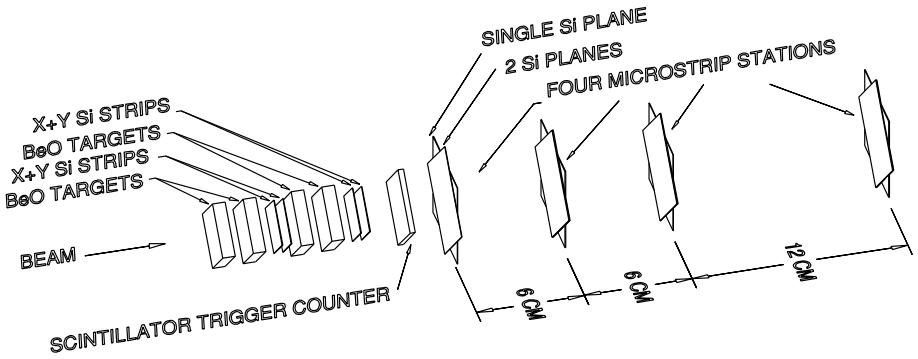

Figure 2.5: The Target region and the upstream systems of tracking detectors (TSSD and SSD) are shown.

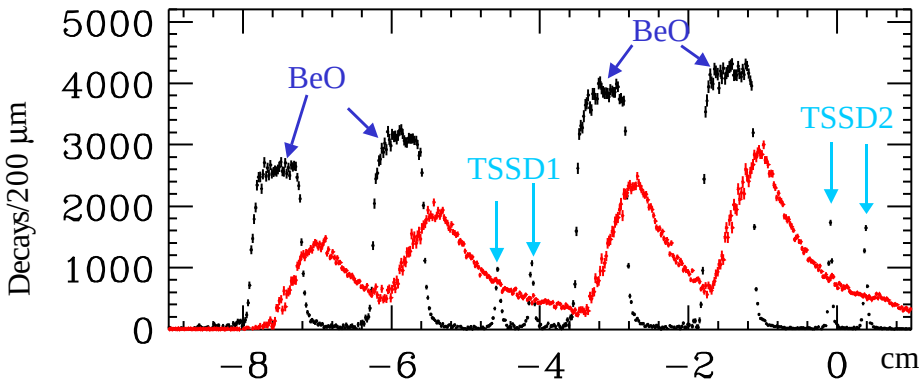

Figure 2.6: Distribution of the z coordinate of the primary and secondary vertices for background subtracted charm events. The primary vertex distribution (black points) shows the location of the target segments and the TSSD stations (note how a small fraction of the events is produced in the active tracking system). The secondary vertex distribution (red points) shows how most of the events occur outside the material.

Table 2.1: The specifications of the SSD planes (listed from the most upstream to the most downstream).

Station	Active Area		Strip Pitch
	Total	High Res.	
1	2.5×3.5 cm^2	1.0×3.5 cm^2	25 μm , 50 μm
2	5.0×5.0 cm^2	2.0×5.0 cm^2	50 μm , 100 μm
3	5.0×5.0 cm^2	2.0×5.0 cm^2	50 μm , 100 μm
4	5.0×5.0 cm^2	2.0×5.0 cm^2	50 μm , 100 μm

silicon strip ionize the material. Their direction is reconstructed from the collection of the released charge by the readout strips, the establishment of a hit, and the subsequent track reconstruction algorithm.

As shown in Fig. 2.5, the SSD system consists of twelve planes divided into four stations of three planes each. The first three stations are 6 cm apart, while the last station is 12 cm downstream of the third station. The three planes in each station are oriented along three different directions: -135°, -45° and -90° with respect to the horizontal axis (x). To increase the resolution in the region of small aperture angles, where the track density is higher, each plane has a finer pitch in the inner region than in the outer one. For the first station where due to the shorter lever arm the tracks are closer to each other, the two regions have 25 μm and 50 μm pitch, respectively. For the other planes the pitch values are 50 μm and 100 μm. Each plane has 688 ADC readout channels. The spatial resolution of the different planes ranges from 14 μm to 7 μm. Table 2.1 shows the specifications of each station.

2.4.2 Multi–Wire Proportional Chambers

Tracking downstream of the first magnet is performed by Multi–Wire Proportional Chambers (MWPC). The information from the MWPC is also used to determine each charged particles momentum from the bend angle in the magnetic field of the two analysis magnets of opposite polarity. In a gaseous environment, planes of high voltage wires and sense wires at ground are alternated. Charged tracks that travel through the

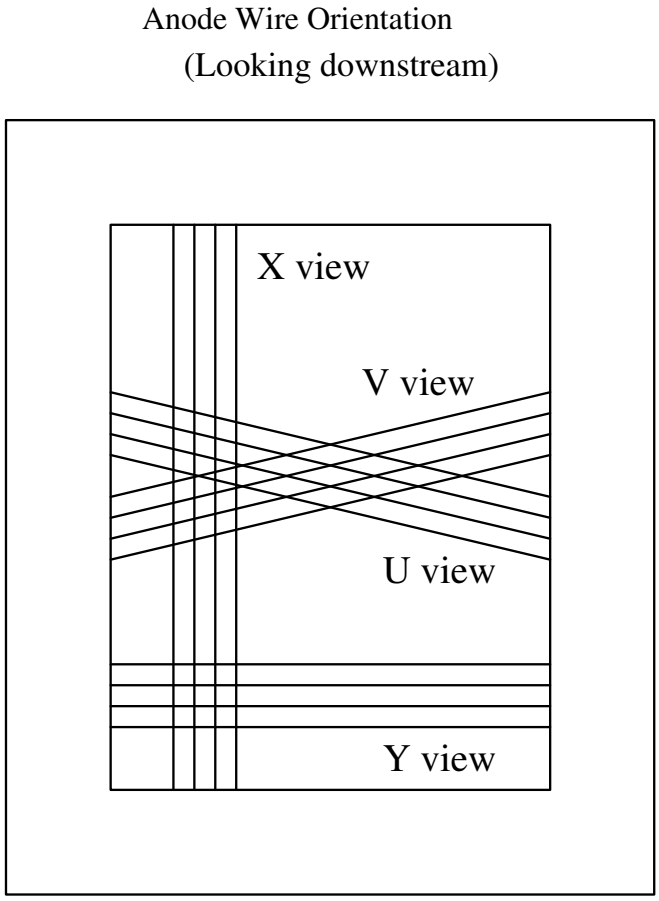

Figure 2.7: The four views of each MWPC station are shown.

Table 2.2: The specifications of the five Multi–Wire Proportional Chambers.

Wire Chamber	Wire spacing	Wires/plane				Size	Position
		X	Y	U	V	$(X \times Y)$	(cm from target)
P0	0.080"	376	640	640	640	76×127 cm^2	403
P1	0.130"	480	704	768	768	152×229 cm^2	644
P2	0.130"	480	704	768	768	152×229 cm^2	879
P3	0.080"	376	640	640	640	76×127 cm^2	1,444
P4	0.130"	480	704	768	768	152×229 cm^2	2,286

system ionize the gas. The freed electrons that are accelerated towards the sense wire ionize the gas too, producing a cascade charge that is collected on the wire. The gas is a mixture of argon (65%) and ethane (35%), bubbled through 0° C ethyl alcohol. The system consists of twenty planes divided into five stations of four planes corresponding to four views: X along the vertical axis (which measures the direction in the horizontal plane), an orthogonal Y view, and two views at $\pm\ 11.3^0$ from the Y view (U and V). The different views are shown in Fig. 2.7. In order to achieve good momentum resolution, there is more information provided in the bend (vertical) view. The first three stations (P0, P1 and P2) are placed between the magnets while the last two (P3 and P4) are placed downstream of the second magnet. Momentum determination is performed using the information from the SSD system when the track is reconstructed in both systems. The apertures of the magnets limit the maximum angles of the emerging track, so P0 and P3 are smaller than the other stations. Table 2.2 shows the specifications of the MWPC.

2.4.3 Straw Tubes

Additional information, which has yet to be used to its full potential, is provided by straw tube wire chambers. The initial design for the tracking detectors was based on a plan to deaden the wire chambers in the high intensity pair region. In order to reconstruct tracks in this region Straw Tubes Chambers were built, as they can operate in higher rate environments than the MWPC. It turned out that deadening the MWPC

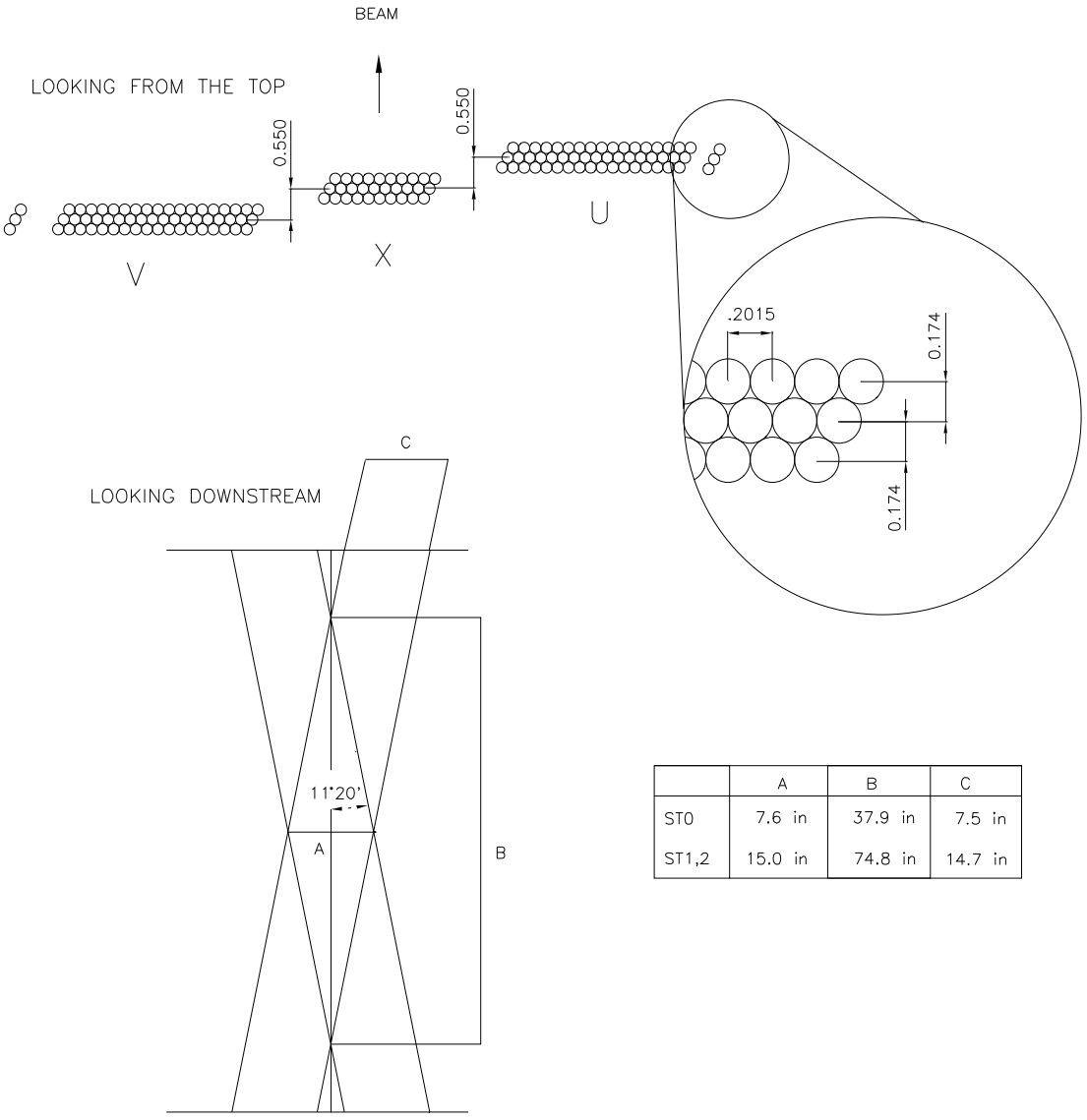

	A	B	C
ST0	7.6 in	37.9 in	7.5 in
ST1,2	15.0 in	74.8 in	14.7 in

Figure 2.8: The layout of the Straw Tubes is shown.

Straw Chamber	Straw length	Wires/view		Total Wires
		Vertical	Angled	
ST0	138 cm	3×10	3×38	258
ST1	241 cm	3×10	3×74	474
ST2	241 cm	3×10	3×74	474

Table 2.3: Specifications of the three straw tube chambers.

was not necessary. The straw tubes worked fine, but they were not implemented in tracking.

There are three stations of Straw Tubes adjacent to P0, P1 and P2. The Straw Tubes work with the same gas–ionizing technique as the MWPC, but the high voltage cathode consists of a metal coated tube around the ground sense wire. Each station has three views: one along y (to measure the horizontal direction), and the other two at $\pm\ 11.3^0$ from the vertical. There are three layers of tubes for each view. The Straw Tube layout within a chamber is presented in Fig. 2.8 and the details for the three chambers are shown in Table 2.3.

2.5 Analysis Magnets

Two large aperture analysis magnets (M1 and M2) are used to deflect charge particles along the y direction for the momentum measurement. The magnet M1 is placed at the beginning of the spectrometer, between the last SSD station and P0. The magnet M2 lies between P2 and P3. The magnets are 1.7 m long and have apertures which measure 76 cm (along x) $\times$ 127 cm (along y). The magnets M1 and M2 work with currents of 1020 A and 2000 A, respectively. Each magnet is characterized by the transverse momentum "kick", which for a given track relates the bend angle $\Delta\theta$ to the momentum P by:

$$\Delta\theta = \frac{P_T \text{ kick}}{P}$$

The P_T kick of M1 and M2 are +0.400 GeV/c and -0.835 GeV/c, respectively. The values are chosen in order to focus the e^+e^- pairs on the BGM.

Detector	Gas	Threshold (GeV/c)		
		π	K	p
C1	58% He/42% N_2	8.5	29.9	56.8
C2	N_2O	4.5	16.2	30.9
C3	He	17.0	61.0	116.2

Table 2.4: Characteristics of the Čerenkov detectors

2.6 Čerenkov Counters

The Čerenkov counters [30] are the main device for charged particle identification in FOCUS. They identify electrons, pions, kaons, protons, and in a small momentum range can be useful in distinguishing pions from muons. The identification method is based on the Čerenkov radiation that is or is not emitted by a particle traveling through the detector. A charged particle emits Čerenkov light in a medium with index of refraction n if its velocity β is greater than the velocity of light in that medium, namely if (in $c = 1$):

$$\beta = \frac{P}{E} = \frac{P}{\sqrt{P^2 + m^2}} > \frac{1}{n}$$

The momentum threshold depends on the mass of the particle:

$$P_{th} = \frac{m}{\sqrt{n^2 - 1}}$$

and the light is emitted at an angle with respect to the flight direction given by:

$$cos\theta = \frac{1}{n\beta}$$

as schematically shown in Fig. 2.9

There are three multicell Čerenkov counters called C1, C2, and C3, that work in threshold mode. The gases used in the three detectors are different, and provide a large momentum range where pions are well separated from kaons and protons, and a fairly wide range for the kaon–proton separation. The momentum threshold for electrons is

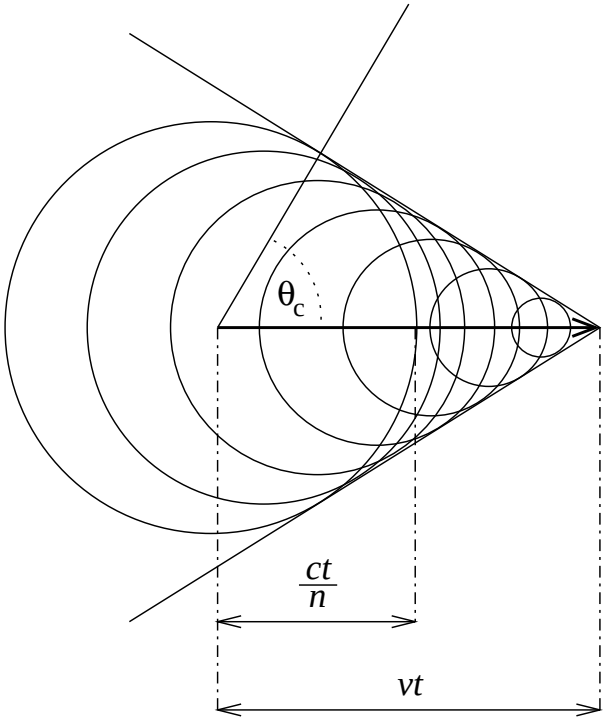

Figure 2.9: A schematic for the Čerenkov radiation angle of emission is shown.

Definite Čerenkov ID range (GeV/c)				
	e	π	K	p
3-chamber	0.16–8.5	4.5–8.5	16.2–29.9	16.2–56.8
5-chamber	0.16–17.0	4.5–17.0	16.2–56.8	16.2–56.8 and 61.0–116.2
Ambiguous Čerenkov ID range (GeV/c)				
	e/π	$e/\pi/K$	K/p	π/K/p
3-chamber	8.5–29.9	29.9–56.8	4.5–16.2	0.16–4.5
5-chamber	17.0–61.0	61.0–116.2	4.5–16.2	0.16–4.5

Table 2.5: Particle positive and ambiguous identification ranges for tracks reconstructed in 3 and 5 MWPC.

very low, and electrons are always above threshold in C1, C2 and C3. The properties of C1, C2 and C3 are summarized in Table 2.4, while Table 2.5 shows the momentum ranges for the different particles identification.

The counter C1 is located between P0 and P1 and uses a Helium (58%) and Nitrogen (42%) mixture. The momentum thresholds for pions, kaons, and protons are 8.5 GeV/c, 29.9 GeV/c, and 56.8 GeV/c, respectively. The gas volume is optically divided by mirrors into 90 cells (see Fig. 2.10 a). The mirrors are used to reflect the Čerenkov radiation onto photomultiplier tubes placed outside the gas volume. Different mirrors are used for the inner and outer regions. For the cells in the outer region (cells 1 to 40) spherical mirrors focus the photons on each individual photomultiplier tube. The inner region (41–90) uses planar mirrors at $\pm 45^0$ from the beam direction, that reflect the light towards 50 photomultiplier tubes. These tubes are surrounded by Wilson cones, which serve to reflecting the light to the apex of the cone, where the tubes are located.

The counter C2 is located between P1 and P2 and uses Nitrous Oxide (N_2O). The thresholds for pions, kaons, and protons are 4.5 GeV/c, 16.2 GeV/c, and 30.9 GeV/c, respectively. For both inner and outer cells planar mirrors at $\pm 45^\circ$ with respect to the beam direction are used. The division in cells is shown in Fig. 2.10 b.

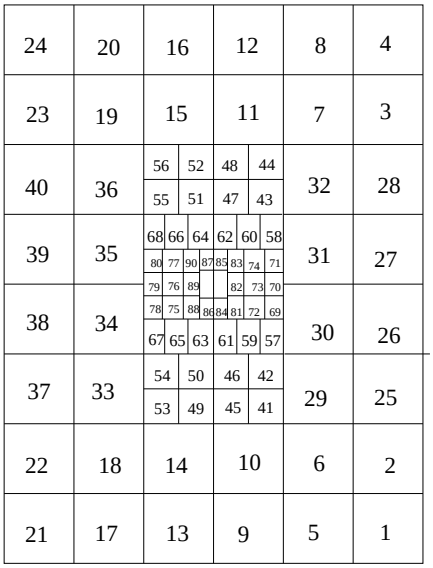

(a) C1. Inner cells (1–40) use spherical mirrors, outer cells (41–90) use planar mirrors.

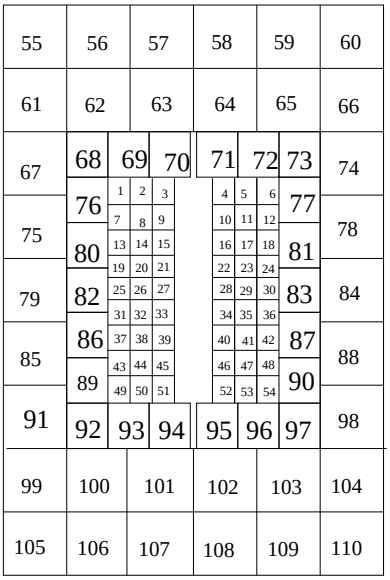

(b) C2. Inner cells (1–54) use planar mirrors, outer cells (55–110) use spherical mirrors.

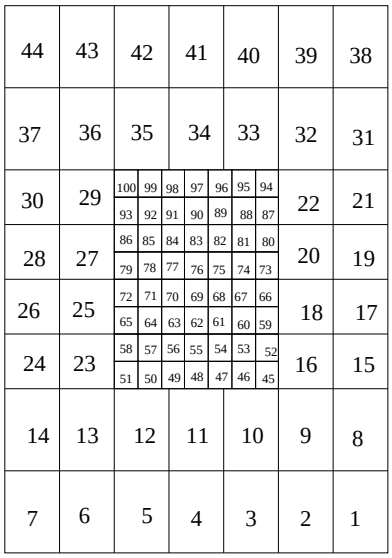

(c) C3. All cells use spherical mirrors.

Figure 2.10: Schematic of the cells for C1, C2, and C3.

The counter C3 lies between P3 and P4 and uses Helium. The momentum thresholds for pions, kaons and protons are 17.0 GeV/c, 61.0 GeV/c, and 116.2 GeV/c, respectively. The gas volume is divided into 100 cells by spherical mirrors that focus the Čerenkov radiation onto the photomultiplier tubes outside the gas volume (see Fig. 2.10 c). A central gap prevent e^+e^- pairs from interacting in the counter.

2.7 Calorimetry

Three calorimeters are used to measure the energy of different particles: the Outer Electromagnetic Calorimeter, the Inner Electromagnetic Calorimeter, and the Hadron Calorimeter. The measurement is performed using a destructive process. The particle that travels through the material produces other particles, and by detecting these particles the energy of the parent is measured. The Inner Electromagnetic Calorimeter and the Hadron Calorimeter are included in the trigger logic. For this analysis these detectors are used only for their trigger function.

2.7.1 Outer Electromagnetic Calorimeter

The Outer Electromagnetic Calorimeter [31] is situated between P2 and the second analysis magnet, M2, and it is used to measure the energy of electrons, positrons, and photons in the outer region. The energy measurement is performed by reconstructing the electromagnetic shower that originates from bremsstrahlung ($e^{\pm} \rightarrow e^{\pm}\gamma$) and pair conversion ($\gamma \rightarrow e^+e^-$).

The detector is 18.4 radiation lengths long and has an aperture that matches the aperture of M2 and a gap to allow conversion pairs to pass through without interacting. This geometry determines an angular acceptance of 28 mrad $\leq \theta_x \leq$ 142 mrad and 49 mrad $\leq \theta_y \leq$ 114 mrad. The calorimeter is built with a sampling structure (see Fig. 2.11), with 23 alternating layers of lead (where the interactions occur) and scintillators (that detect the charged particles).

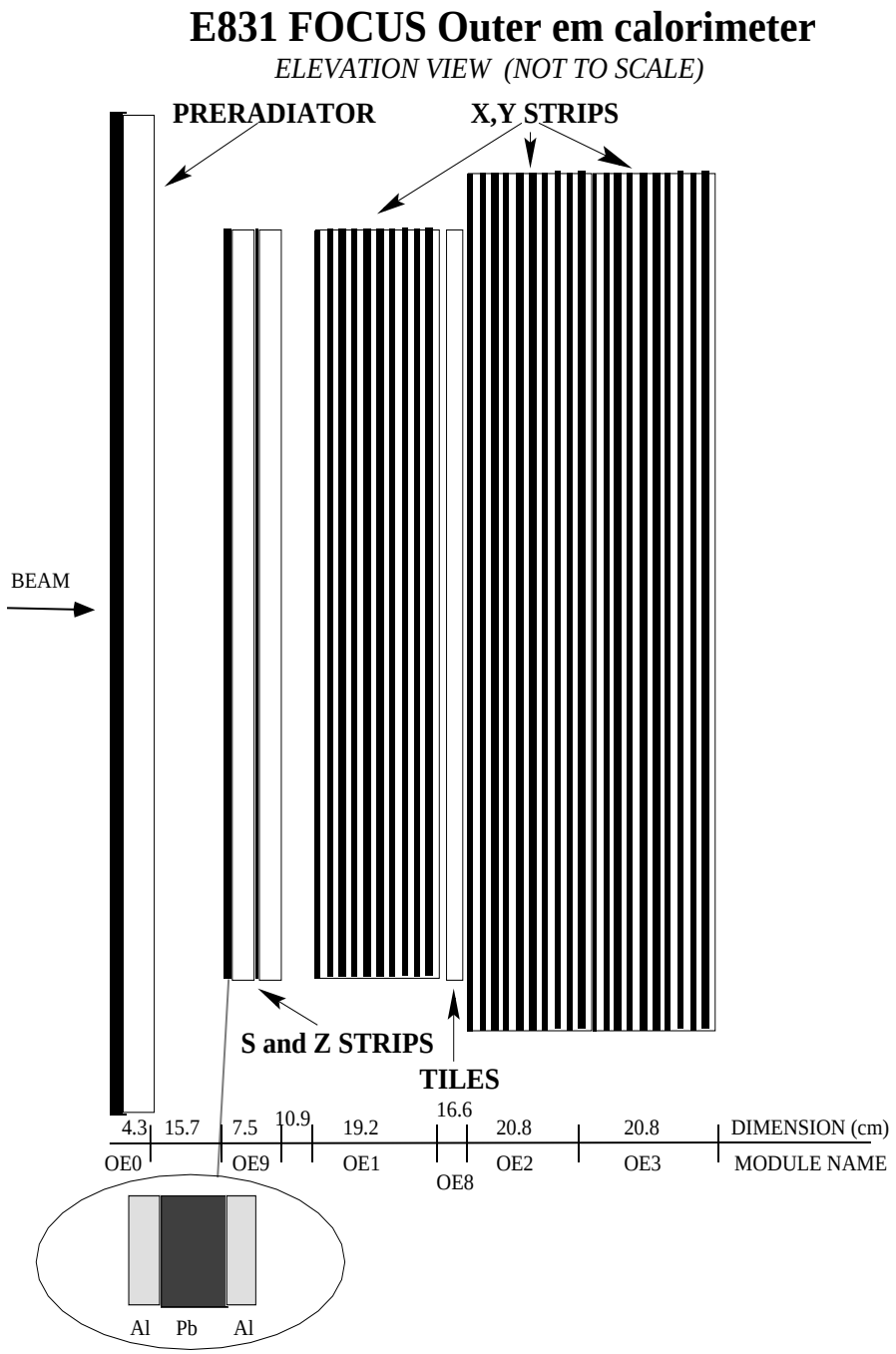

Figure 2.11: A side view of the Outer Electromagnetic Calorimeter.

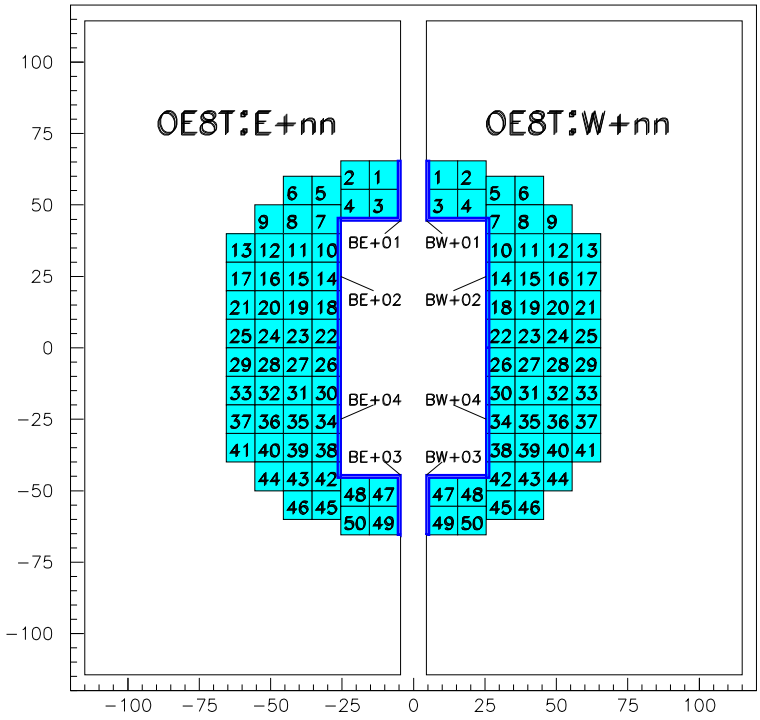

Figure 2.12: A frontal view of the tiles arrangement in the tie breaker plane.

The scintillator planes consist of rectangular tiles, and are divided in four views, x, y, s and z (the last two being at $\pm 45^0$ from the horizontal). The event where two photons leave four hits in the x and y oriented planes has a four fold ambiguity. The ambiguity is solved by using the s and z information, energy matching, and the information from an additional plane ("tie breaker" plane) of 100 scintillator tiles, the arrangement of these tiles is shown in Fig 2.12.

2.7.2 Inner Electromagnetic Calorimeter

The Inner Electromagnetic Calorimeter [32] is located immediately downstream of the last Multi–Wire Proportional Chamber. It measures the energy of electrons, positrons, and photons. The detector consists of 802 lead glass blocks arranged in a tower geometry, and is divided in two by a vertical gap of 14 cm that allows conversion pairs to pass through without interacting (see Fig. 2.13). The blocks are 60.2 cm long in the z direction (which corresponds to 18.75 radiation lengths and 2.2 interactions lengths), and measure 5.8 cm×5.8 cm in the plane transverse to the beam direction (10% of the blocks are slightly smaller). Each block is wrapped in aluminized mylar which reflects towards a photomultiplier tube the photons in the electromagnetic shower. The information on the energy deposited in groups of nine blocks is used in the trigger logic.

2.7.3 Hadron Calorimeter

Charged and neutral hadronic energy is measured by the Hadron Calorimeter [33, 34], where hadrons interact strongly producing mainly pions in the final state. Most hadrons (60%) start their hadronic shower in the lead glass. The Hadron Calorimeter is placed downstream of the Inner Electromagnetic Calorimeter and it consists of 28 alternate layers of 4.4 cm thick steel and 0.7 mm thick scintillator tiles. The calorimeter is 209 cm long (7.8 interaction lengths) and measures 200 cm×300 cm along x and y,

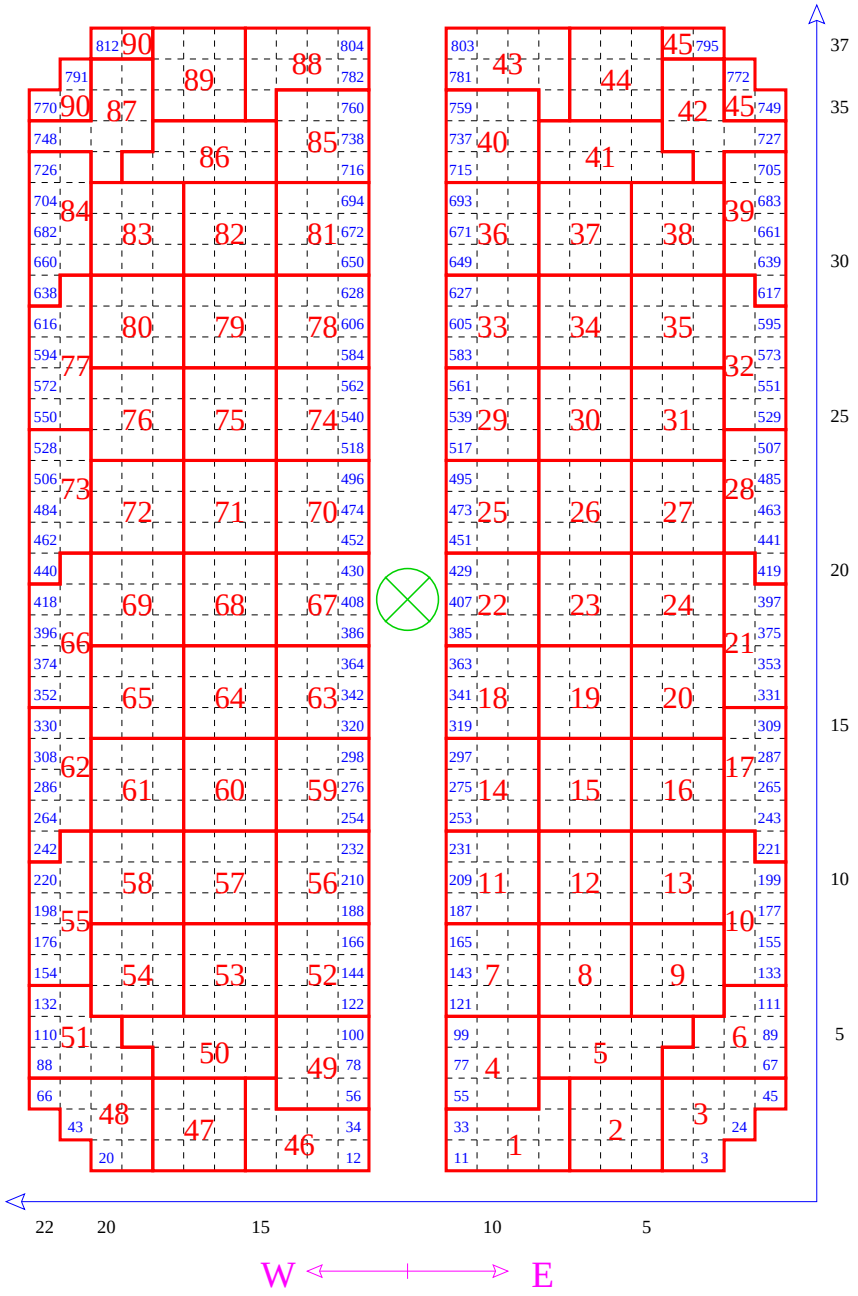

Figure 2.13: A schematic of the arrangement of blocks in the inner electromagnetic calorimeter. The blocks are represented by dashed lines, while heavy lines show the grouping used for the trigger.

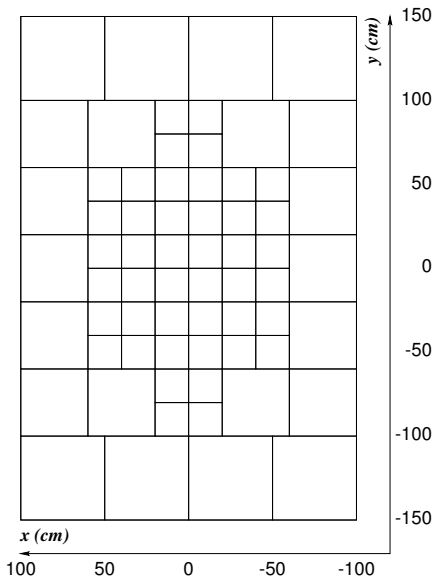

(a) Front view

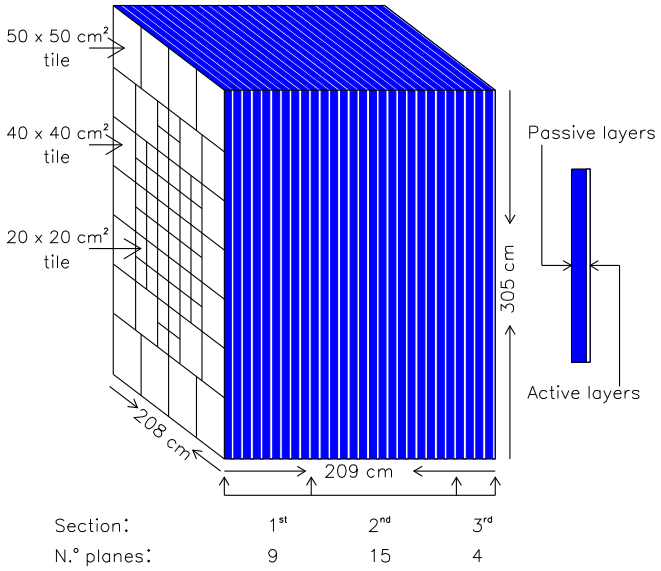

(b) Side view

Figure 2.14: Schematic of the Hadron Calorimeter for the front (a) and side (b) views.

respectively. Each scintillator plane is composed of 66 tiles, with smaller sized tiles in the inner region and larger sized tiles in the outer region (see Fig 2.14). Multiple layers are optically combined to form a tower geometry: the first nine layers form the first tower, the next fifteen layers form the second tower and the last four layers form the third tower. This structure allows for a small number of readout channels (192) while still measuring the energy as a function of depth. The scintillators have a fast response and the information provided by the hadron calorimeter is included in the first level trigger.

2.8 Muon Identification Detectors

The Outer and the Inner Muon detectors are used to identify muons. Muons do not interact strongly, so they do not undergo hadronic absorption, and, due to their relatively large mass, the electromagnetic showering they produce is negligible. For these reasons muons are identified by reconstructing them in tracking systems placed downstream of iron shielding blocks where electrons and hadrons are almost completely absorbed. The bulk of the data used for this thesis uses the information provided by the Inner Muon Detector for muon identification of the data.

2.9 Outer Muon Detector

The Outer Muon Detector is used for the reconstruction of muons produced at large angles with respect to the beam direction. It is located immediately downstream of the analysis magnet, M2, and the Outer Electromagnetic Calorimeter, which are used as shielding material from electrons and hadrons. The charged tracks emerging from the filters are detected by resistive plate chambers, which have the advantage of being relatively insensitive to the magnetic field.

A resistive plate chamber is made of two plates at high potential difference separated by a gap which is filled with gas. The charged particle that travels through the

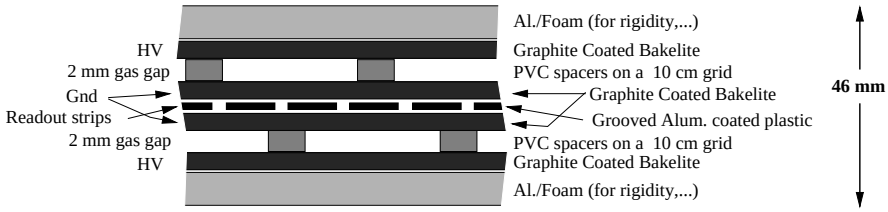

Figure 2.15: A schematic of the Resistive Plate Chambers for the Outer Muon Detector is shown.

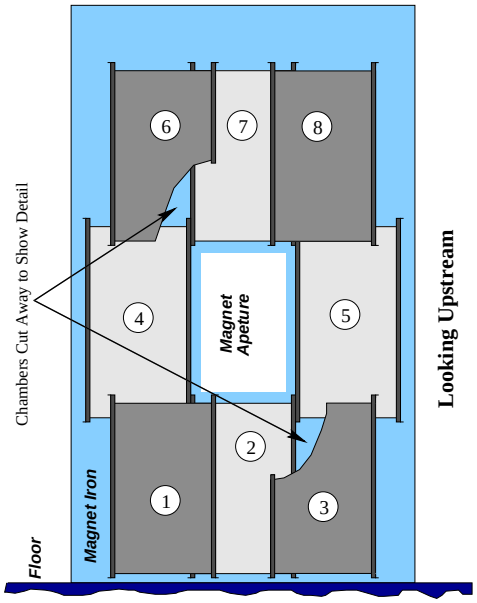

Figure 2.16: A schematic of the arrangement of the towers in the Outer Muon Detector is shown.

gap ionizes the gas and the freed charge is collected by readout strips. FOCUS uses double gap resistive plate chambers with readout strips in the center of the two gaps, as shown in Fig. 2.15. There are 24 RPC modules of 1 cm $\times$ 1.6 cm or 1 cm $\times$ 1.8 cm. The modules are grouped in eight towers (defined by the modules that are aligned along the z axis) with three chambers each (for the x, y and $+45^0$ directions). The towers are arranged around the aperture of M2 as shown in Fig. 2.16.

The plates are made of graphite coated bakelite, which has a high resistivity ($10^{11}\Omega$·cm). The 2.9 cm wide aluminum coated plastic readout strips are placed between the bakelite plates with a 2 mm gap from each other. The strips are cut in half along the long axis. Each four adjacent strips are OR'd together, so that the number of output channels per module is limited to 13–16. This results in a resolution of about 12 cm, which,given the multiple Coulomb scattering in M2, is adequate.

The region of ionization avalanches is limited by the high resistance of the plates and the use of a "quenching" gas. Due to the high operating voltage (∼kV), the break-down limit is often reached. The avalanches are caused by the ultra violet photons emitted as electrons recombine with ions. A quenching gas absorbs these photons and disperses their energy. The gas used for FOCUS was a mixture of 71% argon, 16% CO_2, 8% isobutane and 5% freon.

The Outer Muon system is also used in the trigger logic.

2.10 Inner Muon Detector

The Inner Muon system is used to detect muons with high momentum and small angle. The detector consists of three stations of scintillating hodoscopes (MH1, MH2 and MH3) placed at the end of the FOCUS apparatus. Each station is preceded by a block of steel (61 cm, 129 cm and 68 cm long from the most upstream to the most downstream), which, in addition to the 126 cm of steel of the hadron calorimeter, filters particles other than muons. The detector layout is shown in Fig. 2.17. Each station has

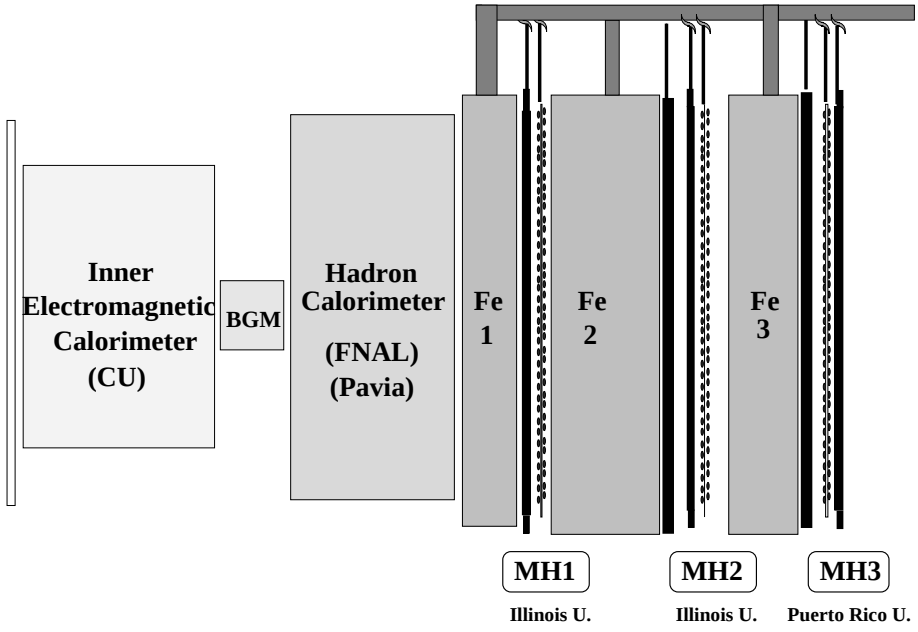

Figure 2.17: Layout of the Inner Muon system and the calorimeters that precede it. The institutions responsible for the detectors are also shown.

Station	Pitch	Number of counters		
		x/u	y/v	Total
MH1	5 cm	84	126	210
MH2	8 cm	52	78	130
MH3	10 cm	54	54	108

Table 2.6: The properties of the Inner Muon Arrays are shown. x and y apply to MH1 and MH2; u and v apply to MH3.

two views: x and y for MH1 and MH2, u and v for MH3 (which corresponds to $\pm 30°$ with respect to the beam direction). A schematic of the counters layout is shown in Fig. 2.18.

The stations have scintillating strips with a large pitch, since position resolution is not important due to multiple Coulomb scattering in the filters. The pitch and number of counters for each station are shown in Table 2.6

2.11 Trigger

The trigger is the electronic logic that makes an on–line selection of interesting events. This on–line process is necessary in order to reduce the event rate (about 10 MHz) to the data acquisition rate of 1 kHz. The main background is electromagnetic e^+e^- pair production, which has a cross section about 500 times larger than the hadronic cross section (and 50,000 times larger than the charm cross section). Pairs are produced at small angles and do not deposit energy in the hadronic calorimeter, so these events are mainly rejected by requiring wide angle tracks and setting a threshold for the energy measured in the hadronic calorimeter.

The trigger consists of two main steps. The first level trigger, called "Master Gate", takes 200 ns. During the first 160 ns the information is transferred from the spectrometer, and in the last 40 ns the decision is made. If the event passes the Master Gate, then a second level trigger begins. This takes 1.2 μs and, if the event passes the requirements, it sends the signal for writing the data on magnetic tape (process that

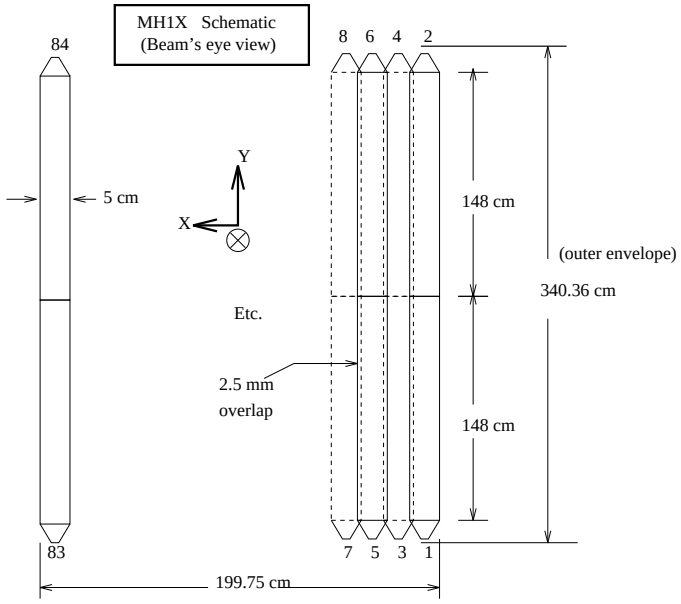

(a) MH1X. The arrangement of MH2X is similar.

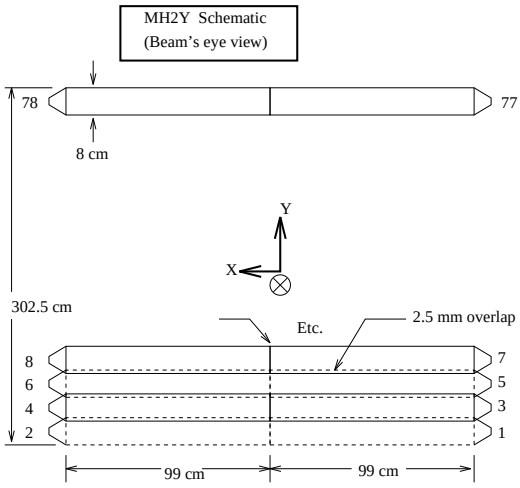

(b) MH2Y. The arrangement of MH1Y is similar.

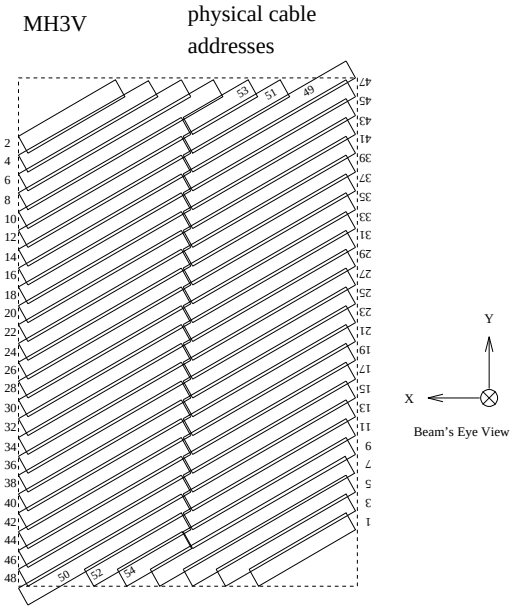

(c) MH3V. MH3U is identical except the counters are rotated by 90^0.

Figure 2.18: Schematic of the counter arrangements of the Inner Muon Hodoscope arrays.

takes about 35μs). If the event is rejected then the system is reset in 1μs.

2.11.1 First Level Trigger: the Master Gate

Different combinations of signals from the detectors have been used for different Master Gate triggers. Most of the data (including the one used for the analysis presented in this thesis) has been collected using the hadronic Master Gate trigger (MG1), which combines the signal from five detectors:

- **TR1**: This is a scintillator counter with PMT readout that lies between the last TSSD station and the first SSD station. This detector signals that an event with production of charged tracks has occurred.

- **TR2**: This is a scintillator detector with PMT readout made of four counters downstream of the last SSD station. This detector signals that an event with production of charged tracks has occurred, and that it enters within the acceptance of M1

- **H** $\times$ **V**: This detector (see Fig. 2.19 a) consists of 36 scintillator counters placed between C3 and the Inner Electromagnetic Calorimeter. It detects charged particles produced at relatively wide angles with respect to the beam direction. In order to avoid counting e^+e^- pairs, it has a central gap along the vertical direction. The detector has two signals: $(H \times V)_1$ and $(H \times V)_2$, signaling that at least one or two charged particles have been detected, respectively.

- **OH**: This detector (see Fig. 2.19 b) consists of 24 scintillator counters placed in front of the Outer Electromagnetic Calorimeter. A vertical gap and an aperture that matches the aperture of M2 allows e^+e^- pairs to pass through. The OH_1 signal guarantees that at least one charged particle with wide opening angle has been detected.

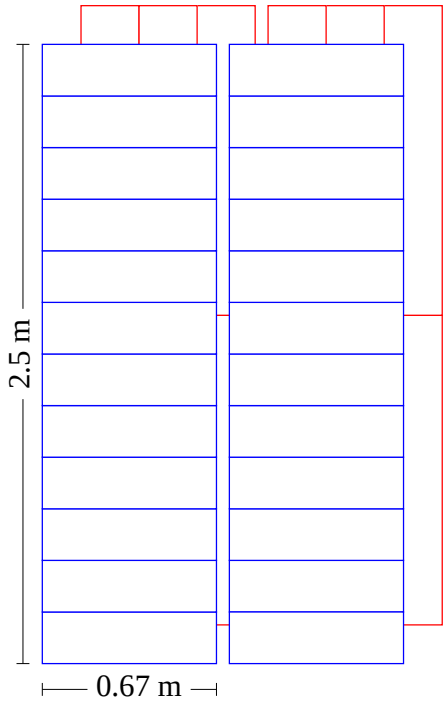

(a) $H \times V$

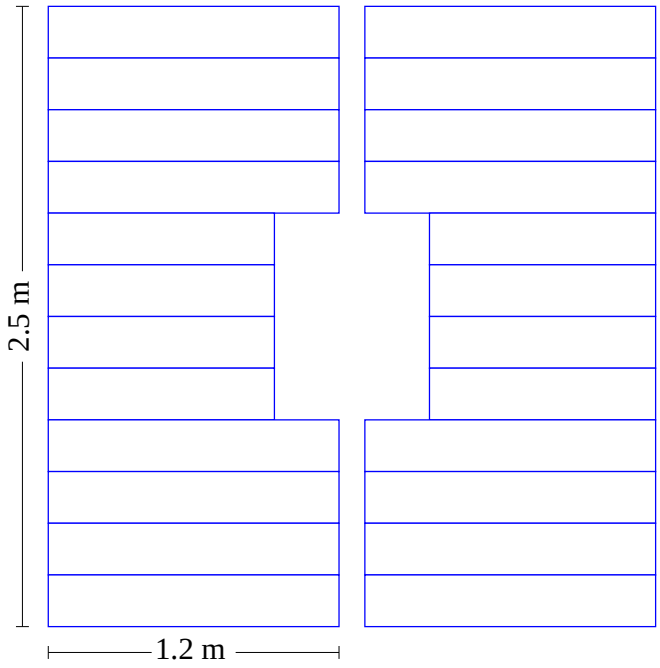

(b) OH

Figure 2.19: A schematic of the $H \times V$ and OH hodoscope arrays.

Trigger	Definition	Physics signal
MG1	TR1·TR2·2B·E_{HI}	Hadronic trigger
MG2	TR1·TR2·2B·IE_2	$J/\psi \rightarrow e^+e^-$
MG3	TR1·TR2·$[\mathrm{IM}_1 + \mathrm{OM}_1] \cdot E_{\mathrm{LO}}$	Semi-muonic decays
MG4	TR1·TR2·2B·$[\mathrm{IM}_2 + \mathrm{OM}_2 + \mathrm{IM}_1 \cdot \mathrm{OM}_1]$	$J/\psi \rightarrow \mu^+\mu^-$
MG5	TR1·TR2	e^+e^- pairs (PS)
MG6	TR1·TR2·2B	Two-body events (PS)
MG7	TR1·TR2·$[\mathrm{IM}_1 + \mathrm{OM}_1]$	One-muon events (PS)

Table 2.7: The logic for the seven Master Gate triggers are shown. Master Gates denoted (PS) are prescaled and are used for calibration. The term 2B stands for $(H \times V)_2 + [(H \times V)_1 \cdot OH_1]$.

- **$\mathbf{E_{HI}}$**: This signal comes from the Hadron Calorimeter, and it is used to reject events with hadronic energy lower than a given threshold.

The hadronic Master Gate requirement is given by the following logical combination of the five signals:

$$\mathrm{MG1} = \mathrm{TR1} \cdot \mathrm{TR2} \cdot [(\mathrm{H} \times \mathrm{V})_2 + (\mathrm{H} \times \mathrm{V})_1 \cdot \mathrm{OH}_1] \cdot \mathrm{E_{HI}}$$

In total there are seven Master Gate triggers, which are summarized in Table 2.7, where the other individual inputs are:

- E_{LO}: Hadronic energy over a lower threshold than for E_{HI}.
- E_{IE}: Electromagnetic energy over a high threshold.
- IE_2: At least two hits in the Inner Electromagnetic Calorimeter.
- IM_1: At least one hit in the Inner Muon detector.
- IM_2: At least two hits in the Inner Muon detector.
- OM_1: At least one hit in the Outer Muon detector.
- OM_2: At least two hits in the Outer Muon detector.

Trigger	Definition	Physics signal
TRIG1	MG1·$E_{\text{IE-2}}$·MULT4	Hadronic trigger
TRIG2	MG2·$(H \times V)_2 \cdot E_{IE}$	$J/\psi \rightarrow e^+e^-$
TRIG4	MG4·$\text{IM}_2 \cdot (H \times V)_2$·!(AM·AMD)	J/ψ, inner only
TRIG5	MG5	Prescaled MG5
TRIG6	MG6	Prescaled MG6
TRIG8	MG1	Prescaled MG1
TRIG9	MG4·OH·OM_2·MULT2·!(AM·AMD)	J/ψ, outer only
TRIG11	MG4·IM_1·OM_1·MULT1·$(H \times V)_1$· IM(E+W)	J/ψ, inner/outer

Table 2.8: The logic for different second level trigger that were used during the data tacking are shown.

2.11.2 Second Level Trigger

The second level trigger uses information from detectors that are in general too slow to be included in the first level Master Gates. Also for the second level trigger more complicated logic was used for different physics signals. Some triggers are used for detector monitoring. The bulk of the data has been collected using the hadronic second level trigger. The signal used are:

- **MULTn**: at least n tracks with sufficient number of hits have been detected by the MWPC.
- **AM·AMD**: halo muons are vetoed using two arrays placed between the radiator and the experimental target.
- **IM(E+W)**: Vetoes hits in both halves (west and east) of the inner muon triggers.
- $\mathbf{E_{IE-2}}$: At least two hits above threshold in the Inner Electromagnetic Calorimeter

Some second level triggers that were used during the data tracking are shown in Table 2.8.

2.12 Data Acquisition

The Data AcQuisition (DAQ) system has the task of digitizing and recording the analog signals that come from the detectors and writing the information to tape. Data from different formats are merged into one stream and the output is recorded on 8 mm magnetic tapes.

The performance of the FOCUS DAQ was excellent, the events were collected at a rate of about 30,000–40,000 events per 20 s spill with a typical event size of 4 kB. The fraction of time spent waiting for the next event ("livetime") was about 85%–90% and the readout time was about 35 μs. A more detailed description of the DAQ system is given in [35]

Chapter 3

The DATA Skims

3.1 Introduction

During the data collection 6.5 billion events were triggered and the data, which amounts to about 30 TB, was stored on 6000 8 mm "Exabyte" magnetic tapes. In order to make this raw data manageable for the physics analyses the data were processed and divided into smaller sets through three steps : "Pass One", "Skim One" and "Skim Two".

Pass One reconstructs the raw data saved on tape by the DAQ system. With Skim One the reconstructed data is divided into a set of 6 Super–streams corresponding to broad physics categories. Each Super–stream is divided into multiple Sub–streams with the Skim Two process. Figure 3.1 is an overview of this three step process, which is described in more detail in this chapter.

3.2 Pass One

Pass One uses the raw data from the detectors (i.e. the hits in the tracking detectors, or the energy deposited in the calorimeters) to perform a topological and kinematical reconstruction of the event: the track direction and momentum, the vertices coordinates are reconstructed and the particle identification for each track is performed. The reconstruction techniques are described in detail in the next chapter. During Pass One D decays called golden modes ($D^0 \to K^-\pi^+\pi^-\pi^+$, $D^0 \to K^-\pi^+$ and $D^+ \to$

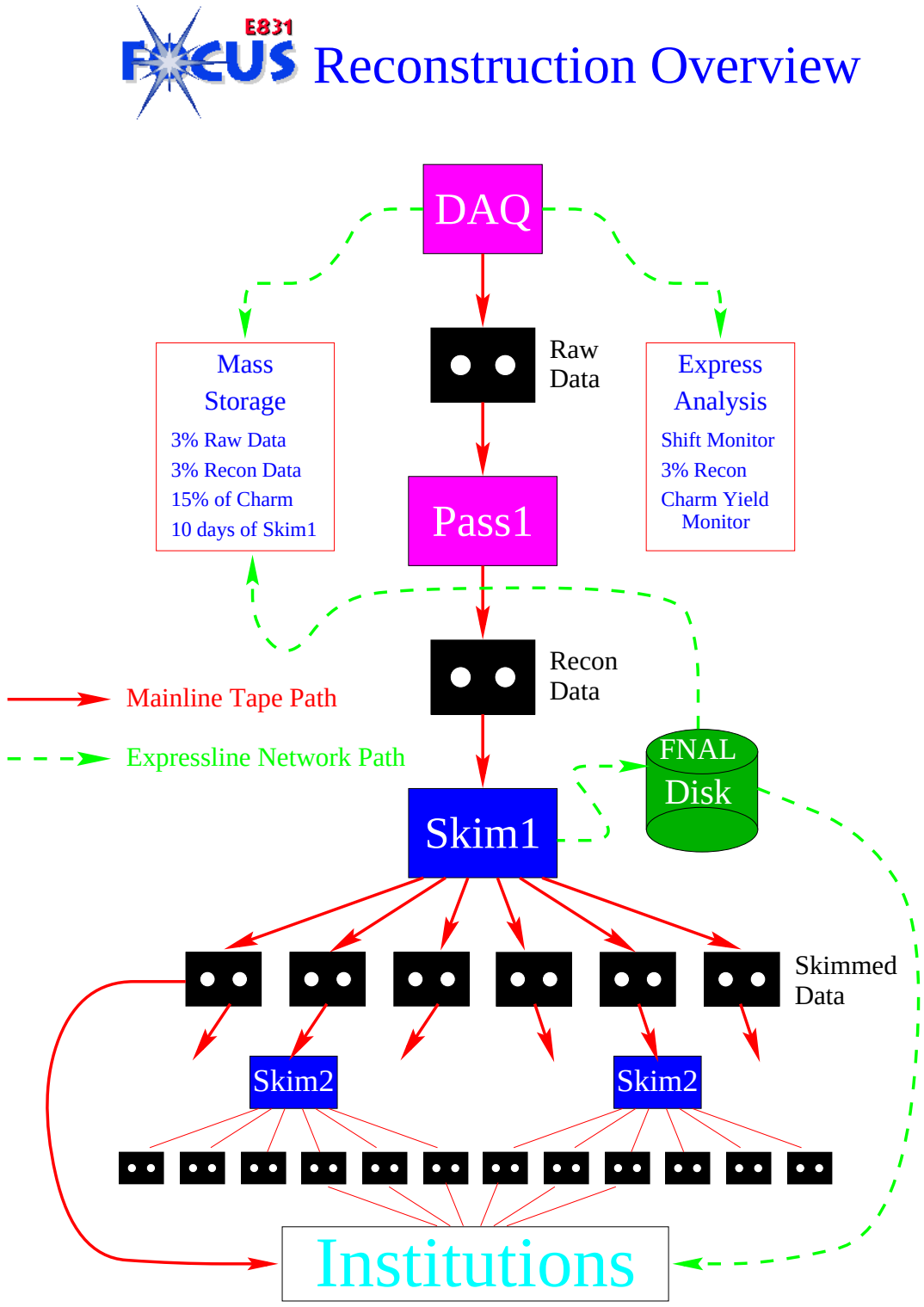

Figure 3.1: The Data Reconstruction Overview is shown.

$K^-\pi^+\pi^+$) were reconstructed with the purpose of monitoring the performance of the process.

A considerable computing effort was necessary to perform this initial reconstruction process. Eight computing "farms" were used, for a total of up to 90 computing nodes. Each farm consists of a server node and ten worker nodes that perform the reconstruction in parallel. The Fermilab software Cooperative Process Software was used for the transmission of data and control information among many processes running on multiple computers. The functioning of each farm is schematically shown in Fig. 3.2. The data is initially transfered from tape to disk, and read by the server node. This sends the information to the worker nodes for computation through a high speed network. Each worker node receives eighty events at the time, performs the computation, and sends the reconstructed data back to the server, requiring new data. A separate program transfers the information from disk to tape. The farm consists of SGI workstations (based on the MIPS R5 000 CPU) and IBM workstations (based on the IBM/Motorola PowerPC CPU). The average CPU maintained during Pass One was about 85–90%.

The Pass One process took almost one year, from January 1998 to October 1998. The larger fraction of computing time was taken by the reconstruction algorithms and the combination of shower reconstruction and particle identification. At this stage about 10% of the events were discarded due to reconstruction errors (e.g. too many hits) or by requiring very loose selection cuts (e.g. to have reconstructed at least one track in the SSD). The output of Pass One consists of 6000 magnetic tapes (one for each input tape) were the raw data is recorded along with the reconstructed data. In order to maintain the data flow proceed without delays, the reconstructed calorimetry information was not written on the output tapes.

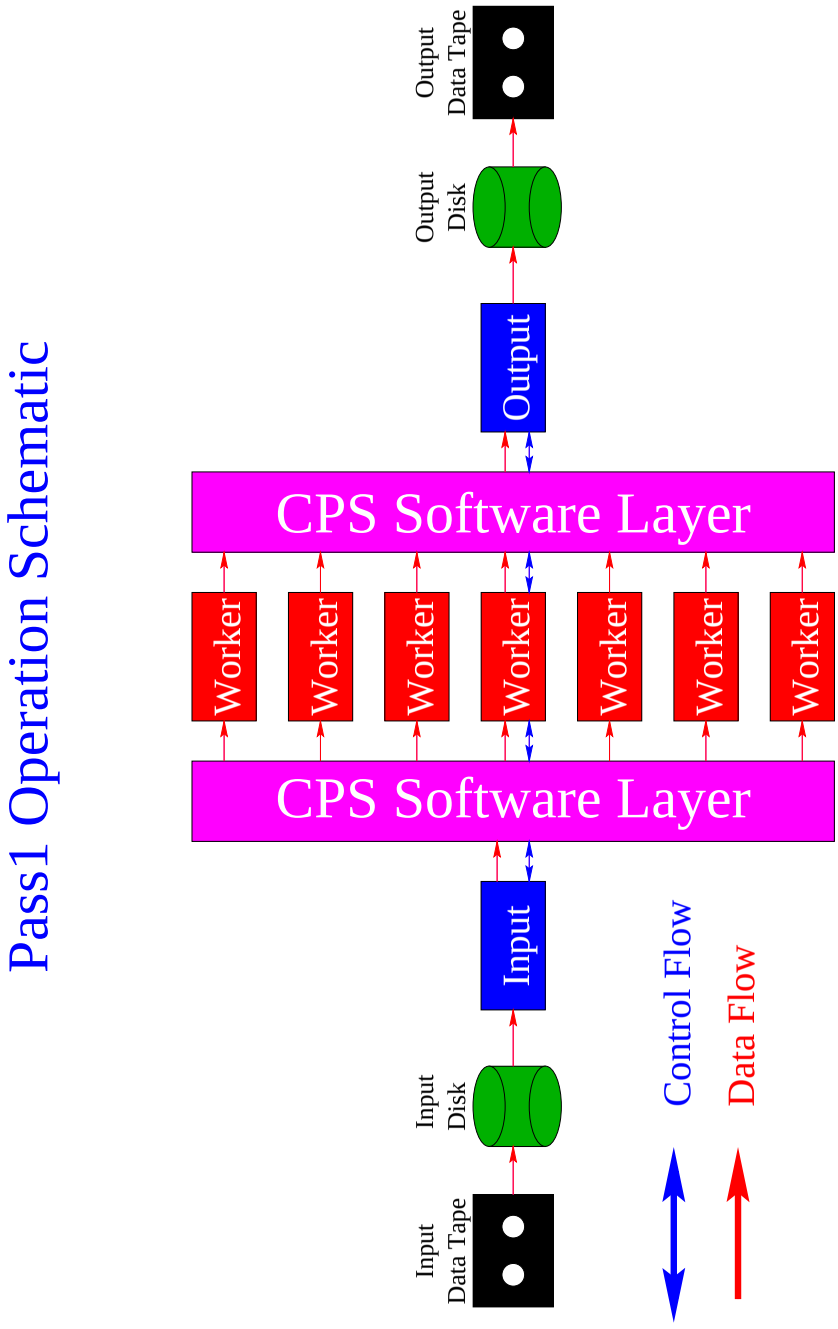

Figure 3.2: A diagram of a computing farm used for the data reconstruction in Pass One is shown.

3.3 Skim One

With the Skim One process the output of Pass One was divided into six sets, called "Super–streams", each corresponding to one or two broad physics topics. Skim One was run at two institutions, University of Colorado and Vanderbilt University. Both institutions used a computer farm with jobs running in parallel. University of Colorado used Alpha machines, while Vanderbilt used Linux machines. Both computer clusters had about 4000 MIPS (Millions of Instructions Per Second). The data processing method was similar to Pass One, except that each job reconstructed 40,000 events instead of 80. A diagram of the process ran at Colorado is shown in Fig. 3.3, the picture is a good representation also for the Vanderbilt process.

During Skim One the calorimetry reconstruction was again processed, since the relative reconstructed information was not output in Pass One, and new, improved routines were run for the Čerenkov identification and for the reconstruction of the decays $K_s \to \pi^+\pi^-$ and $\Lambda^0 \to p\pi^-$. The Skim One process was run from October 1998 to February 1999, the main limitation in speed deriving from the time necessary for tape reading and writing. About 50% of the data were retained after Skim One.

3.4 Skim Two

Skim Two is the split of the Super–streams into Sub–streams corresponding to more specific physics topics. For each Super–stream about 5–12 Sub–streams were generated. The process was run at five different institutions, each of which "skimmed" one Super–stream (two for the University of California at Davis), as shown in Table 3.1. The computing models for the different institutions were all similar to the one for Pass One. The Skim Two started in January 1999 and was completed by the end of June 1999.

The data for the analysis presented in this thesis comes from the Skim Two Sub–

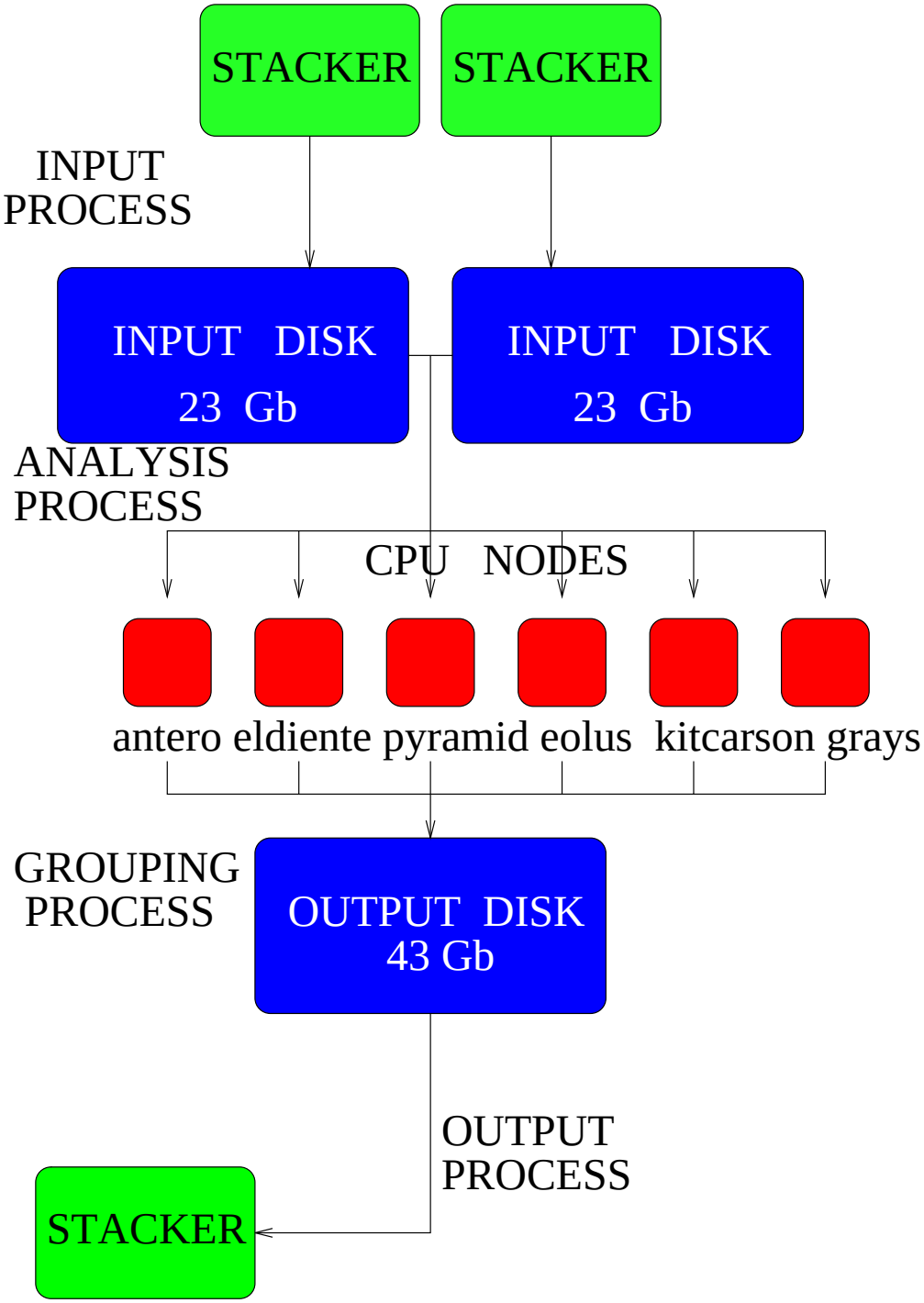

Figure 3.3: The computing process ran at the University of Colorado for Skim One.

Table 3.1: Institutions that run Skim Two and physics topics for the division of each Super–stream into Sub–streams.

Super Stream	Physics Topics	Skim2 Institution
1	Semi-leptonic	Puerto Rico
2	Topological vertexing and K_S^0	Illinois
3	Calibration and rare decays	CBPF, Brazil
4	Baryons	Fermilab
5	Diffractive (light quark states)	California, Davis
6	Hadronic meson decays	California, Davis

stream FSK, where events with at least one K_S^0were selected. The FSK Sub–stream was produced at the University of Illinois at Urbana–Champaign ant it consists of 212 magnetic tapes (corresponding to about 1 TB of data). I performed two consecutive skims to reduce this data to about 70 GB; this data selection is described in Chapter 5.

Chapter 4

Data Reconstruction

In this chapter the techniques used for transforming the raw information collected in the detectors into data records that can be used for physics analysis will be described. We explain the algorithms for reconstructing charged particles in the spectrometer, we describe two methods of determining the vertices position, we also explain the reconstruction of hyperons and neutral kaons and we discuss different particle identification methods (using the Čerenkov counters, the muon systems, and the calorimeters).

4.1 Tracking

Tracking (or track finding) is performed using pulse height in strips above threshold in the SSD and using wires which are on in the MWPC . Initially, the reconstruction is performed separately for the two systems, then a "linking" procedure combines segments in the two systems. Linked segments which have a good confidence level for the hypothesis of belonging to the same particle are assigned to a track.

4.1.1 SSD Tracking

Tracking in the SSD system is performed in a three–step process: first clusters of hits are formed, then the projections in the three measured directions are found, and then the projections are combined to construct the track. The track parameters are the slope and intercept in the coordinate system of the granite structure that supports the

experimental target.

The hit clusters are formed using hits from up to three adjacent strips. By comparing the total collected charge (given by the sum of all channels in the cluster) to the number expected from a Minimum Ionizing Particle (MIP) it is possible to determine if a cluster was formed by one or two tracks. The two track case is most likely an e^+e^- pair event (the two tracks in this event have very small separation compared to the detector resolution).

For each of the three views, the clusters are used to find the projection in the measured direction. The projection in a given direction is found from the fit to a straight line of the clusters in that view (taking all possible combinations). A combination is kept if $\chi^2/(\text{d.o.f.}) < 3$ (d.o.f. being the number of degrees of freedom). Clusters can be shared by 3–plane projections and in the first plane of 4–plane projections. The projection must be found in at least three of the four planes for each view.

All the possible combinations of three projections (one for each view) are used to form a track. A loose requirement for the fit is applied, $\chi^2/(\text{d.o.f.}) < 8$. An arbitration based on the best $\chi^2/(\text{d.o.f.})$ is applied for shared projections between tracks. When groups of tracks have almost identical parameters they are arbitrated to a single track.

The resolution on the direction is given by the detector resolution and by Multiple Coulomb Scattering which depends on the particle momentum. The resolution in the horizontal and vertical direction for tracks reconstructed in the central part of the SSD planes is:

$$\sigma_x = 11.0\ \mu\text{m} \sqrt{1 + \left(\frac{17.5\ \text{GeV/c}}{p}\right)^2}$$

$$\sigma_y = 7.7\ \mu\text{m} \sqrt{1 + \left(\frac{25.0\ \text{GeV/c}}{p}\right)^2}$$

In the outer region, where the strip pitch is larger, the resolution is twice as large. The resolution is better in the y direction because all the three views provide information in this direction, while only two provide information on the x direction.

Once the SSD track is formed, its direction is extrapolated upstream for a refit using hits in the TSSD system. Two refits of the track are performed. The first refit uses the hits in TSSD2 that lie within a three sigma radius of the track (which usually corresponds to about 1–2 strips). If the first refit is successful (i.e. matching hits are found), a second refit is performed. This second refit uses hits in TSSD1 in addition to the TSSD2 hits used in the first refit. The information on the track parameters is saved for the three fits (using only the information from the SSD system, using also TSSD2, and using also TSS1 and TSSD2).

4.1.2 PWD Tracking

Track reconstruction in the MWPC system is based, like the SSD system, in finding the single view projections and extracting the track parameters (slope and intercept) from a fit to a straight line. There are three stations between the magnets and two stations downstream the magnet M2.

First, the projections along the x, y, u, and v views are formed independently. The projections are then used to reconstruct the track in three dimensions. For the tracks that travel through M2, the momentum is included as a fit parameter, and a first estimate for its value is found. The fit includes magnetic corrections for the fringe field and for the spatial variation of the magnetic field inside the magnet.

The reconstructed track must have hits in P0 and in at least two other chambers. The maximum number of missed hits is four, with a limit of two missing hits per plane. For events with a large number of hits the number of reconstructed tracks can be very high. To reject events where such track cluttering occurs, a maximum number of tracks per event of 30 is required (about 3.5% of the events are discarded by this requirement). Tracks are divided into two categories, the "stub" type, when the track has been reconstructed in the first 3 MWPC stations, and the track type, when the track has been reconstructed in all 5 MWPC stations. An additional type with very

poor resolution is given by tracks that are outside the geometrical acceptance of P2. The unused hits in the x direction of P0 and P1 are matched to the extrapolation of SSD tracks, then the projections in the other views are found. This category is required to have hits in all four views if they extend only to P0, or at in least three views if they extend to P1.

4.1.3 Linking

The linking procedure provides useful information for the physics analyses since long lived charged particles ($\mu^{\pm}$, $e^{\pm}$, $\pi^{\pm}$, $K^{\pm}$) generally travel through both the SSD and MWPC systems. A good requirement for these particles is to have "linked" tracks. A stub linking to an SSD track allows for a momentum measurement from the bend angle in M1. When selecting events with a muon in the final state, the comparison of the two momentum measurements in M1 and M2 helps reject background events where the muon results from a pion that decayed between M1 and M2.

The links are formed by extrapolating SSD and MWPC tracks to the center of M1 and by requiring consistency for the intercepts and the slopes. A global fit using the hypothesis that the two track segments are the same track is performed from the hits in the SSD and MWPC systems, and a loose requirement on χ^2/(d.o.f.) is applied. For each SSD track a maximum of two MWPC links are allowed (the links arbitration is based on the best χ^2/(d.o.f.)). An e^+e^- pair is normally reconstructed as a "double–link" track, since the two tracks are not resolvable in the SSD system, but they become separated after the magnets.

4.1.4 Momentum Measurement

Depending on the topology of the track, either the bend angle in M1 (linked stubs or linked 4–plane tracks) or the bend angle in M2 (5–chamber tracks) is used for the momentum measurement. The algorithms for the two categories are similar: the

particle trajectory inside the magnet is determined from the known magnetic field and the track parameters at both ends of the magnet. An iterative fit is performed where the momentum value and track parameters are free to float, one at the time and starting from the momentum. The fit ends when improved and stable values are found for both the momentum and track parameters.

The momentum resolution is dominated by Multiple Coulomb Scattering at low momentum and by the uncertainty on the track direction at high momentum. The resolution on the momentum measured in M1 and in M2 are given by:

$$\left(\frac{\sigma_p}{p}\right)_{M1} = 0.034 \times \frac{p}{100\ \text{GeV/c}} \sqrt{1 + \left(\frac{17\ \text{GeV/c}}{p}\right)^2}$$

$$\left(\frac{\sigma_p}{p}\right)_{M2} = 0.014 \times \frac{p}{100\ \text{GeV/c}} \sqrt{1 + \left(\frac{23\ \text{GeV/c}}{p}\right)^2}$$

A rough momentum estimate is also possible for unlinked stub–type tracks: the x projection is extrapolated to the target region and the closest vertex from this direction is assumed to be the origin of the track. If no vertex is found, the target center is taken. By knowledge of the origin point and the direction in the bend view after the magnet a low precision estimate of the momentum is made.

4.2 Vertexing

There are two primary vertex finding (or vertexing) algorithms, DVFREE and DVNUCL. The first method is used when no *a priori* information on the vertex location is available. The DVNUCL method is used in physics analyses where the direction of the charm particle is known (namely when all the daughter particles momenta are measured) and the charm particle flight direction is used as a *seed* track. For the decay mode studied in this thesis we use DVFREE, since, due to the undetected neutrino in the final state, we do not have a seed track.

4.2.1 DVFREE

The DVFREE algorithm begins with taking two SSD tracks (linked or not) and forming a χ^2 for the hypothesis that they originate from the same vertex. If $\chi^2 > 1$, the track combination is rejected and we search for a new combination. If $\chi^2 < 1$, other tracks are added one at the time so long as $\chi^2 < 1$. For N tracks forming the vertex, the χ^2 is given by:

$$\chi^2 = \sum_{i=1}^{N} \left(\frac{x - (x_i + x_i' z)}{\sigma_{x_i}} \right)^2 + \left(\frac{y - (y_i + y_i' z)}{\sigma_{y_i}} \right)^2 \tag{4.1}$$

where $x,\ y,\ z$ are the vertex coordinates, $x_i,\ y_i,\ x_i',\ y_i',\ \sigma_{x_i}$ and σ_{y_i} are the track intercepts, slopes, and errors. The vertex finding algorithm is repeated until all possible combinations of tracks forming a vertex with $\chi^2 < 1$ are formed. If the vertex is reconstructed upstream of TSSD1 (TSSD2), the SSD tracks are replaced with their refit tracks using the information from TSSD1 (TSSD1 and TSSD2).

For specific physics analyses the user can decide to exclude some tracks from the vertexing. For instance, in reconstructing the decay mode $D^0 \rightarrow K_S^0(\pi^+\pi^-)\pi^-\mu^+\nu$, we have excluded the muon and the pion tracks. Also each pion from the K_S^0 decay is removed, if it is reconstructed as a linked track. Vertexing is performed during the initial Pass One as the vertex is needed for finding other objects and for determining momenta (as seen in the previous section). This reconstruction is done without assuming any particular decay in the event, so it is performed using DVFREE. More than one vertex is usually found. Different criteria are used to determine the so called "event vertex". Normally either the highest track multiplicity vertex or the most upstream vertex is chosen as the primary vertex.

4.2.2 DVNUCL

DVNUCL is used when the charm decay has been fully reconstructed and a flight direction (seed track) of the charm particle is known. A least squares method similar to

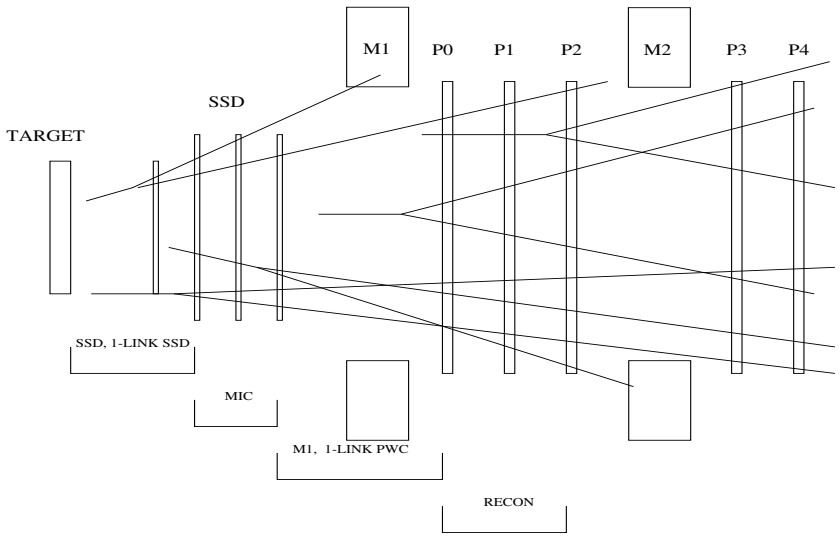

Figure 4.1: Different topologies for the decay of Vees are shown. The corresponding Vee type is indicated in the picture.

the one used in DVFREE is used to form a vertex, the difference with DVFREE being that the tracks must be verticized with the seed track. The tracks that are used to find the seed track are automatically excluded from the process, and the user can also exclude other tracks. DVNUCL yields a much better resolution than DVFREE.

4.3 Vees, Kinks, Ξ^-'s and Ω^-'s Reconstruction

Charm particles normally decay into final states that contain a strange particle (like K_s, Λ^0, Σ^+, Σ^-, Ξ^- and Ω^-). Different reconstruction techniques, which are described in detail in Reference [36], are used depending on the decay topology.

4.3.1 Vees

K_s and Λ^0 are reconstructed from the charged decays $K_s \to \pi^+\pi^-$ (BR=68.6%) and $\Lambda^0 \to p\pi^-$ (63.9%). For both modes the reconstruction algorithm is based on finding two oppositely charged tracks that make a good vertex. Because the geometry of the decay resembles a "V", these particles are normally called "Vees". Due to the relatively long lifetime of these particles ($\tau \sim 10^{-10}$ s), they can travel several meters

before decaying, and the decay range in the spectrometer is quite large. Fig. 4.1 shows the different categories that are reconstructed in FOCUS. We will describe briefly the algorithms that have been implemented for all these categories. In all cases the invariant mass of two oppositely charged tracks is computed first by assigning the π mass to both tracks to test the K_s hypothesis, and then by assigning the proton mass to the higher momentum particle to test the Λ^0 hypothesis. The selection cuts for the initial reconstruction are quite loose to allow different degrees of purity of the signal for different physics analyses.

Although reconstruction algorithms have been implemented for all Vee types, not all categories are used for the analyses. Several analyses use the SSD, M1, and One-link SSD Vees. For the analysis presented in this thesis we use the SSD and M1 Vee categories. The RECON and P34 Vees were implemented for E687, but they are not used in FOCUS. Due to a reduction in the beam energy, long–lived decays are less frequent, therefore RECON and P34 Vees are less frequent. Moreover, the number of fake RECON Vees increased in FOCUS compared to E687 due to the higher luminosity, which results in more noise in the chambers. MIC Vees are not used for FOCUS analyses because they require excessive computing time. MIC Vees are first found as M1 Vees, and then a search is performed for the remaining hits in the SSD . Singly–linked MWPC Vees are only used to reconstruct the decays $\Xi^- \to \Lambda^0\pi^-$ and $\Omega^- \to \Lambda^0 K^-$ as described in section 4.3.3.

As will be explained in the next paragraphs, it is often necessary to assume that the Vee has been produced at the primary vertex of the event, which can be a rather rough approximation. A "refit" procedure has been developed to improve the resolution on the mass and direction of the Vee. In this method, which is used at the physics analysis stage, the Vee is constrained to come from the charm decay vertex.

SSD Vees SSD Vees are normally K^0_S and Λ^0 particles that decay upstream of the second SSD station. They are reconstructed from oppositely charged, linked tracks

that originate from the same vertex. The Vee decay vertex is required to be downstream of the primary vertex of the event. If matching hits are found in the TSSD system, they are included in the track definition. Only hits downstream of the Vee decay vertex are used. Since the Vee normally has low momentum, the resolution (σ_m) on the di–pion mass is excellent, σ_m is about 3.6 MeV and 1.6 MeV for K^0_S and Λ^0, respectively. SSD Vees have excellent resolution on the Vee direction. This resolution is comparable to that of two combined tracks.

M1 Vees K^0_S and Λ^0 particles that decay downstream of the last SSD station and upstream of the first MWPC station are called M1 Vees. The two pion candidate tracks must be unlinked MWPC tracks. Depending on the nature of the two tracks, M1 Vees can be of the "track–track", "stub–stub" or "track–stub" types. For each of these sub–categories the decay vertex in the non–bend xz plane is found. An iterative fit is used to determine the y coordinate of the Vee decay vertex. For track–stub types this method allows a determination of the momentum of the stub daughter. For stub–stub types it is necessary to constrain the Vee to originate at the primary vertex of the event. With this constraint it is possible to evaluate the track momenta. A global fit using the full covariance matrix of the tracks and including multiple Coulomb scattering is performed to provide a better estimate of the Vee decay vertex and the Vee momentum. About 70% of all Vees belong to the M1 category. The mass and vertex resolution are not as good as for the SSD type and the resolution varies with the angle between the normal to the Vee decay plane and the magnetic field direction. The di–pion mass distribution has long, non–Gaussian tails. For this reason the K^0_S and Λ^0 candidates are selected not based on the reconstructed mass, but based on the "normalized reconstructed mass", which is the difference between the reconstructed mass and the nominal value divided by the calculated mass error σ_m. The normalized mass has a Gaussian distribution. The default requirement for M1 Vees is that the absolute value of the normalized mass is less than 5 (which corresponds to requiring that the reconstructed mass lies within

five standard deviations from the nominal mass). The average resolution σ_m varies from 5.9 MeV for track–track Vees to 6.6 MeV for stub–stub Vees.

RECON Vees RECON Vees are K_S^0 and Λ^0 particles that decay between P0 and P2. These high momentum Vees are not very prevalent in FOCUS, and they are not used for the physics analyses. The two pion candidates are reconstructed using the hits in P1, P2, P3, and P4 that have not been used in the global track finding process, which uses searches for hits in all the chambers. Depending on which MWPC stations have been used for the reconstruction, the track can be of the P1234, P123, P234, or P23 type. First, vertices in the xz plane using the projections of two tracks at a time are formed. Tracks that do not verticize with any other track are discarded. Then, projections in the bend views (U, V, and Y) are formed and matched to the projection on the xz planes to form tracks in three dimensions. Finally, tracks are combined two at the time to form the Vee candidate. The Vee decay vertex coordinates and the tracks parameters are fit parameters.

P34 Vees P34 Vees are the highest momentum Vees of all categories that are reconstructed. They decay between P3 and P4 in the magnetic field of M2. The pion candidates are formed from hits in P3 and P4 that have not been used in the global track finding. The efficiency for this category is low, since hits in the two planes can be erroneously assigned to other tracks. Also for this category, track projections are formed in the xz plane, and projections are combined pairwise. A projection is discarded if no match is found for it. Projections in the bend directions are found and combined with xz plane projections to make tracks in space. The Vee vector is constrained to the event primary vertex in order to find the momenta of the pion candidates.

One–link SSD Vees The One–link SSD Vees are K_S^0 and Λ^0 particles that decay before the second SSD station with one of the pions not entering the acceptance of P0. These Vees are reconstructed using a linked track and an unlinked SSD track. The primary vertex of the events is used as a constraint for the production point of the

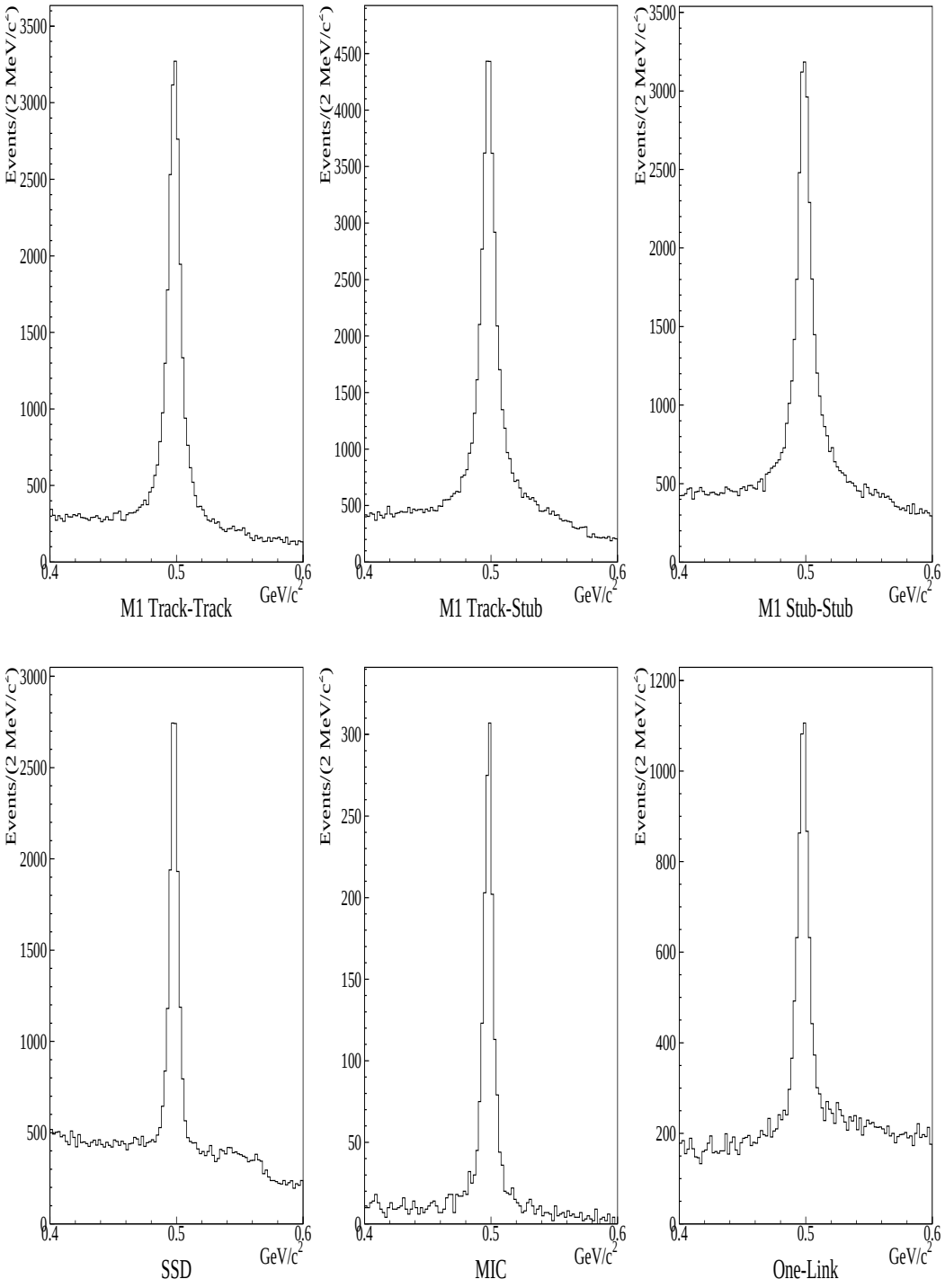

Figure 4.2: Di–pion invariant mass distributions for K^0_S candidates for different categories. For the analysis presented in this thesis we use the M1 Track-Track, M1 Stub–Stub, M1 Track–Stub and SSD categories. The SSD, MIC, and One–Link categories have the best mass resolution.

Vee. The line connecting secondary and primary vertices must lie in the same plane as the Vee decay plane. These constraints allow for us to determine the momentum of the unlinked daughter. The primary and secondary vertices are required to have a significance of separation greater than 10. This separation is calculated as the distance between the two vertices over the error on such distance (ℓ/σ_ℓ). The mass resolution for this type is about 4.7 MeV.

MIC Vees MIC Vees are $K_S^{0\prime}$ s and $\Lambda^{0\prime}$ s that decay between the second SSD and the last SSD station. Unlinked MWPC tracks are matched to unused hits in the SSD planes to form the pion candidate tracks. These tracks are then used to form the Vee decay vertex. The Distance of Closest Approach (DCA) is required to be smaller than a certain value, and it is used for arbitration in case two Vees share a common track. The resolution on the K_S^0 mass is 4.4 MeV.

Single–linked MWPC Vees Single-linked MWPC Vees decay between the SSD detector and P0 (like for M1 Vees), but they are formed by a linked track and an unlinked track. Their reconstruction algorithm is the same as for M1 Vees, and they are divided in the same three sub–categories. The K_S^0 sample has very high background contamination for this type, and it has never been used. This category is very important for $\Lambda^{0\prime}$ s, when the Vee is produced in the decays of Ξ^-'s and Ω^-'s.

Fig. 4.2 shows the invariant mass distribution of the two daughter pions for the six Vee types that are used in physics analyses: the three M1 sub–categories, the SSD, MIC and One–link types. The category M1 is the most copious, but the other three types have the best mass resolution.

4.3.2 Kink Reconstruction

Charged particles that decay into a neutral and a charged particle are called "Kinks" from the geometry of the reconstructed decay. The neutral particle goes undetected and a charged track that makes a vertex with another charged track having

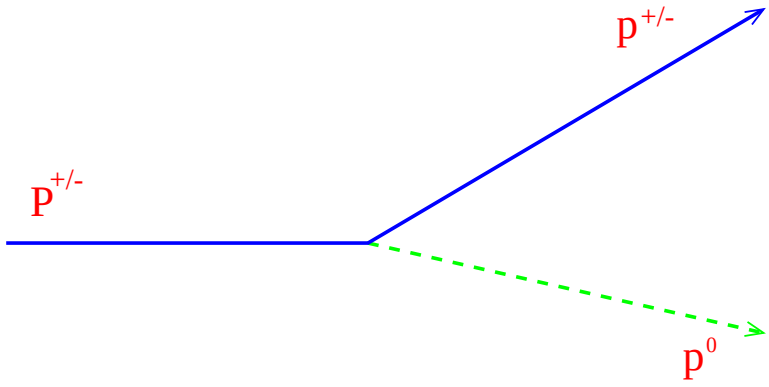

Figure 4.3: Schematic for a "Kink" decay. The neutral particle is not reconstructed.

a different direction is found, see Fig. 4.3. The FOCUS Kink algorithm is used for the reconstruction of Σ hyperons via the decays $\Sigma^+ \to p\pi^0$ (BR=51.6%), $\Sigma^+ \to n\pi^+$ (BR=48.3%), and $\Sigma^- \to n\pi^-$ (BR=99.8%).

The algorithm starts by finding an SSD track that points to the M1 aperture and a matching MWPC track that points back to the M1 aperture. Different categories are found depending on where the Σ decay occurs and on the nature of the MWPC track. The match is found by verticizing the two tracks in the x direction. For 5–chamber tracks the determination of the Σ momentum depends on the position of the decay vertex. If the vertex is upstream of M1, the Σ mass is assigned to the SSD track, and its momentum is determined up to a two–fold ambiguity. Different algorithms have been implemented for the arbitration, depending on the particular physics analysis. If the vertex occurs in the magnet, both the SSD and the MWPC tracks are traced through the magnetic field and the Σ momentum is determined by minimizing the distance of closest approach of the two particles. The 3–chamber case is only reconstructed for decays inside the magnet. First the x and z intersection of the two tracks is found, then the y value is determined from the SSD track parameters at the z of the intersection. Also in this case the nominal Σ mass is assigned to the SSD track.

Backgrounds with similar topologies are reduced by requiring Čerenkov identi-

fication for the proton, and finding a matching neutron from the hadron calorimeter shower reconstruction.

4.3.3 Ξ^- and Ω^- Reconstruction

The hyperons Ξ^- and Ω^- are reconstructed from the decays $\Xi^- \rightarrow \Lambda^0\pi^-$ (BR 99.9%) and $\Omega^- \rightarrow \Lambda^0 K^-$ (BR=67.8%). Most of the events are fully reconstructed from a Λ^0 candidate and an unlinked track. If no Λ^0 is found, or if the vertex between the Vee and the track is downstream of the Vee vertex, the hyperon is reconstructed as a MULTIVEE, where three unlinked tracks are used. If no MULTIVEE is found, then the hyperon is reconstructed as a Kink (to recover the events where the Λ^0 decays to $n\pi^0$). We will refer to both hyperons Ξ^- and Ω^- as "cascades" when no distinction is necessary.

Fully reconstructed cascades can be of two types depending on whether the decay is upstream (Type 1) or downstream (Type 2) of the SSD system. In both cases the reconstruction algorithm starts by finding a Vee that passes requirements for being a Λ^0. The main requirements are that the reconstructed mass lies within a certain window of the nominal mass and that Čerenkov identification on the highest momentum track in the Λ^0 be consistent with a proton.

For Type 1 cascades, the decay occurs upstream of the SSD and the Λ^0 is paired to a linked track. The two objects are required to make a good vertex, and that the vertex be downstream of the event vertex. The Ξ^- (Ω^-) mass is reconstructed by assigning the π^- (K^-) mass to the track.

For Type 2 cascades, since the cascade travels through the SSD system, its track can be reconstructed. For this category the Λ^0 is paired with an unlinked MWPC track. The vertex (with good confidence level) is found and the direction given by the sum of the momenta is matched to an unlinked SSD track.

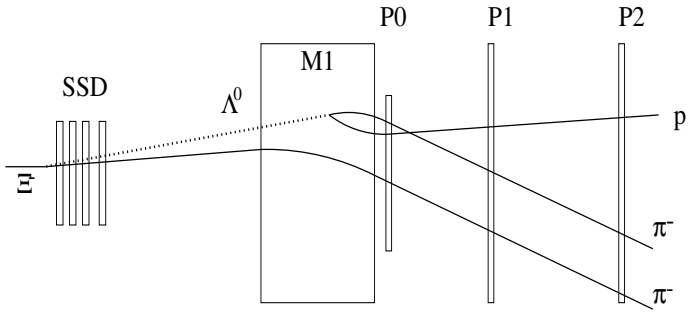

(a) Type 1 Cascade

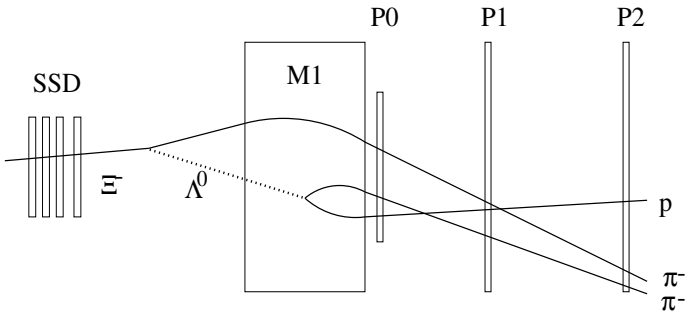

(b) Type 2 Cascade

Figure 4.4: Decay schematic for the two types of fully reconstructed cascades (Ξ^- or Ω^-). Type 1 decays upstream of the SSD system, and its Ξ^- track is not reconstructed. Type 2 decays downstream of the last SSD station, and its Ξ^-track is reconstructed.

4.4 Electromagnetic Shower Reconstruction

The reconstruction of electromagnetic showers is used for identifying electrons and for the reconstruction of neutral pions. For both inner and outer electromagnetic calorimeters the algorithm is based on forming clusters of deposited energy. In FOCUS electrons are produced at very high energies compared to their mass. Thus, the energy of a track measured in the electromagnetic calorimeters is used to identify it as an electron by requiring the ratio E/p to be close to unity.

4.5 Inner Electromagnetic Calorimeter Shower Reconstruction

In the Inner Electromagnetic calorimeter as many as twenty blocks can have deposited energy from an interacting particle. The largest fraction of energy, however, is normally deposited in only nine blocks. For this reason, each energy cluster is found using only nine blocks. First, the ADC counts from each block are converted into energy values (each block has its own conversion factor which varies over time). Next, the highest energy block is found and the eight blocks surrounding it are grouped into a cluster. The energy weighted average of the blocks coordinates (x_w,y_w) are found, for instance for the x coordinate:

$$x_w = \frac{\sum_{b=1}^{9} x_b E_b}{\sum_{b=1}^{9} E_b}$$

where block x coordinate and energy are labeled b. An improved cluster set of coordinates (x_c, y_c) is found following the procedure described in Reference [37]. The x_c coordinate (and similarly for the y_c coordinate) is given by:

$$x_c = 0.76 \ \mathrm{Sinh}^{-1}\left[\frac{x_w - x_{b1}}{S/2} \ \mathrm{Sinh}\left(\frac{S/2}{0.76}\right)\right] + x_{b1}$$

where x_{b1} is the x coordinate of the central block in the cluster and S is the dimension of the block. The process is repeated until all possible clusters are formed. Once a block

is assigned to a cluster, it cannot be used again.

For electron reconstruction each cluster is matched to a MWPC track. Only tracks within 6 cm from the cluster are associated with it. In principle, multiple tracks can be associated to the same cluster and vice versa, but this happens rarely due to this requirement. Calorimeter energy resolution is normally expressed as a constant term plus a term that improves with energy like $1/\sqrt{E}$. In FOCUS the average electron energy is so large that it is difficult to evaluate the energy dependent term. The constant term dominates the energy resolution, which is approximately 5%. The average resolution between the track and the cluster is about 6 mm.

Fig. 4.5 shows the E/p distribution for electron candidates for tighter requirements on the parameter IEID. This identification parameter provides information on the E/p ratio (IEID$\geq$10 corresponds to E/p in the window 0.8–1.25) and on the confirmation of the electron hypothesis from the Čerenkov system.

4.6 Outer Electromagnetic Calorimeter Shower Reconstruction

Lower momentum photons and electrons are also reconstructed from the energy deposited in the Outer Electromagnetic Calorimeter. In this detector energy clusters are formed, the averaged position is determined, and matching MWPC tracks (in this case stub–type tracks) are found. The energy of the cluster is found by summing the energy of the counters associated with it. The energy resolution for the OE is about $3\%+15\%/\sqrt{E\ (\mathrm{GeV/c^2})}$, while the position resolution varies from 9 mm at 3 GeV/c^2 to 3 mm at 10 GeV/c^2.

4.6.0.1 π^0 Reconstruction

Clusters with no associated tracks are called "neutral" clusters and can be used for neutral pion reconstruction. The neutral pion is reconstructed from the decay $\pi^0 \to \gamma\gamma$, which is assumed to decay at the center of the target. Cluster pairs are a candidates

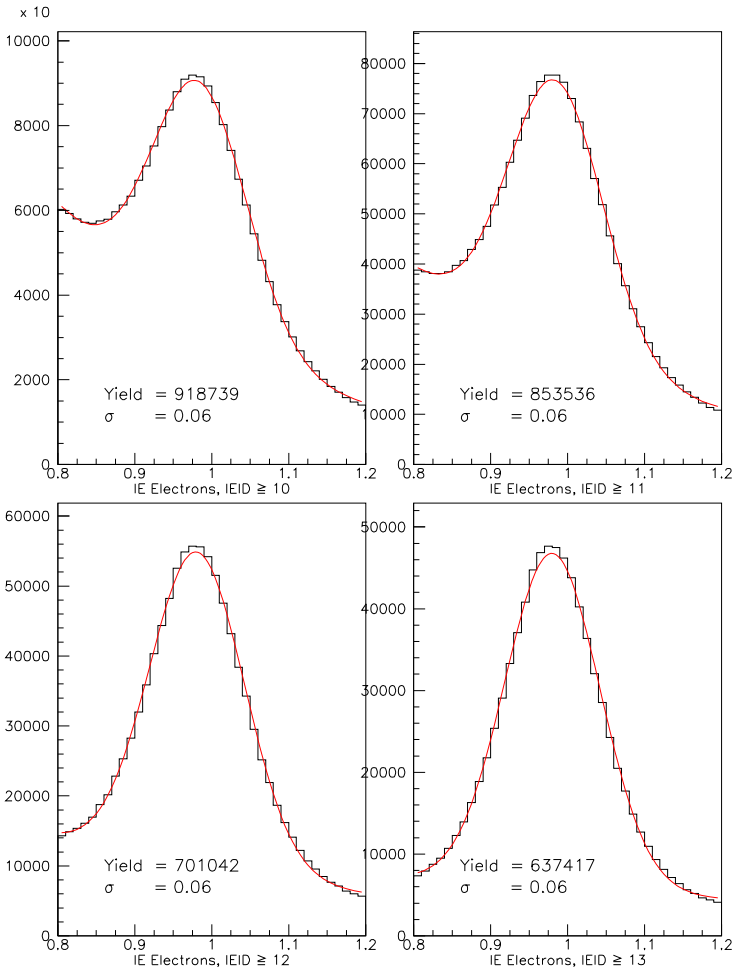

Figure 4.5: E/p distribution for electron candidates. The energy is measured in the Inner Electromagnetic calorimeter, the momentum is measured from the bend angle in the magnets.

for the two daughter photons. From the energy of the clusters the photon momenta are found and the pion mass is calculated. The two photons can be reconstructed in either the same calorimeter or in two different ones, accordingly there are three possible categories for the reconstructed pion: IE–IE, OE–OE, or IE–OE.

4.7 Neutral Hadron Shower Reconstruction

The reconstruction of neutral hadrons in the HC is used to find confirming neutrons for the Kink reconstruction. Clusters in the HC are associated with neutral clusters in the Inner Electromagnetic calorimeter, since approximately 80% of the hadrons that travel through this detector undergo a nuclear interaction in the material and produce a "pre–shower". The total energy of the hadron is given by the sum of the energy of the two clusters reconstructed in the two detectors. The resolution on the energy is found to be $0.86\% + 85\%/\sqrt{E}$.

4.8 Čerenkov Identification

Čerenkov identification of electrons, protons, charged pions and kaons is performed using the CITADL [30] algorithm (Čerenkov Identification of Tracks by an Algorithm using Digital Likelihood). While the Čerenkov hardware is essentially the same as the previous experiment E687, the identification software is a great improvement upon the one used in E687, LOGIC.

For each charged track that has been reconstructed in the MWPC system, the CITADL algorithm builds a log–likelihood variable W_α for the four hypotheses that the track is left by a particle $\alpha = e$, π, K, p. The on/off status of each cell is used, rather than the pulse height. For a particle of momentum p, one can calculate the $\beta = 1$ cone for each particle hypothesis (i.e. for each hypothesis on the mass of the particle, to which corresponds a β value). For each cell within the cone let μ be the number of expected photoelectrons and P_{ON} (P_{OFF}) the Poisson probability of firing (not firing)

is:

$$P_{ON} = 1 - e^{-\mu} \tag{4.2}$$

$$P_{OFF} = e^{-\mu} \tag{4.3}$$

The log–likelihood variable for the hypothesis α is given by:

$$W_\alpha = -2 \sum_j \log P_j \tag{4.4}$$

where the sum is over the cells within the $\beta = 1$ cone and the probability P_j has two possible values: $P_j = P_{ON}$ if the cell is ON and $P_j = P_{OFF}$ if the cell is OFF (for this reason it is called a "digital" likelihood). Cells that are inside the Čerenkov cone of more than one track are excluded from the sum.

The assumption so far is that a cell fires only in response to Čerenkov radiation. The CITADL algorithm in fact takes into account random firing. The probability for a cell to fire for reasons other than Čerenkov light has been calculated from the rate of firing in cells outside the $\beta = 1$ cone of any track in the event. This probability is higher for central cells, that are close to the beam axis. Fig. 4.6 shows a plot of the accidental rate versus cell number in C2 for a small fraction of data (corresponding to a single run of the experiment). The firing probability for a given cell therefore given by:

$$P_{ON} = P_{RND} + (1 - e^{-\mu}) - P_{RND} \cdot (1 - e^{-\mu}) \tag{4.5}$$

where P_{RND} is the random firing probability for that cell. P_{OFF} is evaluated using the obvious relation $P_{OFF} = 1 - P_{ON}$.

Particle identification is performed by comparing the W, or "Wob", variable values for each hypothesis. For instance when identifying a pion we normally require that the pion hypothesis is either the best hypothesis or does not differ by much from the best hypothesis. This is achieved by requiring $\min(W) - W_\pi > -n$, where n is a positive value, usually between 3 and 6. Background contamination from misidentifying

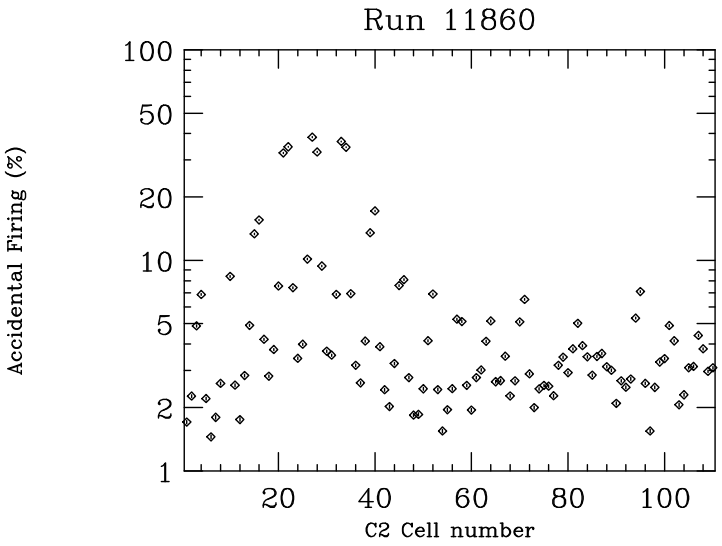

Figure 4.6: Percentage of accidental firing rate versus cell number in C2. For cells located near the beam axis the accidental rate is almost 40%, while it is only a few percent for the other cells.

a kaon as a pion is rejected by requiring that the pion hypothesis is favored over the kaon hypothesis by a certain number N of likelihoods units, i.e. $W(K) - W(\pi) > N$. The standard kaon identification is similarly performed by requiring $W(\pi) - W(K)$ to be greater than a certain value.

The Čerenkov identification performance was tested using high statistics channels. The decay $K_s \to \pi^+\pi^-$ was used for pion identification studies, the decay $\Lambda \to p\pi^-$ for proton and low momentum pion identification studies, and the decay $\Phi \to K^-K^+$ for kaon identification studies. The performance was investigated on a run by run basis. The $K_s \to \pi^+\pi^-$, with about 15,000 events per run, was used for a photoelectron recalibration of almost all 300 cells. Also the golden mode charm decays ($D^0 \to K^-\pi^+\pi^-\pi^+$, $D^0 \to K^-\pi^+$, and $D^+ \to K^-\pi^+\pi^+$) were used for monitoring the CITADL performance. Figure 4.7 shows the effectiveness of Čerenkov cuts in reducing background contamination in the sample $D^0 \to K^-\pi^-\pi^+\pi^+$. The signal with no Čerenkov requirement is compared to the signal with increasing $W_\pi - W_K$ values for the kaon identification.

The CITADL algorithm provides excellent particle identification for FOCUS. Two features of CITADL are the reason for the great improvement over LOGIC from E687. The old algorithm based the identification on the overall firing status of C1, C2, and C3, returning a single identification indicating whether or not the track was consistent with the four hypotheses (electron, pion, kaon and proton). This method is much less flexible than the log–likelihood–based method of CITADL. The second feature that provides a great improvement is the inclusion of random firing in the expected Čerenkov radiation pattern.

4.9 Muon Reconstruction

Muons are reconstructed from matching MWPC tracks to hits in the inner or outer muon systems. A confidence level for the hypothesis that the track belongs to a muon is determined by fitting the track to the hits. At the Skim 1 level, muon candidates

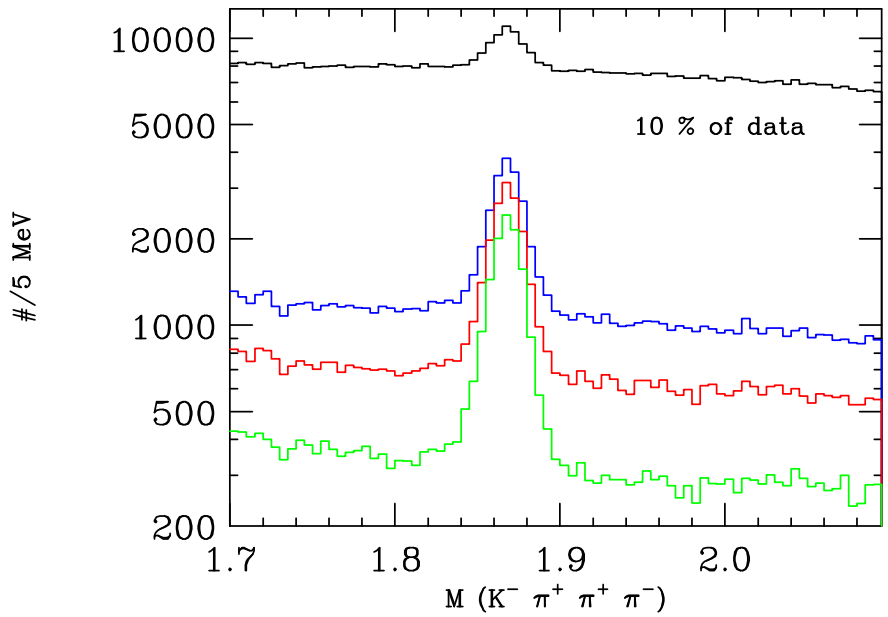

Figure 4.7: Invariant mass distribution $M(K^-\pi^-\pi^+\pi^+)$ for the decay $D^0 \rightarrow K^-\pi^-\pi^+\pi^+$ for different kaon identification requirements. From top to bottom: no requirements; $W_\pi - W_K > 0$; $W_\pi - W_K > 2$; $W_\pi - W_K > 2$ and $W_K - W_\pi > -2$ for the pion candidates. The ratio of signal events over background events increases dramatically. The plot is semilogarithmic.

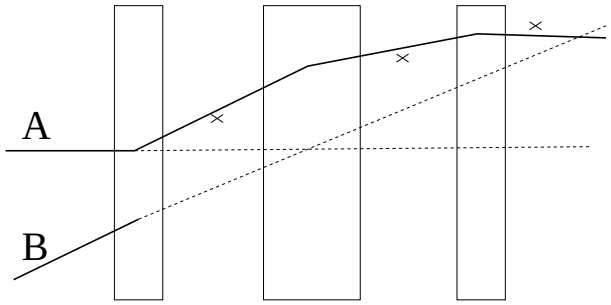

Figure 4.8: A schematic for the importance of including multiple Coulomb scattering effects in the confidence level evaluation. Solid lines indicate the actual trajectory. A is a real muon that leaves the hits indicated with crosses, B is absorbed in the filter. Dashed lines indicate the track extrapolation without including multiple Coulomb scattering effects.

are required to have a confidence level greater than 0.01%. For physics analyses, the requirement is normally tighter.

4.9.1 Inner Muons Reconstruction

As seen in section 2.10, the inner muon detector consists of three scintillating hodoscopes with two planes each. The hits recorded in the six planes are used to construct a χ^2 for the hypothesis for a track being a muon as follows:

$$\chi^2 = \sum_{i=1}^{6} \sum_{j=1}^{6} C_{ij}^{-1}(t_i - X_i)(t_j - X_j) \tag{4.6}$$

where the sum ranges over the six planes, X_i is the coordinate of the hit recorded on the i^{th} plane, t_i is the coordinate of the track extrapolation to the i^{th} plane, and C_{ij}^{-1} is the inverse of the coordinate covariant matrix. The effects of multiple Coulomb scattering in the filters are included in the calculation. Fig. 4.8 shows how the inclusion of these effects is crucial in rejecting spurious tracks that by accident might match the hits better than the real muon that produced them. In the figure solid lines indicate the actual particle trajectory of a real muon (A) which leaves the hits indicated with crosses, and another particle (B) that is absorbed in the filter. Dashed lines indicate the trajectory extrapolation without including multiple Coulomb scattering effects. Due to

multiple Coulomb scattering the hits do not lie along the extrapolated trajectory of the muon. In fact in this example they provide a better match to the spurious track. When multiple Coulomb scattering effects are included the confidence level is better for the trajectory of A, as a match between the hits and the trajectory of B would require large scattering angles. In the muon algorithm the t_i coordinates are calculated with a straight line extrapolation and the multiple Coulomb scattering effects are included in the covariant matrix by evaluating, based on the track momentum, the range were hits are expected considering multiple Coulomb scattering. The errors are dominated by multiple Coulomb scattering at low momentum and by the granularity of the planes at high momentum. The most upstream hit recorded is assigned a higher weight than the other hits.

Muon candidates are required to have hits in at least four out of the six hodoscope planes. For tracks with momentum below 10 GeV/c, the requirement is only two planes because lower momentum muons can be absorbed in the filters. For a low momentum track, hits are searched over a larger area, therefore it is easier to find a good confidence level. Normally, a minimum value for the muon candidate momentum is required to separate signal from background. We investigate how likely it is that the muon candidate is uniquely responsible for the hits used for the fit. To do this, all MWPC tracks are fit to the set of hits used for the muon candidate, and the two best confidence levels from these fits are saved. This information on the isolation from other tracks can be used in physics analyses to reject background.

The efficiency of the scintillating hodoscopes has been carefully studied using the muon halo in the beam. These studies report that the efficiency of the Inner Muon arrays is greater than 99%. Golden mode D decays have been used for misidentification studies as a function of the track momentum. For momenta greater than 10 GeV/c, the proton misidentification rate is less than 0.1%, while the pion misidentification rate is about 1%. Most of the pion contamination derives from the decay $\pi^{\pm} \rightarrow \mu^{\pm}\nu$, where

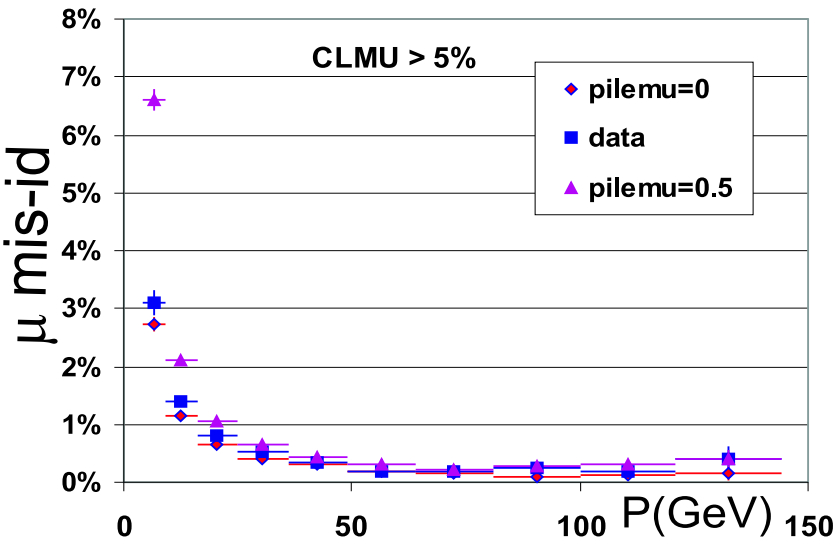

Figure 4.9: Kaon and pion misidentification rate of inner muons as a function of the track momentum. The data is compared to a zero noise Monte Carlo simulation (pilemu=0, where pilemu is the Poisson average of halo muons in each event) and a Monte Carlo simulation with much higher noise than in normal charm events (pilemu=0.5).

the muon direction is very close to the pion direction. Fig. 4.9 shows the kaon and pion misidentification rate of inner muons as a function of the track momentum. The data results are compared to two simulations, a zero noise Monte Carlo and one with a muon halo rate much higher than it is present in typical charm data.

4.9.2 Outer Muons Reconstruction

The Outer Muon system muons are reconstructed from fitting MWPC tracks to hits collected in the detector. In this case the fit is complicated by the magnetic field in the filter M2 that deflects the charged tracks. This deflection is accounted for by tracing the muons through the magnetic field. Multiple Coulomb scattering in the M2 iron and in the Outer Electromagnetic calorimeters is included in the tracing of the track. Particles that enter the Outer Muon system have lower momenta and therefore a more detailed treatment of energy loss is performed. The efficiency is good for muons above 4 GeV/c. Below 4 GeV/c muons are normally absorbed in the filters and do not contribute to the sample.

Chapter 5

Event Selection

As seen before, $c\overline{c}$ pairs are produced from the interaction of a photon beam on a BeO target. The two quarks hadronize into charmed mesons and baryons which can be reconstructed through the decay into long lived particles. In this chapter we describe the selection of the $D^0 \to \overline{K}^0\pi^-\mu^+\nu$ and $D^0 \to \overline{K}^0\pi^-\pi^+$ decays. The D^0 meson is reconstructed from the decay $D^{*+} \to D^0\pi^+$. The $\overline{K}^0$ is reconstructed as a K^0_S from the decay $K^0_S \to \pi^+\pi^-$.

The analysis uses data from one of the Sub–streams of Skim 2; the 212 FSK tapes that contain events with at least one reconstructed $K^0_S \to \pi^+\pi^-$ candidate. We reduced the 1 TB of data on the FSK tapes to approximately 70 GB in two steps that will be called Selection–1 and Selection–2. After describing the Selection–1 and Selection–2 processes, we will explain the event selection for the specific decays $D^0 \to \overline{K}^0\pi^-\mu^+\nu$ (signal mode) and $D^0 \to \overline{K}^0\pi^-\pi^+$ (normalization mode).

Since a Monte Carlo simulation is used to compute the selection cuts efficiency, a systematic bias due to poor simulation of the detector performance could be introduced. We choose to normalize to a mode with a very similar topology, and we apply the same selection cuts (whenever possible) as the semileptonic mode, in order to minimize such possible bias. The cuts are optimized for the semileptonic mode.

5.1 Selection–1

The Selection–1 process reduced the data to almost 300 GB. This process selects the decays $D^0 \to K_s\pi^-\ell^+\nu_\ell$, $D^0 \to K_s\pi^-\pi^+$, and $D^+ \to K_s\pi^-\pi^+\pi^+$ (for other physics analyses that are being performed in FOCUS). An event is required to pass the hadronic trigger and to have at least four tracks reconstructed in the SSD system. As seen in section 2.11, the hadronic trigger requires signals of TR1 and TR2 to be in coincidence, that the energy deposited in the hadron calorimeter is above a certain threshold, and that at least two charged particles have been detected in the $H \times V$ array or that at least one charged particle has been detected in the $H \times V$ array and one charged particle has been detected in the OH array.

Only events where the candidate K^0_S is an M1 or SSD type Vee are retained. For the remainder of the thesis we will refer to M1 stub–stub, M1 stub–track, M1 track-track and SSD Vees as types 1, 4, 5, and 9, respectively. The invariant mass $M(\pi^+\pi^-)$ is required to be within three mass errors σ_m of the nominal K^0_Smass.

Leptons and pions from the D meson are selected by requiring they are linked and have a confidence level less than 3% for being produced at zero angle with respect to the beam direction. This requirement eliminates most of the e^+e^- pair contamination from the incident photon beam. All the pions have a loose identification requirement of picon > -6, where picon $= \min(Wobs) - Wobs(\pi)$.

For the semileptonic mode, both muon and electron candidates are kept in the two categories of outer and inner tracks [1] . Inner electrons must have P>10 GeV/c, have hits reconstructed in all 5 MWPC stations, and have the quality parameter IEID between 10 and 13. This quality parameter combines the information from the Inner Electromagnetic calorimeter with the information from the Čerenkov counters. An IEID

[1] We remind the reader that inner (outer) type tracks are tracks that enter (do not enter) the acceptance of the second magnet M2. Inner type particles are produced at smaller angles with respect to the beam direction compared to outer type, and have larger momentum.

greater than or equal to 10 corresponds to tracks with E/p in the window 0.8 – 1.25. An IEID between 11 and 13 means that the Čerenkov identification algorithm returns a good confidence level for the electron hypothesis. Outer electrons must have P>5 GeV/c, have hits reconstructed in the first 3 MWPC stations, have 0.8 < E/P< 1.25, and have the quality parameter OESCDST > 0.5. This parameter is used to discriminate between pions and electrons. At this stage muon candidates are simply required to have C.L.(μ) >0.1% as calculated with either the inner or the outer muon system.

A decay vertex for the D is formed from the pion tracks (or the pion and the lepton track in the semileptonic case) that pass the identification cuts. The K^0_S object is used to form the vertex only if it is type 9, since for the other cases its direction is known with relatively low precision. The track combination is kept if the vertex C.L. is greater than 1% and if the z coordinate lies in the target region (-10 cm< z_{VTX} < 4 cm). For type 9 K^0_S we require ℓ/σ_ℓ >5 (where ℓ is the distance between the charm and the K^0_S decay vertices, and σ_ℓ is the error on that distance).

For the hadronic modes we require the invariant mass of the K^0_S and the pions from the D to be in the window 1.7–2.1 GeV/c^2, and that the total momentum of the reconstructed particles (which corresponds to the total momentum of the D) be greater than 35 GeV/c. For the mode $D^0 \to \overline{K}^0\pi^-\pi^+$ we require opposite charges for the candidate pions. For semileptonic modes the invariant mass M($K_s\pi^-\ell$) is required to be smaller than 2.1 GeV/c^2. Table 5.1 summarizes the Selection–1 requirements.

5.2 Selection–2

The data were reduced from 300 GB to about 70 GB with the Selection–2 process. This is a selection of the semileptonic decay and the normalization mode: $D^0 \to \overline{K}^0\pi^-\ell^+\nu$ and $D^0 \to \overline{K}^0\pi^-\pi^+$. In addition to the Selection–1 cuts for these two modes, a preliminary reconstruction of the $D^{*+} \to D^0\pi^+$ is performed.

An event is retained if there is a pion candidate that gives a mass difference be-

K_S^0	TYPE 1, 4, 5, 9 $(M(\pi^-\pi^+) - 0.4977)/\sigma_{M(\pi^-\pi^+)} < 3$
Common Cuts for π, ℓ:	Linked Tracks Non–zero Angle w.r.t. Beam Axis
All π's	picon>-6
Inner Electron Outer Electron Inner Muon Outer Muon	p >10GeV/c, 5 MWPC Stations 10 <IEID< 13 p >5GeV/c, 3 MWPC Stations 0.8 <E/p< 1.25, OESCDST$\geq$0.5 INNER MUON CL>0.1% OUTER MUON CL>0.1%
D decay Vertex	DCL>1% -10 cm< z_{VTX} < 4 cm K_S^0 Used for Vertexing Only if Type 9
Invariant Masses	1.7 GeV/c^2< $M(K_s\pi^-\pi^+) < 2.1$ GeV/c^2 1.7 GeV/c^2< $M(K_s\pi^-\pi^+\pi^+) < 2.1$ GeV/c^2 $M(K_s\pi^-\mu^+) < 2.1$ GeV/c^2
D Momentum	$p(K_s\pi^-\pi^+)$, $p(K_s\pi^-\pi^+\pi^+) > 35$ GeV/c
$K_s\pi^-\pi^+$ mode	Opposite Charge π^- and π^+

Table 5.1: Summary of the requirements for Selection–1.

tween the D^* and the D in the broad region where the signal events are expected to pile up. We call this pion candidate "π^{soft}", due to its rather low average momentum (about 8 GeV/c). For the hadronic mode we require $\Delta M = M(K_s\pi^-\pi^+\pi^{soft}) - M(K_s\pi^-\pi^+) <$ 200 MeV/c^2 and for the semileptonic mode we require $\Delta M = M(K_s\pi^-\mu^+\pi^{soft}) - M(K_s\pi^-\mu^+) <$ 300 MeV/c^2. At this stage the neutrino momentum is undetermined, so the distribution is broader for the semileptonic mode than for the hadronic mode. In the rest of the thesis we will refer to the mass difference as ΔM for both the hadronic and semileptonic modes. The π^{soft} candidate must pass the same cuts as the π^- from the D^0 : the track must be linked, it must have picon > -6, and the hypothesis that the angle with respect to the beam axis is not zero must have C.L.>3%. No requirement is made on the sign of the charge. We require that the lepton and the pions (π^- from the D^0 and π^{soft}) not share the track segment in either the SSD or in the MWPC systems.

5.3 Selection Cuts for $D^0 \to \overline{K}^0\pi^-\mu^+\nu$ and $D^0 \to \overline{K}^0\pi^-\pi^+$

After the Selection–1 and Selection–2 processes are finished, tighter requirements are applied to further select signal events and reject backgrounds.

In addition to the reconstructed mass being within three standard deviations from the nominal mass, we identify the K^0_S with tighter requirements that depend on the Vee type. For type 1 K^0_S we require the uncertainty on the z coordinate of the decay vertex to be smaller than 10 cm. Both pions must be reconstructed in the first 3 MWPC stations, they each must have momentum greater than 3 GeV/c, and their slopes along the x direction must be greater than 0.002 (to reject events where one of the pions is from an e^+e^- pair). The K^0_S momentum must be greater than 7 GeV/c. For type 4 K^0_S we require that the distance of closest approach between the pions is less than 0.6 cm. The linked track from type 5 K^0_S must have the slope along the x direction greater than 0.002. For type 9 K^0_S we require that the decay vertex is outside the material in the target region and it must have a fit confidence level greater than

5%. Fig. 5.1 shows the di–pion mass distributions for the K_S^0 candidates for the final sample used for this thesis. The K_S^0 types 4 and 5 constitute the bulk of the data.

The selection of the π^- candidate for the semileptonic mode starts from the linked tracks that do not have double links in the MWPC system, as is normally the case for e^+e^- pairs where the two tracks get separated in the first magnet. To reject this background, we also require that the probability for the track to be produced at zero degrees with respect to the beam is less than 3%. Čerenkov identification is performed by requiring picon > -6, and W(K)-W(π)>1. The track momentum must be greater than 10 GeV/c. For the hadronic mode we identify the pion that has opposite charge with respect to π^{soft} and apply the same requirements as for the π^- in the semileptonic mode.

The muon candidate is selected from the linked tracks that have a C.L. greater than 1% for the fit to the hits in either the inner or the outer muon system. The track must not be double linked, and it must be produced at non–zero angle. The track must have been reconstructed in all 5 MWPC stations for inner type muons and in the first 3 MWPC stations for outer type muons. Its momentum must be greater than 10 GeV/c. This cut significantly reduces the contribution from the outer type muons. We intentionally do not adopt looser cuts for this category, as studies showed that they are more contaminated by backgrounds. For inner type muons we require that the hypothesis that the muon trajectory is consistent through the two analysis magnets has a confidence level greater than 1%. This requirement is designed to reject background from the decay $\pi^+ \to \mu^+\nu$. The hits must have been found in at least 5 out of 6 planes in the inner muon arrays. In the momentum range 13.2 GeV/c $< P(\mu) <$ 17.4 GeV/c, where the muon Čerenkov pattern is more similar to the electron than to the pion, we require that the muon track satisfies $W(\pi) - W(e) > 0$. For outer type muons we require that at least 200 cm of material has been passed through (which rejects most of the particles that are more likely to be absorbed) and the track must have been

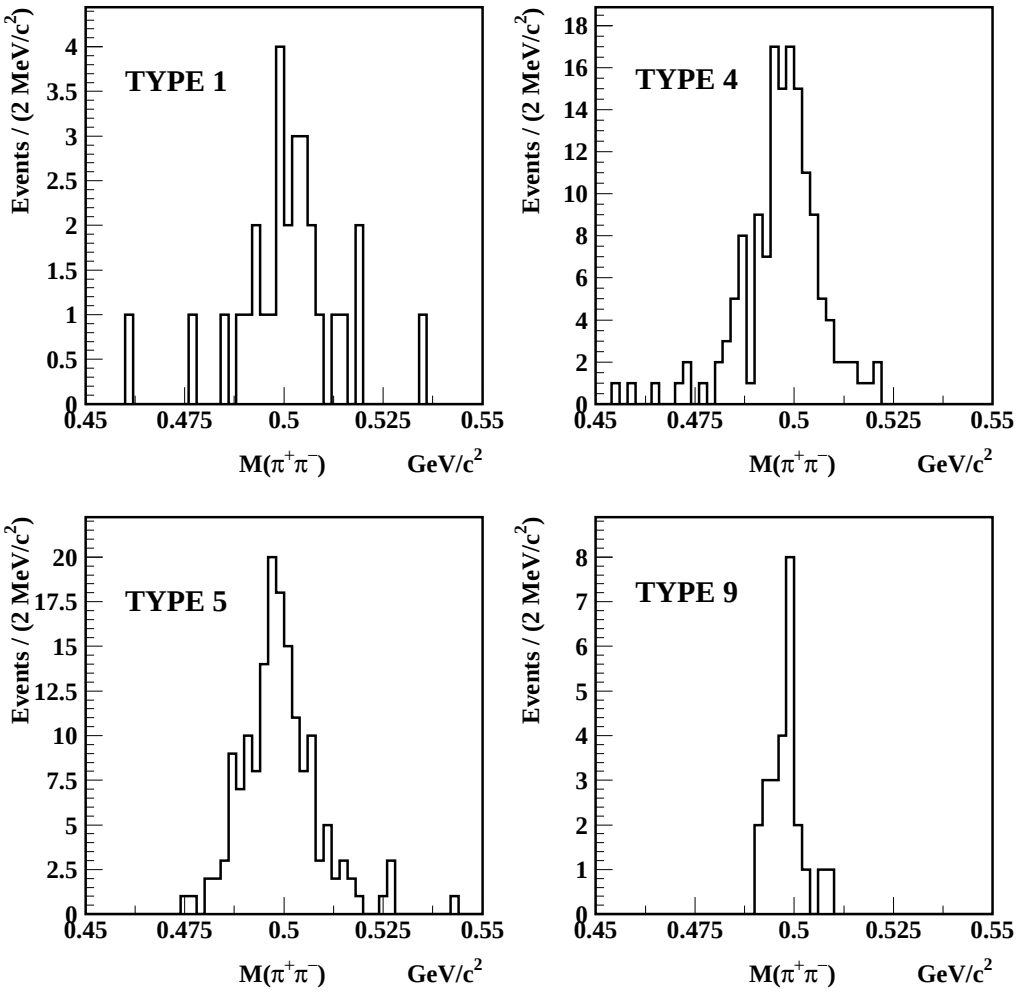

Figure 5.1: M($\pi^-\pi^+$) distributions for K^0_S candidates for the Vee types used in this thesis. Type 1, 4, 5, and 9 correspond to M1 stub–stub, M1 stub–track, M1 track–track, and SSD type, respectively.

reconstructed in the first 3 MWPC stations.

The muon and pion candidates (the two pion candidates) for the semileptonic (hadronic) mode are used to form the charm decay vertex. The K^0_S is included in the vertex finding only if it is type 9, as its direction is known with low precision for the other categories. The vertex is required to have good confidence level (C.L.>5%) and, in order to reject hadronic reinteraction events, it must lie one sigma outside of the target material. Background events from higher multiplicity charm decays are discarded by requiring that the maximum confidence level for other tracks to come from the secondary vertex (ISO2) is less than 0.1% (not including tracks associated with the primary vertex).

The charm production vertex (or primary vertex) of the event is reconstructed with DVFREE (see Sect. 4.2). Candidates are discarded if the confidence level is less than 1%. If more than one vertex is found, the vertex with highest track multiplicity is selected and, in the case of a tie, the one with the largest detachment from the secondary vertex is kept. Vertex detachment is perhaps the most powerful tool to discard non–charm hadronic interaction events. The detachment is given by the distance between the two vertices over its error (ℓ/σ_ℓ), as schematically shown in Fig. 5.2. In a fixed target experiment, particles are produced with a large longitudinal momentum; for this reason the Lorentz boost between the particle rest frame and the laboratory system is quite large. Charm particles travel distances long enough to provide a fairly good separation between primary and secondary vertices. On the contrary, non–charm backgrounds decay promptly or much further downstream. For this reason the charm decay can be identified by requiring that the primary and the secondary vertices are reconstructed with a significantly large detachment. For both the semileptonic and the hadronic modes we require $\ell/\sigma_\ell > 5$.

Once the D^0 decay is reconstructed, we search for a pion (π^{soft}) and reconstruct the decay $D^* \rightarrow D^0\pi^+$. The pion must be one of the linked tracks coming from the

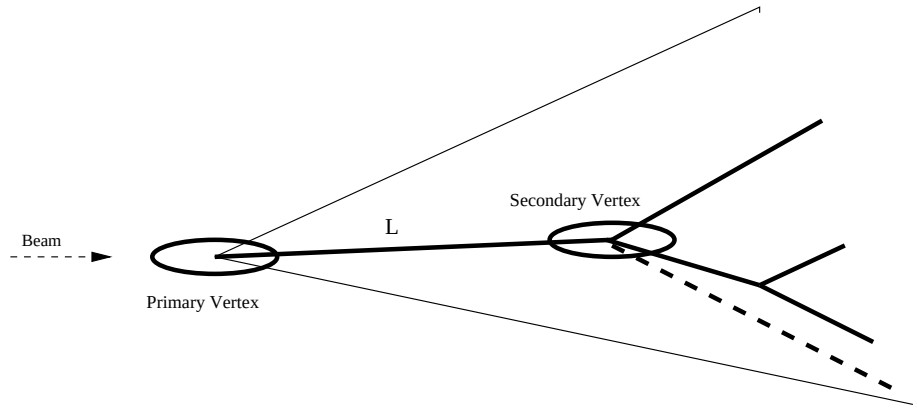

Figure 5.2: A schematic for a charm particle production and decay is shown.

primary vertex. It must not be double linked and it must be produced at a non–zero angle with respect to the beam direction. The track is identified as a pion by requiring picon>-6 and its momentum must be greater than 2 GeV/c. For the semileptonic mode the sign of charge of π^{soft} is required to be the same as that of the muon.

For the semileptonic mode we require that the $\overline{K}^0\pi^-$ invariant mass is in the window of one natural width ($\Gamma = 50$ MeV/c^2) around the nominal $K^*(892)^-$ mass, see Fig. 5.3. The $K^*(892)^-$ natural width is much larger than the experimental resolution on the reconstructed $K^0_S\pi^-$ mass (about 5 MeV/c^2). For this mode the total "visible" mass $M(K^0_S\pi^-\mu^+)$ is required to be less than 1.8 GeV/c. Due to the missing neutrino energy, $M(K^0_S\pi^-\mu^+)$ has to be less than the nominal D^0 mass. With this cut we reject a significant part of the combinatoric background and most of the contamination from $D^0 \rightarrow \overline{K}^0\pi^-\pi^+$, where a pion is misidentified as a muon. These background events can pass the mass cut if one of the pions decays. We have evaluated with Monte Carlo studies that this contamination is negligible. Fig. 5.4 shows the D^0 reconstructed mass distribution for the hadronic mode and the "visible" D^0 reconstructed mass for the semileptonic mode (M($K_s\pi^-\mu^+$)) for our final sample.

Although the neutrino is undetected, different methods can be used to find its momentum, which we must use to compute q^2 and ΔM. To compute the q^2 we

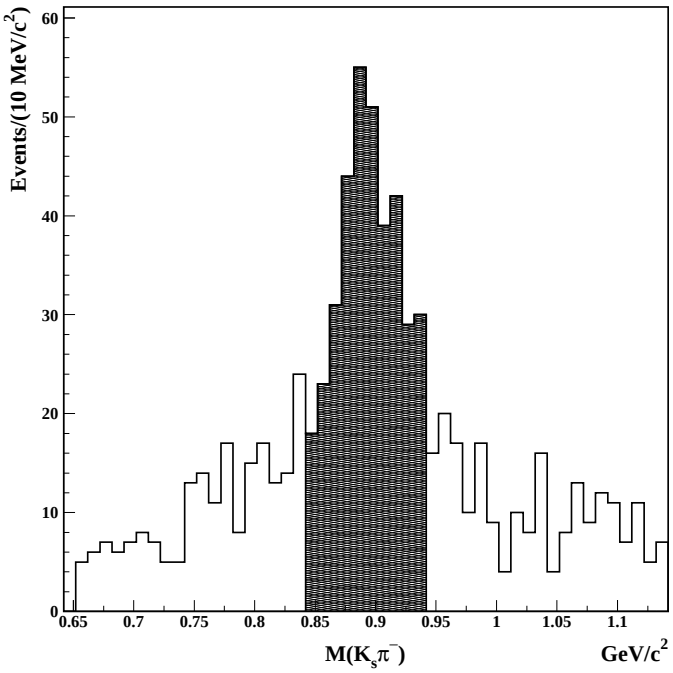

Figure 5.3: $\overline{K}^0\pi^-$ invariant mass. We select events within 50 MeV of the nominal $K^*(892)^-$ mass (shaded area).

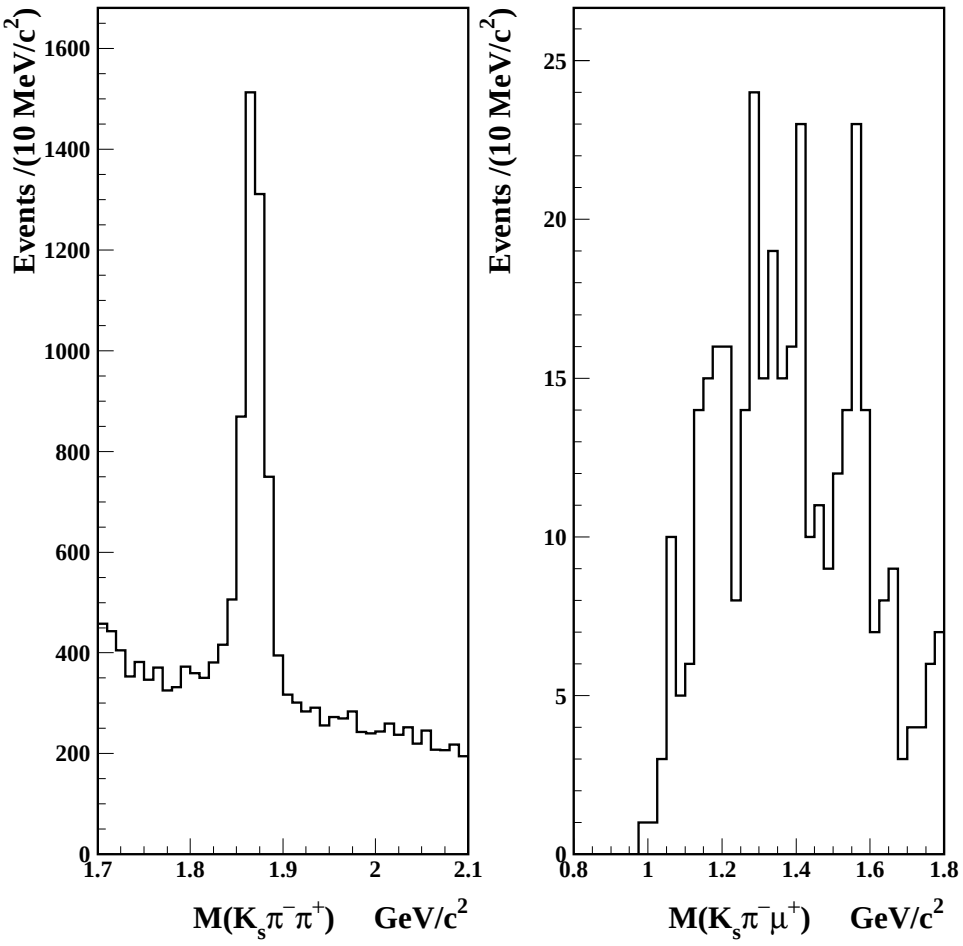

Figure 5.4: Left: D^0 reconstructed mass distribution for the hadronic mode. Right: reconstructed mass distribution M($K_s\pi^-\mu^+$) for the semileptonic mode.

use a "D^* cone" algorithm. By imposing energy and momentum conservation in the $K^*(892)^-$ rest frame and by constraining the D and the D^* to their nominal masses, we fix the magnitude of $p(D^0)$ (which in this frame is equal to $p(\nu)$), but its direction lies on a cone. The direction is chosen by selecting the solution that gives the best χ^2 when compared with the D^0 direction as given by the line connecting the two vertices. Additional details on the method can be found in Appendix A. To compute the mass difference, we determine the neutrino momentum using the "neutrino closure" algorithm. This method is based on energy and momentum conservation for the decay $D^0 \to \overline{K}^0\pi^-\mu^+\nu$ and uses the nominal mass of the D^0 meson. The algorithm allows for us to determine the neutrino momentum up to a two fold ambiguity, which we resolve by choosing the solution with lowest ΔM. Monte Carlo studies show that this choice is most often the correct solution. The method is fully described in Appendix B.

Fig. 5.5 and Fig. 5.6 show the mass difference distributions for the semileptonic and the hadronic modes, for different values of the detachment cut ($\ell/\sigma_\ell > 4$,....,12).

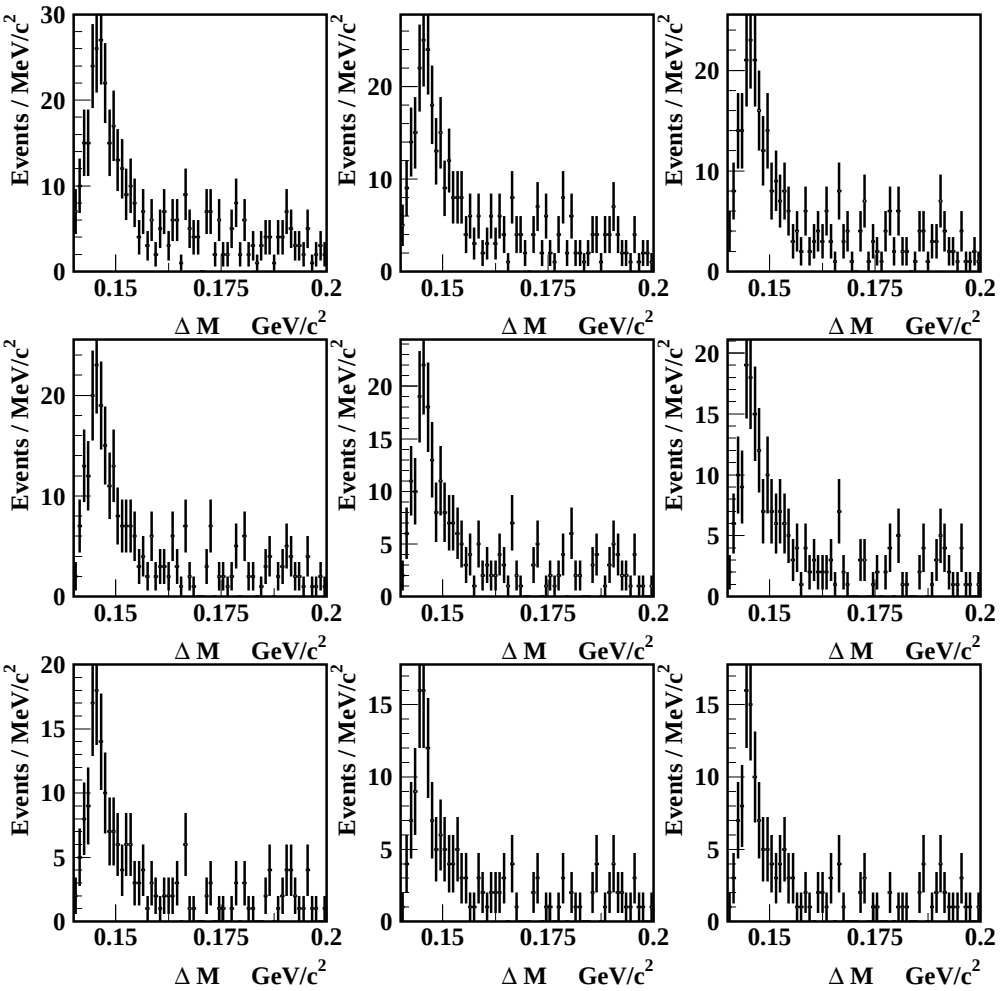

Figure 5.5: Distributions of the mass difference for the semileptonic mode, $\Delta M = M(K_s\pi^-\mu^+\nu\ \pi^{soft}) - M(K_s\pi^-\mu^+\nu)$ for different values of the ℓ/σ_ℓ cut. From left to right, top to bottom: $\ell/\sigma_\ell > 4$, 5, ...,12.

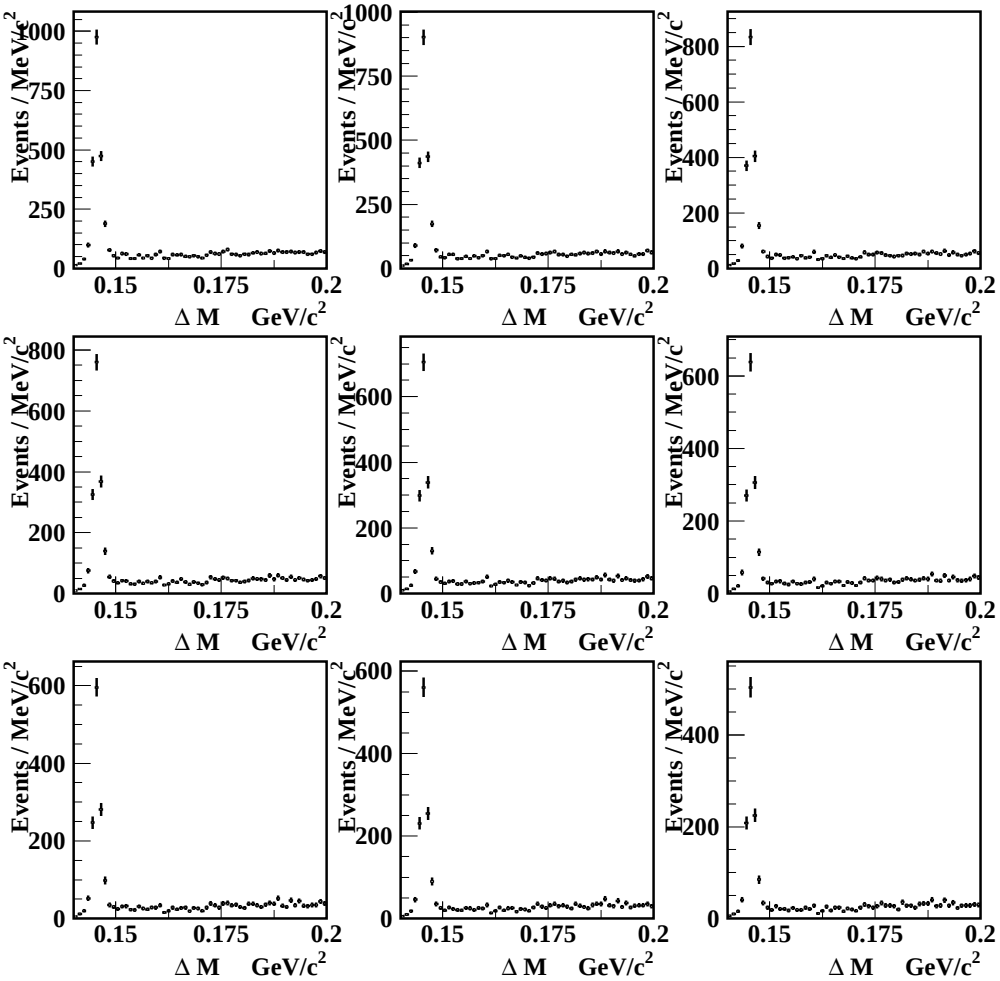

Figure 5.6: Distributions of the mass difference for the hadronic mode, $\Delta M = M(K_s\pi^-\pi^+\pi^{soft}) - M(K_s\pi^-\pi^+)$, for different values of the ℓ/σ_ℓ cut. From left to right, top to bottom: $\ell/\sigma_\ell > 4$, 5, ...,12.

Chapter 6

Fit to the Form Factor Ratios and to the S-wave Amplitude

In this chapter we motivate the use of a model including the $\overline{K}^0\pi^-$ S-wave component, describe the fitting procedure for the form factor ratios and for the amplitude of the S-wave, present the fit results, and describe the estimate of the systematic uncertainty.

6.1 The $\overline{K}^0\pi^-$ S-wave

The study of the decay $D^0 \to \overline{K}^0\pi^-\mu^+\nu$ presented in this thesis is based on a model that includes an S-wave component that interferes with the dominant $K^*(892)^-$. As described in Section 1.4, the S-wave is represented by an amplitude and a constant phase, Ae^{δ}. The new terms introduced in the decay amplitude due to the S-wave contributions are a term proportional to A^2 and an interference term between the S-wave and the $K^*(892)^-$. Since the A^2 term is small, the presence of the S-wave contribution can be inferred from the interference term. This term is (from the square of the first term in equation 1.15):

$$\begin{aligned}\text{Interference} = \; & 8\ \cos\theta_V \sin^2\theta_\ell A\ \mathcal{R}e(e^{-i\delta}B_{K^{*-}})H_0^2 \\ & - 4(1+\cos\theta_\ell)\sin\theta_\ell \sin\theta_V A\ \mathcal{R}e(e^{i(\chi-\delta)}B_{K^{*-}})H_+H_0 \\ & + 4(1-\cos\theta_\ell)\sin\theta_\ell \sin\theta_V A\ \mathcal{R}e(e^{-i(\chi+\delta)}B_{K^{*-}})H_-H_0\end{aligned}$$

The interference term introduces a component proportional to $\cos\theta_V$ in the decay

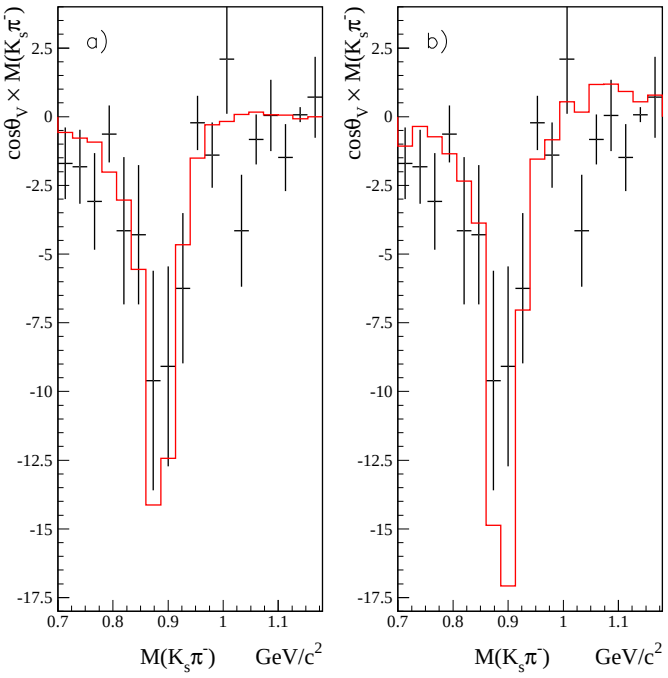

Figure 6.1: Distribution of $M(K_s\pi^-)$ weighted by $\cos\theta_V$ versus $M(K_s\pi^-)$ after wrong sign subtraction. Points with error bars are data, the histogram is Monte Carlo. The distributions are normalized to data. a): MC generated with S-wave, b): MC generated without S-wave. A slightly better match to data is achieved with the S-wave included in the Monte Carlo.

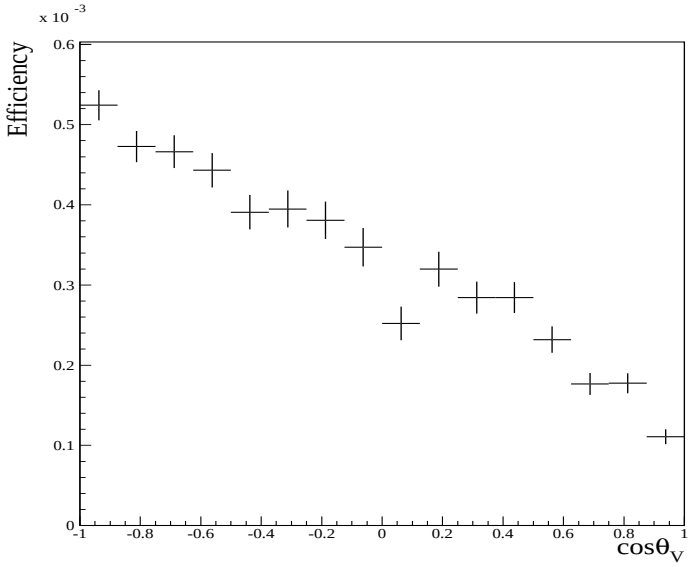

Figure 6.2: MC reconstruction efficiency versus $\cos\theta_V$.

amplitude, which is otherwise symmetric with respect to $\cos\theta_V$.

If the efficiency versus $\cos\theta_V$ is flat, the distribution of $M(K_s\pi^-)$ weighted by $\cos\theta_V$ is null if there is no S-wave, while it has an excess in the negative values if there is the S-wave. Figure 6.1 shows a comparison of data with two Monte Carlo distributions, one generated with S-wave and one without. In order to reduce the amount of background for this comparison, we subtract the same distribution for the "wrong sign" events. These events are given by combinations where the muon and π^{soft} have the opposite sign, and is a good rapresentation of the combinatoric background. We observe a large discrepancy from zero with and without the S-wave in the MC. This is due to the fact that the efficiency is not flat versus $\cos\theta_V$, but has a linear dependence, with main loss of events at positive $\cos\theta_V$ values (see Fig 6.2). Data agrees well with both simulations, but the MC with S-wave included is a better description, so we use the MC that includes the S-wave as a default simulation, and we use the MC without S-wave as a check on the bias due to this assumption (as will be described later).

6.2 The Fitting Technique

Using a binned maximum likelihood technique, we fit simultaneously the three dimensional distribution $\cos\theta_V \times \cos\theta_\ell \times q^2$ and the ΔM distribution. The fit to ΔM allows us to assess the background level, since for this variable the signal and the background distributions have very different shapes. For the ΔM component we use 60 bins in the region 0.14–0.20 GeV/c^2. For the $\cos\theta_V \times \cos\theta_\ell \times q^2$ distribution we select events with $\Delta M <$ 0.15 GeV/c^2, and we divide the phase space into four equally spaced bins for each of the two angular variables and two equally spaced bins for q^2. We construct the likelihood $\mathcal{L}$ as:

$$\mathcal{L} = \prod_{ijk} \frac{n_{ijk}^{s_{ijk}} e^{-n_{ijk}}}{s_{ijk}!} \times \prod_{l} \frac{N_l^{S_l} e^{-N_l}}{S_l!}$$

where s_{ijk} (n_{ijk}) is the number of observed (expected) events in the ijk^{th} bin of the three dimensional distribution, and S_l (N_l) is the number of observed (expected) events in the ΔM distribution. The number of expected events is given by signal and background contributions.

Non-charm backgrounds are effectively removed by the ℓ/σ_ℓ requirement, by discarding events where the reconstructed decay vertex of the D^0 lies within one standard deviation from the target, and by the muon requirement. Contamination from charm decays is estimated with a Monte Carlo (that will be called MC_{BKG}) which simulates all known charm decays other than our signal mode. The background shape for both distributions (ΔM and $\cos\theta_V \times \cos\theta_\ell \times q^2$) is taken from the distribution of the reconstructed events in MC_{BKG}, and their amplitude is free to float. Since we require ΔM<0.15 GeV/c^2 for the events used to plot $\cos\theta_V \times \cos\theta_\ell \times q^2$, we require that the signal (background) yield in the $\cos\theta_V \times \cos\theta_\ell \times q^2$ distribution is equal to the area of the signal (background) shape in the ΔM distribution below 0.15 GeV/c^2.

For the ΔM distribution, the shape obtained from Monte Carlo generated $D^0 \to \overline{K}^0\pi^-\mu^+\nu$ events is used as the expected signal shape (after all selection cuts are applied). For the $\cos\theta_V \times \cos\theta_\ell \times q^2$ distribution, the signal contribution to n_{ijk} is computed as the number of events generated in the bin ijk corrected by the efficiency in that bin. The generated number of events depends on the form factor ratios and on the S-wave parameters. We compute this number using a weighting of the MC generated events based on [38]. For each Monte Carlo event generated in the bin ijk, we fill that bin with a weight given by the ratio of the decay amplitude in Eq. 1.15 over the decay amplitude evaluated for the input Monte Carlo values [1] . For instance, for the form factor ratios fit, where the S-wave parameters are fixed, the weight is given by:

$$\text{Weight} = \frac{\Gamma(r_v', r_2')}{\Gamma(r_v^\circ, r_2^\circ)} \tag{6.1}$$

[1] The FOCUS Monte Carlo generation uses the D^+ form factor ratios and the S-wave parameters measured in [20] for any $D \to V\ell\nu_\ell$ decay: $r_v = 1.504$, $r_2 = 0.875$, $A = 0.330$, and $\delta = 0.68$.

where r'_v and r'_2 are the fit parameters and r°_v and r°_2 are the values used for generating the MC events. This way the number of generated events in the bin ijk is:

$$\mathrm{No(Generated)}_{ijk} = \sum_{e_{ijk}} \frac{\Gamma^e(r'_v, r'_2)}{\Gamma^e(r^\circ_v, r^\circ_2)}$$

where the sum is over the generated events in the bin ijk of the $\cos\theta_V \times \cos\theta_\ell \times q^2$ distribution. Finally, the number of expected signal events in such bin is:

$$\mathrm{Sig}_{ijk} = \epsilon_{ijk} \times \sum_{e_{ijk}} \frac{\Gamma^e(r'_v, r'_2)}{\Gamma^e(r^\circ_v, r^\circ_2)}$$

where ϵ_{ijk} is the efficiency of the bin. This efficiency is determined by dividing the Monte Carlo reconstructed events in each of the $\cos\theta_V \times \cos\theta_\ell \times q^2$ distribution bins by the number of generated events in that bin. Fig 6.3 and 6.4 show the efficiency in each bin of the three variables.

The choice of the binning for the $\cos\theta_V \times \cos\theta_\ell \times q^2$ distribution ($4 \times 4 \times 2$) gives information on the angular distributions of the W and the $\overline{K}^0\pi^-$ decays, for two regions of q^2. At low q^2 the angular dependence is more dramatic, while a more isotropic behavior is expected for high q^2 values, where the helicity amplitudes contribute with similar strength. Fig. 6.5 shows the MC distributions of the two angular variables for high and low q^2 . The events are plotted before any acceptance or reconstruction effect, to show differences only due to the dynamics of the process. Fig. 6.6 shows the same distributions for data reconstructed events compared to MC reconstructed events. The agreement is good for all four plots.

The results of the simultaneous fit to ΔM and $\cos\theta_V \times \cos\theta_\ell \times q^2$ are illustrated in Fig. 6.7. The χ^2 per degree of freedom in Fig. 6.7b is 40.0/30, which corresponds to a confidence level of 22%. We measure:

$$r_v = 1.71 \pm 0.68 \tag{6.2}$$

$$r_2 = 0.91 \pm 0.37 \tag{6.3}$$

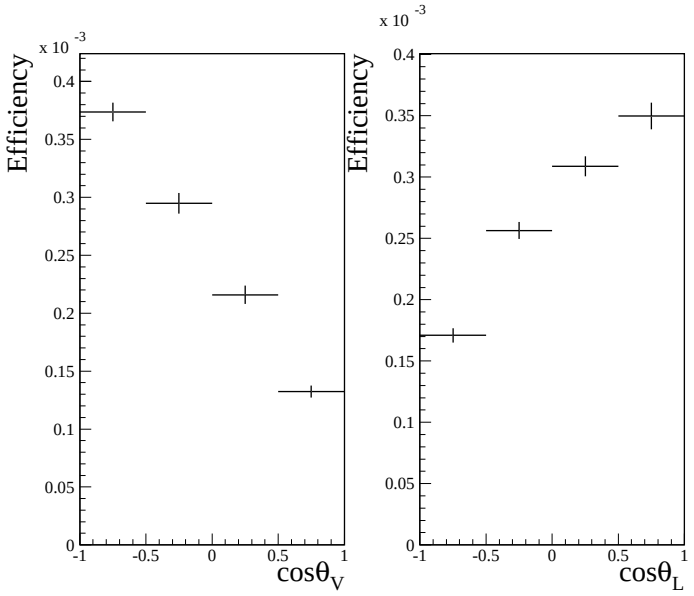

Figure 6.3: Efficiency versus the four $\cos\theta_V$ and the four $\cos\theta_\ell$ bins.

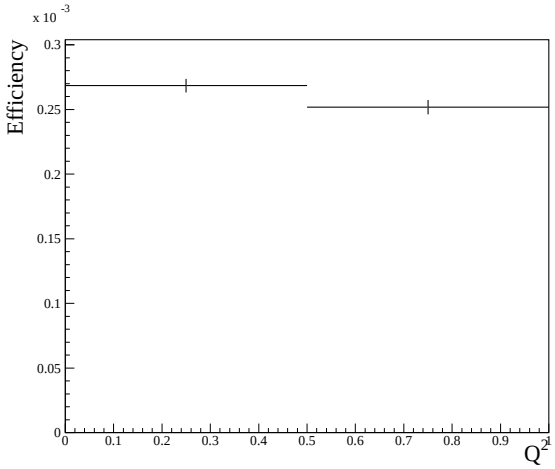

Figure 6.4: Efficiency versus the 2 q^2 bins.

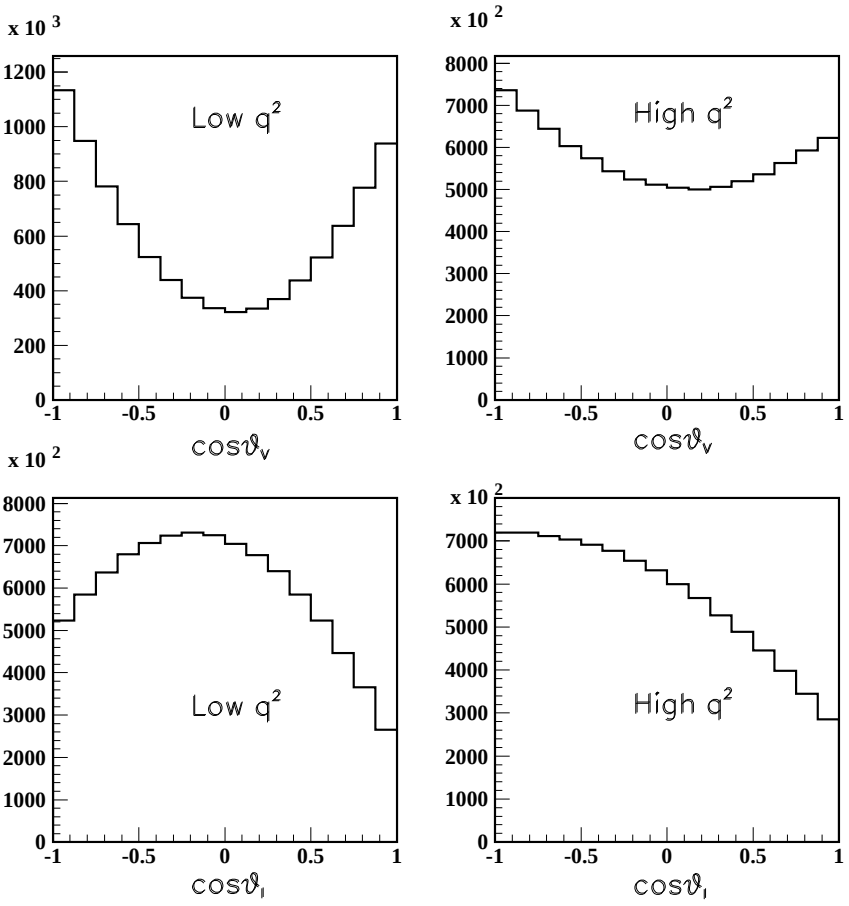

Figure 6.5: Monte Carlo generated angular distributions before acceptance, resolution and efficiency effects, for high and low q^2 values.

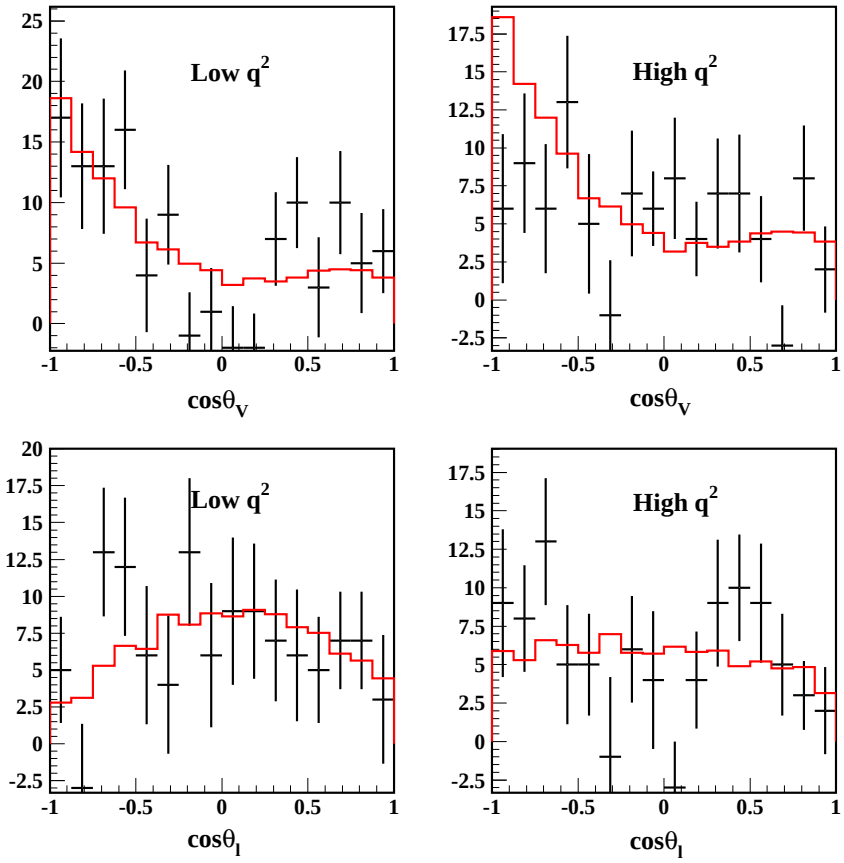

Figure 6.6: Comparison of angular distributions at high and low q^2 between data (black points with error bars) and MC (red histogram) scaled to data events. The distributions are wrong sign subtracted.

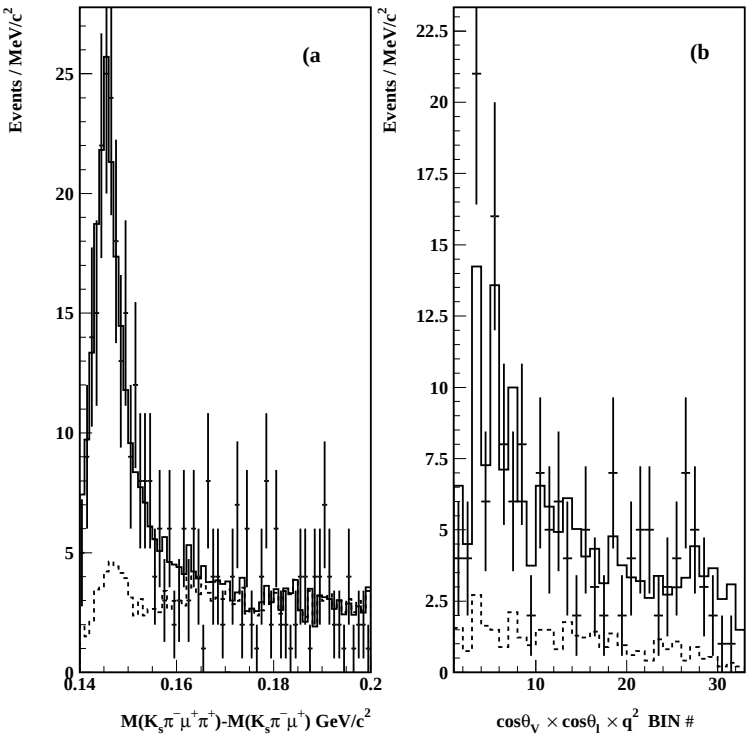

Figure 6.7: Results from the simultaneous fit to ΔM (a) and $\cos\theta_V \times \cos\theta_\ell \times q^2$ (b). Points with error bars are data, histogram is the fit, dashed line is the background component.

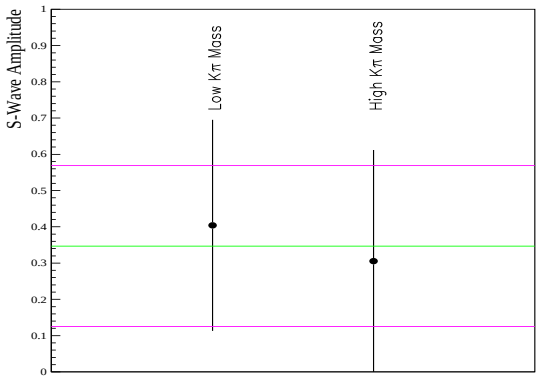

Figure 6.8: Amplitude fit results for $M(K\pi) < 0.892$ GeV/c (first point) and $M(K\pi) > 0.892$GeV/c^2 (second point). The results are compared to the value fit on the whole sample (horizontal band).

where the errors are statistical.

After fitting for the form factor ratios, we fix the values to the fit results in Eq. 6.2 and 6.3 and fit for the S-wave amplitude. For this fit we still fix the phase of the S-wave to the FOCUS measurement for the D^+ ($\delta = 0.68$ rad) as we have seen a lack of sensitivity to this parameter in fits where its value is let free to float. We measure the S-wave amplitude A to be:

$$A = 0.35 \pm 0.22$$

where the error is statistical.

In the D^+ form factors and S-wave analysis, it has been determined that in the low $M(K\pi)$ data ($M(K\pi) < 0.892$ GeV/c^2) the effect of the S-wave was more evident. We have split the data accordingly into low and high $M(K\pi)$, but, probably due to the low statistics and the large variation in the efficiency versus $\cos\theta_V$ and $\cos\theta_\ell$, we do not see such striking difference; see Fig. 6.8.

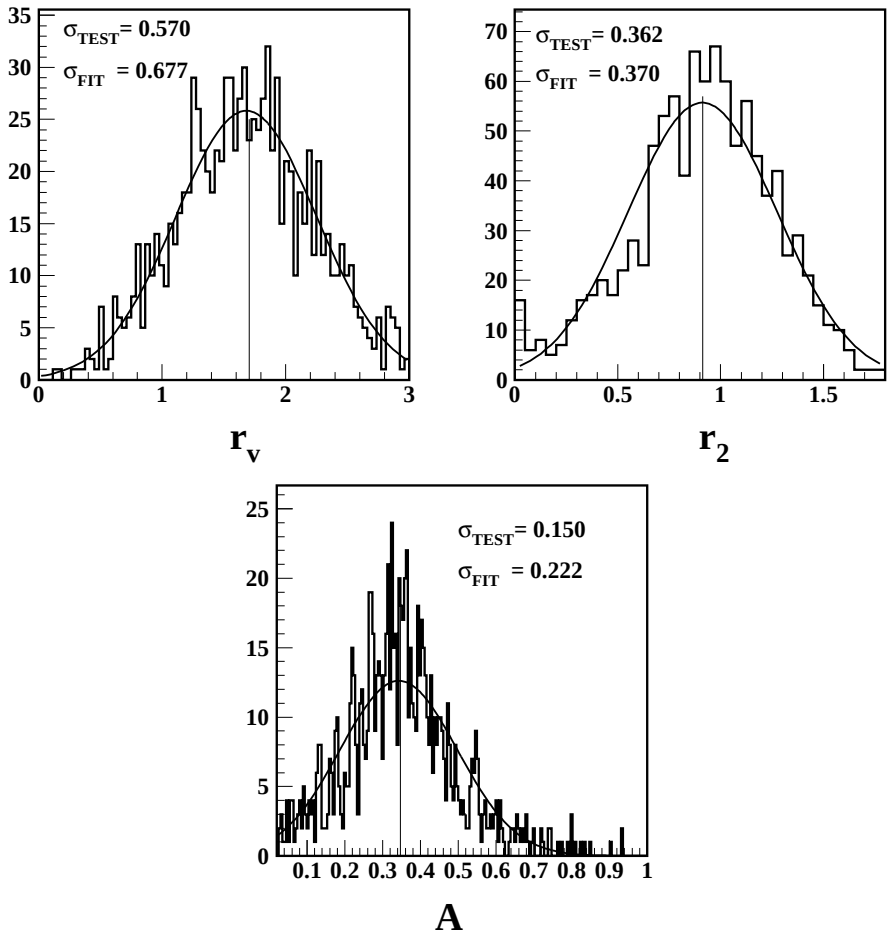

Figure 6.9: Mini MC test on the fit procedure. a): r_v, b): r_2, c): A. For each plot the vertical line shows the central value of the parameter obtained with the fit on the original real data sample. In all cases this value is in good agreement with the mean of the Gaussian. We find that our errors are not underestimated, since the error from the standard fit (σ_{FIT}), is never larger than the width obtained from the Gaussian fit to the 1000 fit results (σ_{TEST}).

6.3 Toy Monte Carlo Study

To check the accuracy of the method and the correct estimate of the errors, a "toy Monte Carlo" test was performed. The fit method is tested on 1000 samples each statistically equivalent to the data. The samples are obtained by Poisson-fluctuating 1000 times the four dimensional distribution of $\Delta M \times \cos\theta_V \times \cos\theta_\ell \times q^2$. The two projections on ΔM and $\cos\theta_V \times \cos\theta_\ell \times q^2$ for each sample were fit simultaneously with our method. If the fit technique works correctly, the distribution of the 1000 fits for a given parameter should distribute as a Gaussian with average and width close to the value and error that the fit reported on the actual data sample for such parameter. Fig. 6.9 shows the distribution of the 1000 fits results for for r_v , r_2, and A. The spread due to statistical fluctuations is determined by a Gaussian fit for each distribution. In all cases we find that the error reported by our measurement is not underestimated, for r_2 and$A$ it might actually be overestimated. The mean of the Gaussian distribution is very close to the central value reported by the fit for each parameter. We therefore conclude that the fitting method is not affected by a systematic bias.

6.4 Systematic Uncertainty Evaluation

We carefully considered and evaluated many possible sources of systematic uncertainty in our results. A possible poor MC simulation of the detector performance and of the event reconstruction and selection efficiency might introduce a bias in estimating the number of expected events in the likelihood construction. Also, the particular fitting choices (e.g. the binning of the histogram) might introduce a systematic error. Due to the level of the statistical uncertainty of this analysis, and considering the level of bias from simulation studies in previous FOCUS analyses, we find that the largest contribution to the systematic uncertainty is due to the fitting choices rather than to the Monte Carlo simulation.

6.4.1 Investigation of Bias from Simulation

To evaluate how well the Monte Carlo simulates the data we make several comparisons of variable distributions. Fig. 6.10 shows the distribution of the momentum of π^-, μ^+, π^{soft} , and K^0_S for data and Monte Carlo. In order to minimize the background contamination we select events with ΔM<0.15 GeV/c^2, therefore the events we plot are the same events that are fit in the $\cos\theta_V \times \cos\theta_\ell \times q^2$ distribution. It is crucial that the momenta are well simulated, since for all the detectors the performance (e.g. the efficiency or the misidentification rate) varies as a function of the momentum. From this comparison we find very good agreement, within errors, between simulation and real data.

The correctness of the efficiency evaluation from Monte Carlo can be inferred from studying the stability of the results versus different purities of the signal. We test the r_v, r_2, and A stability for a variation of the relevant variables used in the event selection: $p(\pi)$, $p(\mu)$, $p(\pi^{soft})$, $p(K_s)$, $M(K_s\pi)$, $M(K_s\pi\mu)$, W(K)-W(π), C.L. secondary vertex, C.L.(μ), μ track consistency in the two magnets, secondary vertex out of target, and ISO2.

The results, shown in Fig. 6.11, are stable within uncertainties. The more significant variations are observed for r_v and r_2 in the scan on $p(\mu)$. Since we use a relatively significant cut on $p(\mu)$ we have investigated it further, along with the other momenta $p(\pi)$ and $p(\pi^{soft})$. For this more detailed investigation we use the "split sample" technique described in Appendix C and derived from the S–factor method used by the Particle Data Group [39]. Briefly, the data are split into statistically independent samples, for example it is split in distinct momentum regions. The measurement is performed on each sample for the observable x (e.g. r_v) and a χ^2 for the hypothesis that the independent measurements are consistent is calculated. A poor consistency might result from badly estimated efficiency with respect to the momentum. We define

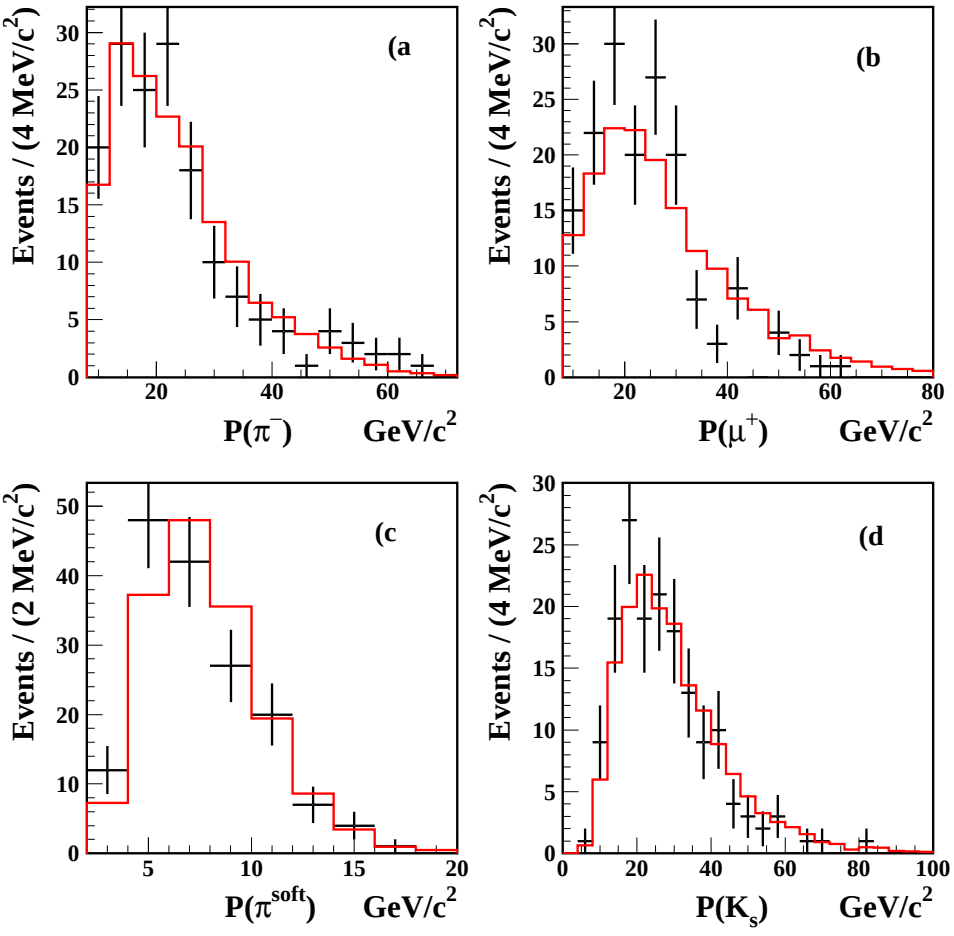

Figure 6.10: Comparison of momentum distributions for events with ΔM<0.15 GeV/c^2. a): $p(\pi^-)$, b): $p(\mu^+)$, c): $p(\pi^{soft}$), d): $p(K^0_S)$. Points with error bars are data, histogram is Monte Carlo (scaled to the number of data events).

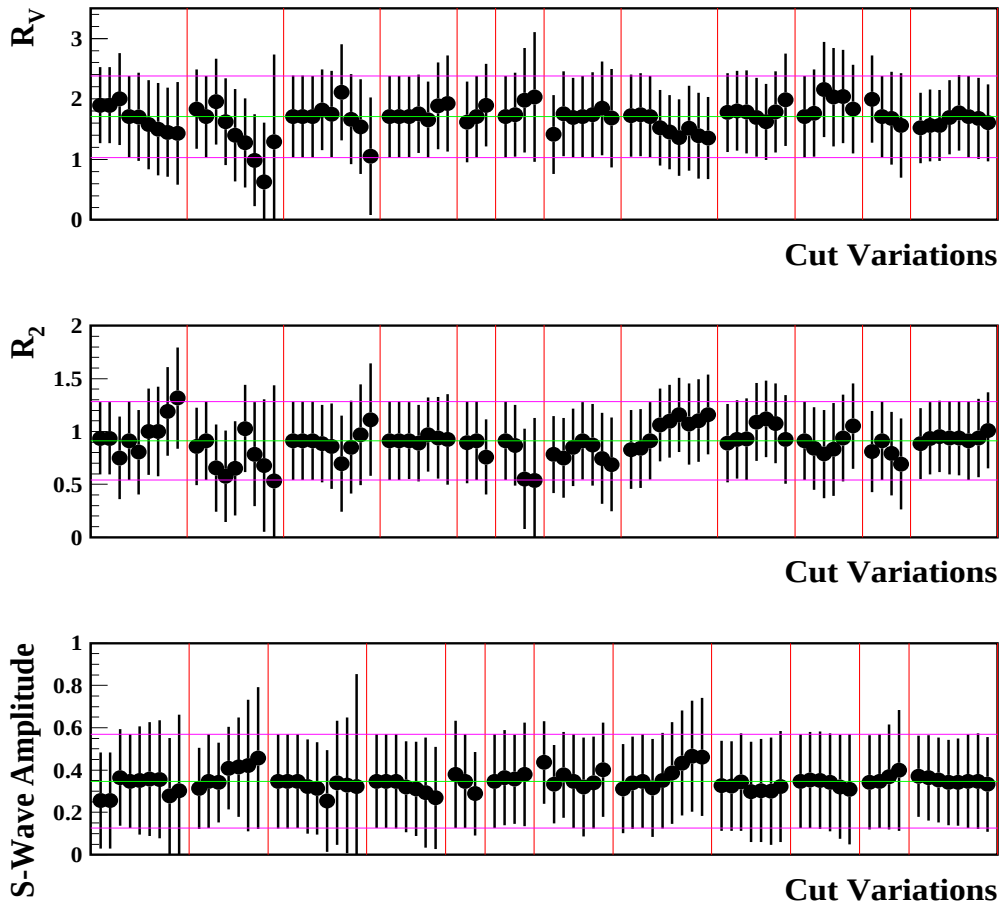

Figure 6.11: Results on r_v, r_2 and S-wave amplitude for different cut variations. From left to right the varied cuts (separated by red lines) are: $p(\pi)$, $p(\mu)$, $p(\pi^{soft})$, $p(K^0_S)$, $M(K_s\pi)$, $M(K_s\pi\mu)$, W(K)-W(π), C.L. secondary vertex, C.L.(μ), μ track consistency in the two magnets, secondary vertex out of target, and ISO2. The horizontal bands indicate the results with baseline cuts.

poor consistency to be the case where $\chi^2 > 1$. In this case the errors on the different measurements are scaled in order to return $\chi^2 = 1$, and we calculate a systematic uncertainty for the x measurement by subtracting in quadrature the statistical error from the scaled error on the weighted average of the independent measurements.

Fig 6.12 shows the results for r_v, r_2, and A for the three sets of two independent samples: $p(\pi) < 23$ GeV/c and $p(\pi) > 23$ GeV/c, $p(\mu) < 21$ GeV/c and $p(\mu) > 21$ GeV/c, $p(\pi^{soft}) < 8$ GeV/c and $p(\pi^{soft}) > 8$ GeV/c. The momentum values for the splits are given by the MC average of each momentum distribution (after wrong sign subtraction). We find no systematic uncertainty associated to the simulation of the momenta.

6.4.2 Investigation of Bias from Fitting Technique

The fitting method consists of a particular set of choices of parameters and technique. Such choices have been varied in order to evaluate how they might bias the result.

The binning in both the ΔM and $\cos\theta_V \times \cos\theta_\ell \times q^2$ distributions has been varied. The $\cos\theta_V \times \cos\theta_\ell \times q^2$ bins have been varied using more or less bins (3×3×2, 4×4×2, 4×4×1, 5×5×2). The ΔM fit was varied by using finer (0.5 MeV/c per bin) and larger (2 MeV/c per bin) bins than the standard 1 MeV/c per bin. For the r_v and r_2 fit, we include a variation where the S-wave amplitude and phase are set to zero. For the amplitude fit we vary the S-wave phase, taking the values at plus and minus one standard deviation.

A different fitting technique (which will be called "FT2") has been investigated in the course of the analysis. The final choice was selected by the one that was predicted to have a higher precision. The other fitting method is used as fit variation. FT2 is also a simultaneous fit of ΔM and $\cos\theta_V \times \cos\theta_\ell \times q^2$, but the number of expected signal events per bin is calculated in a different way. For each MC event we compute

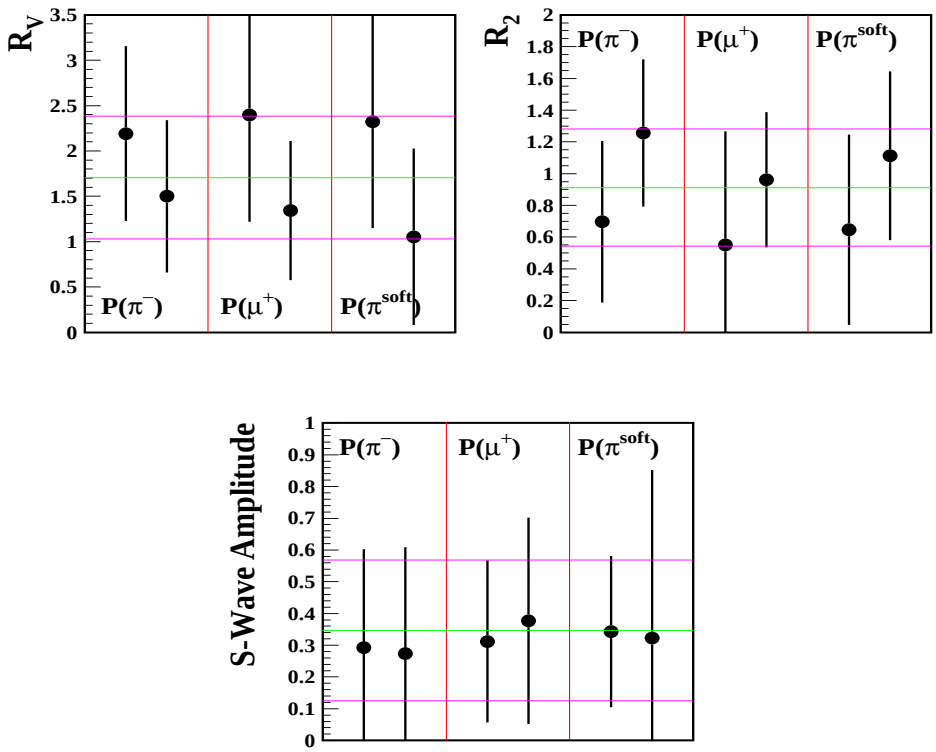

Figure 6.12: r_v, r_2, and S-wave amplitude results for the three sets of two independent samples. The sets are separated by vertical lines. For each plot: first set is $p(\pi) < 23$ GeV/c and $p(\pi) > 23$ GeV/c, second set is $p(\mu) < 21$ GeV/c and $p(\mu) > 21$ GeV/c, and third set is $p(\pi^{soft}) < 8$ GeV/c and $p(\pi^{soft}) > 8$ GeV/c. The standard results are represented by the horizontal bands.

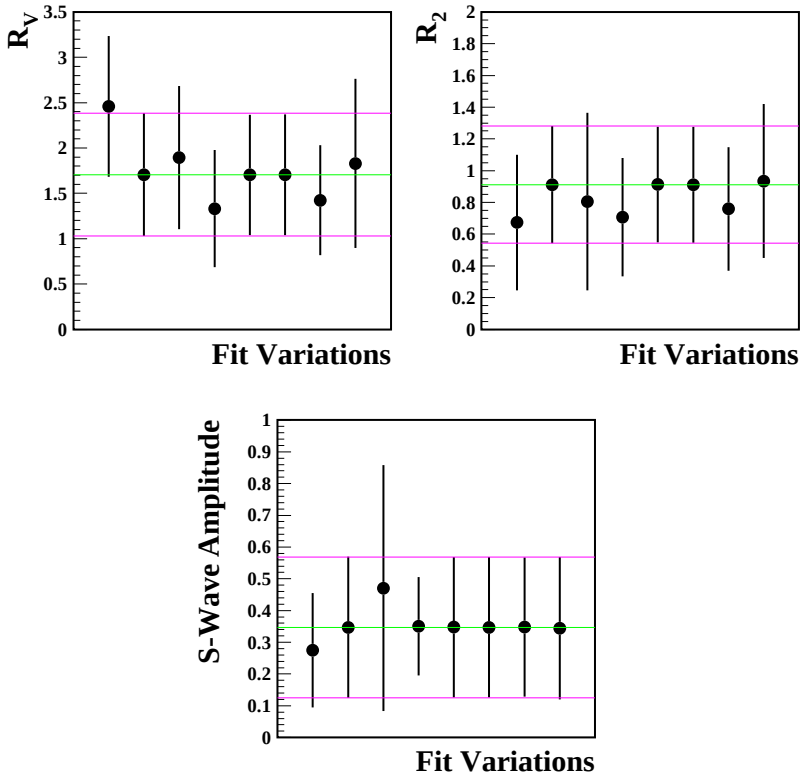

Figure 6.13: Results from fit choices variations for r_v, r_2, and S-wave amplitude. For r_v and r_2 the first four points are variations on the $\cos\theta_V \times \cos\theta_\ell \times q^2$ bins (3×3×2, 4×4×2, 4×4×1, 5×5×2), the next point is the result from the FT2 fit, the next two points are different ΔM bins (0.5 MeV/c per bin and 3 MeV/c per bin), and the last point is the fit without S-wave. For A the first four points are the different $\cos\theta_V \times \cos\theta_\ell \times q^2$ bins, the next two points are the different ΔM bins, and the last two points are different values for the S-wave phase (plus and minus one standard deviation, respectively). The horizontal bands show the results with standard parameters and method (which is the second point in each plot).

the amplitude that it was generated with, using the God's block information on the kinematic variables. Then the bin where such event was *reconstructed* is filled with such probability. The same weighting method as seen for the standard fit is used to compute the amplitude, since the MC was generated with fixed R_V and R_2 values. By filling the reconstructed bin, this method also accounts for resolution. This fitting technique has proved not sensitive enough to measure the S-wave amplitude, so it is not included in the fit variation for this parameter.

The results from fit parameters and fit technique variations are shown in Fig. 6.13. These measurements have been performed on samples that are 100% correlated and are all *a priori* likely, so the uncertainty on the measurement due to fitting choice has been evaluated as the variance of the set of measurements. We find:

$$\sigma(\text{fit})_{r_v} = 0.34$$

$$\sigma(\text{fit})_{r_2} = 0.10$$

$$\sigma(\text{fit})_A = 0.05 \text{ GeV}^{-1}$$

6.4.3 Total Systematic Uncertainty

The total systematic uncertainty is given by the sum in quadrature of the uncertainties from simulation and fit choice:

$$\sigma(\text{sys})_{r_v} = \sqrt{\sigma(\text{sim})^2 + \sigma(\text{fit})^2} = 0.34$$

$$\sigma(\text{sys})_{r_2} = \sqrt{\sigma(\text{sim})^2 + \sigma(\text{fit})^2} = 0.10$$

$$\sigma(\text{sys})_A = \sqrt{\sigma(\text{sim})^2 + \sigma(\text{fit})^2} = 0.05 \text{ GeV}^{-1}$$

The systematic uncertainties are summarized in Table 6.1. Including both statistical and systematic errors, we measure the D^0 form factor ratios and the $\overline{K}^0\pi^-$ S-wave amplitude

for the decay $D^0 \to \overline{K}^0 \pi^- \mu^+ \nu$ to be:

$$r_v = 1.71 \pm 0.68 \text{ (sta)} \pm 0.34 \text{ (sys)} \tag{6.4}$$

$$r_2 = 0.91 \pm 0.37 \text{ (sta)} \pm 0.10 \text{ (sys)} \tag{6.5}$$

$$A = 0.35 \pm 0.22 \text{ (sta)} \pm 0.05 \text{ (sys) GeV}^{-1} \tag{6.6}$$

Source	$\sigma(r_v)$	$\sigma(r_2)$	$\sigma(A)$ (GeV^{-1})
Simulation	0.	0.	0.
Fit	0.34	0.10	0.05
Total	0.34	0.10	0.05

Table 6.1: Summary of the systematic uncertainties on r_v, r_2 , and A.

Chapter 7

Measurement of the Branching Ratio $\Gamma(D^0 \to K^*(892)^-\mu^+\nu)/\Gamma(D^0 \to \overline{K}^0\pi^-\pi^+)$

In this chapter we will describe the measurement of the branching ratio $\Gamma(D^0 \to K^*(892)^-\mu^+\nu)/\Gamma(D^0 \to \overline{K}^0\pi^-\pi^+)$ and the evaluation of the systematic uncertainty.

7.1 The $D^0 \to \overline{K}^0\pi^-\pi^+$ and $D^0 \to K^*(892)^-\mu^+\nu$ Fits

The reconstruction of the semileptonic and of the hadronic modes from the final states $K^0_S\pi^-\mu^+\nu$ and $K^0_S\pi^-\pi^+$ is described in Chapter 5. As previously stated, the reconstruction and the selection cuts for the hadronic decay are chosen to be as similar as possible to the ones used for the semileptonic decay. This allows us to substantially reduce possible systematic bias in the branching ratio due to a possible poor Monte Carlo simulation of acceptance and efficiency.

The branching ratio is measured by dividing the efficiency corrected signal yield of the $D^0 \to K^*(892)^-\mu^+\nu$ mode by the efficiency corrected signal yield of the $D^0 \to \overline{K}^0\pi^-\pi^+$ mode. For each mode the signal yield is given by the number of signal events reported by the fit to the ΔM distribution. The efficiency is evaluated by dividing the Monte Carlo signal yield of the reconstructed events by the number of generated events. The efficiency corrected yield (E.C.Y.) for each mode is therefore given by:

$$\text{E.C.Y.} = \frac{\text{Yield(data)}}{\text{Efficiency}} = \text{Yield(data)} \times \frac{\#\text{Generated(MC)}}{\text{Yield(MC)}} \tag{7.1}$$

For the semileptonic mode we have seen that the simultaneous fit to ΔM and $\cos\theta_V \times \cos\theta_\ell \times q^2$ slightly underestimates the errors on the yield, so for measuring the branching ratio we fit the ΔM distribution alone. The fit is performed using the same components as for the form factor ratios measurement. The shape for the signal events is obtained from the distribution of the reconstructed events in a Monte Carlo that simulates the D^{*+} production and decay $D^{*+} \rightarrow D^0\pi^+$ with subsequent decay $D^0 \rightarrow \overline{K}^0\pi^-\mu^+\nu$. The background shape is taken from the MC_{BKG}, which as seen before simulates all known charm decays except the one under study. The fit to ΔM for the semileptonic mode is shown in Fig. 7.1. The fit reports 175±17 signal events.

For the hadronic mode we select events based on the reconstructed $\mathrm{M}(K^0_S\pi^-\pi^+)$. Fig. 7.2 shows the distribution of $\mathrm{M}(K^0_S\pi^-\pi^+)$ for data and Monte Carlo events. The two distributions are fit to a Gaussian distribution for the signal plus a first order polynomial for the background. The mass peak and width measured in data are $M = 1.868$ GeV/c^2, $\sigma = 0.012$ GeV/c^2, while in Monte Carlo they are $M = 1.866$ GeV/c^2, $\sigma = 0.012$ GeV/c^2. For both data and Monte Carlo we select events within two standard deviations of the fit $\mathrm{M}(K^0_S\pi^-\pi^+)$ mass and we fit the mass difference distribution ΔM =$\mathrm{M}(K^0_S\pi^-\pi^+\pi^{soft}$)-$\mathrm{M}(K^0_S\pi^-\pi^+)$. The ΔM distribution is fit to two Gaussian shapes for the signal events and the following threshold function for the background:

$$\mathrm{BKG}(x) = a\ (x - m_\pi)^{1/2} + b\ (x - m_\pi)^{3/2} + c\ (x - m_\pi)^{5/2} \tag{7.2}$$

The use of two Gaussian distributions provides a better fit confidence level. This is due to the fact that because of the different topologies of the decay, an average resolution is not a good representation for all events. When we used a single Gaussian we found rather poor fit confidence levels. The ΔM fits for data and Monte Carlo using two Gaussians are shown in Fig. 7.3. We measure 1918±52 events.

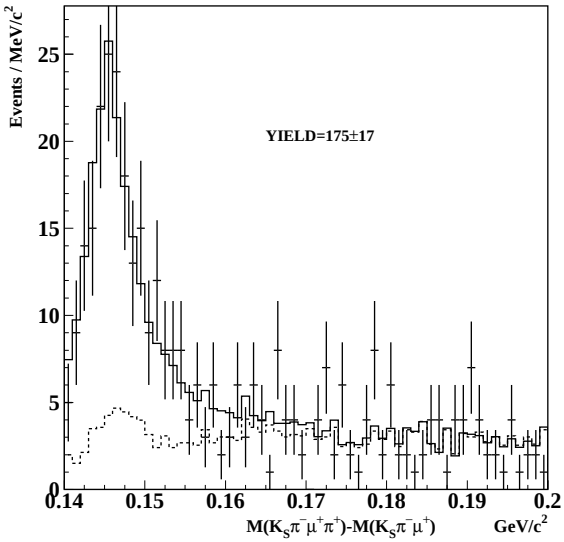

Figure 7.1: M($K^0_S\pi^-\mu^+\pi^{soft}$)-M($K^0_S\pi^-\mu^+$) distribution. Points with error bars are data, histogram is the fit, dashed line is the background component.

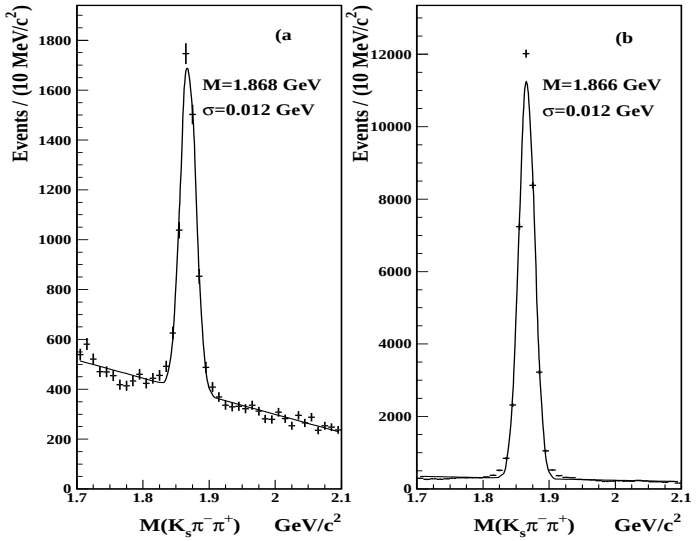

Figure 7.2: M($K^0_S\pi^-\pi^+$) distribution for a): data , b): MC. The fit is to a Gaussian plus a first order polynomial.

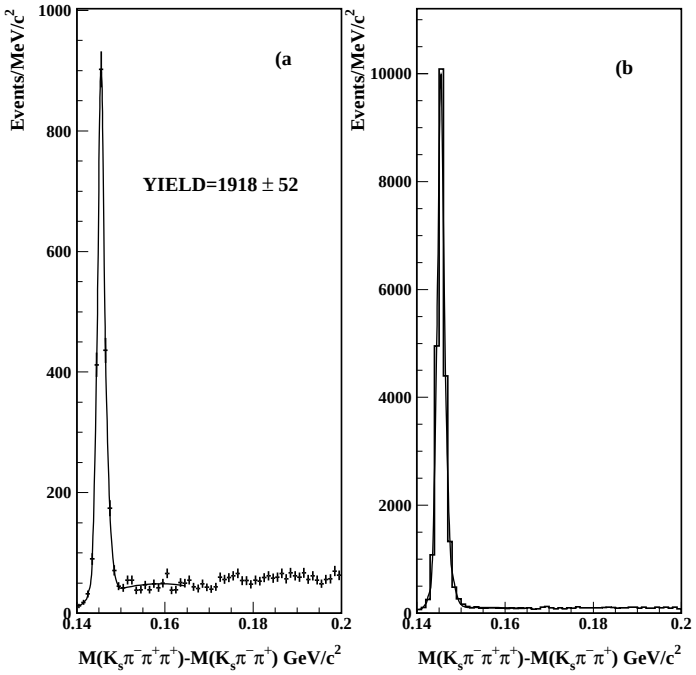

Figure 7.3: ΔM fit for a): data and b): MC. Points with error bars are data (MC) events, continuous line is the fit. The fit to two Gaussian distributions for the signal plus the threshold function in Eq. 7.2 for the background.

7.2 The Branching Ratio Measurement

For the $D^0 \to K^*(892)^-\mu^+\nu$ mode, we measure the efficiency corrected yield by reconstructing inclusively the decay $D^0 \to \overline{K}^0\pi^-\mu^+\nu$. This corrected yield must be corrected in order to account for the right amount of vector decays. We assume that Monte Carlo input S-wave parameters are very close to the parameters in data since they are determined in the much larger statistics analysis of the $D^+ \to K^-\pi^+\mu^+\nu$ decay, and they are in excellent agreement with what we have measured for the D^0 [1]. For this reason the factor that corrects the amount of $K^*(892)^-$ in the yields of data and Monte Carlo should be the same and cancel out in Eq. 7.1. The number of generated events must be corrected by the relative branching ratio $\mathcal{B}(D^0 \to K^*(892)^-\mu^+\nu)/\mathcal{B}(D^0 \to \overline{K}^0\pi^-\mu^+\nu)$ in the Monte Carlo. In order to calculate this ratio we divide the integral over phase space of the decay amplitude when only K* is generated, by the integral of the decay amplitude when the $\overline{K}^0\pi^-$ system is generated inclusively (with $K^*(892)^-$ and S-wave). The ratio of integrals is calculated numerically using a MC simulation. We find that in our MC simulation the ratio of $K^*(892)^-$ events over the total $\overline{K}^0\pi^-$ events is 0.951.

Accounting for the component of $K^*(892)^-$ events in the $D^0 \to \overline{K}^0\pi^-\mu^+\nu$ sample, we find that the relative efficiency between the semileptonic and the hadronic decay is 0.27 and we measure the branching ratio to be:

$$\frac{\Gamma(D^0 \to K^*(892)^-\mu^+\nu)}{\Gamma(D^0 \to \overline{K}^0\pi^-\pi^+)} = 0.337 \pm 0.034 \tag{7.3}$$

where the error is statistical.

7.3 The Systematic Uncertainty Evaluation

Different possible sources of systematic bias are investigated. The correctness of the Monte Carlo efficiency calculation is evaluated by studying the branching ratio

[1] The S-wave parameters measured by FOCUS for the $D^+ \to K^-\pi^+\mu^+\nu$ decay are: $A = 0.330 \pm 0.022$ (stat) ± 0.015 (sys) GeV^{-1} and $\delta = 0.68 \pm 0.07$ (stat) ± 0.05 (sys) rad.

result versus cuts variations. The bias from the fitting choices is evaluated by varying the binning and the fit range. Finally, we study the dependence of the result on different Monte Carlo input parameters.

7.3.1 Investigation of Bias in the Efficiency Evaluation

Like for the semileptonic mode (see Fig. 6.10), we compare the momenta distributions of Monte Carlo and data for the hadronic mode. As stated before, momentum simulation is crucial, as detector efficiency and misidentification levels vary with the momentum. For the comparison we require $\Delta M < 0.15\text{GeV}/c^2$, in order to reduce the amount of background. Fig. 7.4 shows the Monte Carlo distributions superimposed to data. The number of Monte Carlo events is scaled to data. The agreement is good within errors. We notice a slightly higher average K^0_S momentum for the simulation than for data. Nevertheless, the branching ratio result is stable within errors when we vary the requirement on the K^0_S momentum.

The stability of the branching ratio result has been tested versus the individual cut variations, to search for possible bias in the reconstruction efficiency calculation. Most of the cuts are identical for the two modes, so they are varied simultaneously. We vary ℓ/σ_ℓ, $p(\pi^-)$, $p(\mu^+)$ (or $p(\pi^+)$ for the hadronic mode), $p(\pi^{soft}$), $p(K^0_S)$, W(K)-W(π), C.L. of the secondary vertex, μ (or π^+ for the hadronic mode) track consistency in the two magnets, number of standard deviations of the secondary vertex being out of target, and ISO2. For the semileptonic mode we also vary the $M(K^0_S\pi)$ window, the $M(K^0_S\pi\mu)$ upper limit, and C.L.(μ). Fig. 7.5 shows the results of the study on the cut variations: the efficiency corrected yield for semileptonic and hadronic modes, and the branching ratio. All the results are stable within uncertainties. The momenta variations for the hadronic mode show variations from the result with baseline cuts that exceed one standard deviation, but the trend cancels out in the branching ratio measurement.

As for the form factor ratios, we further investigate the momenta $p(\pi^-)$, $p(\mu^+)$

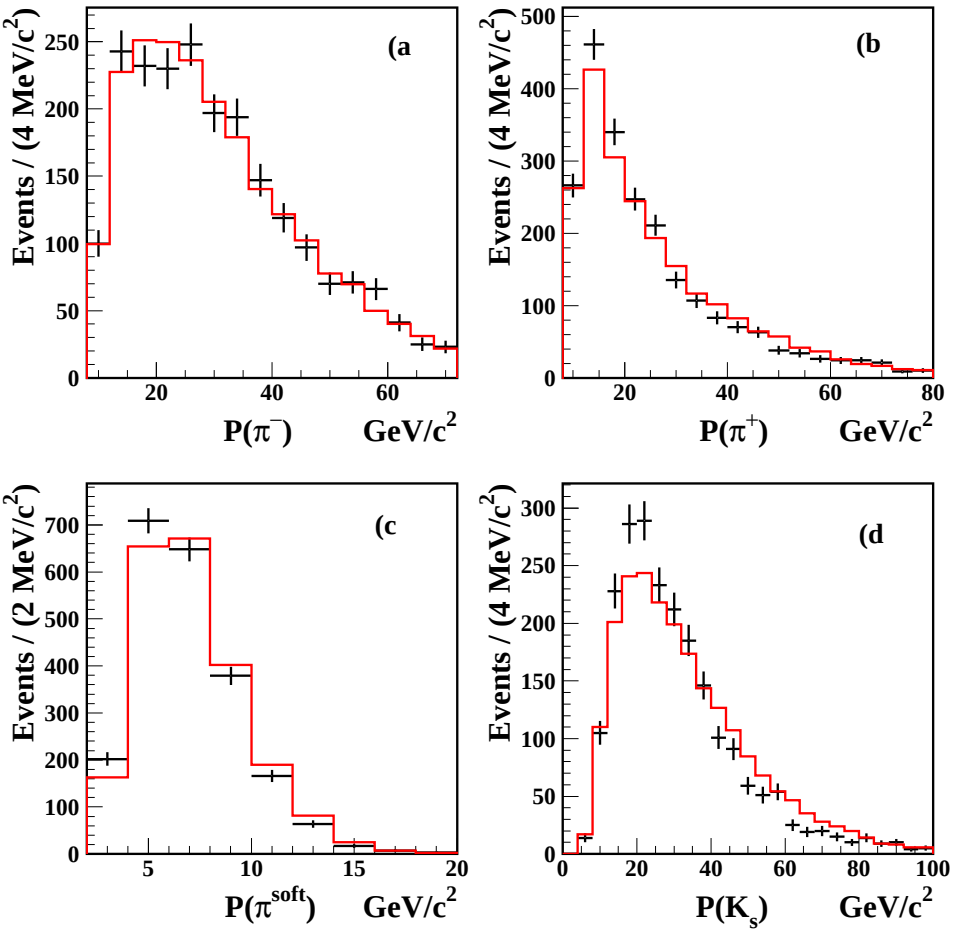

Figure 7.4: Comparison of momentum distributions between data (points with error bars) and Monte (histogram). a) and b): momentum of the pion with opposite and same sign as π^{soft} , respectively; c): $p(\pi^{soft}$); d): $p(K^0_S)$. The Monte Carlo is scaled to the number of data events.

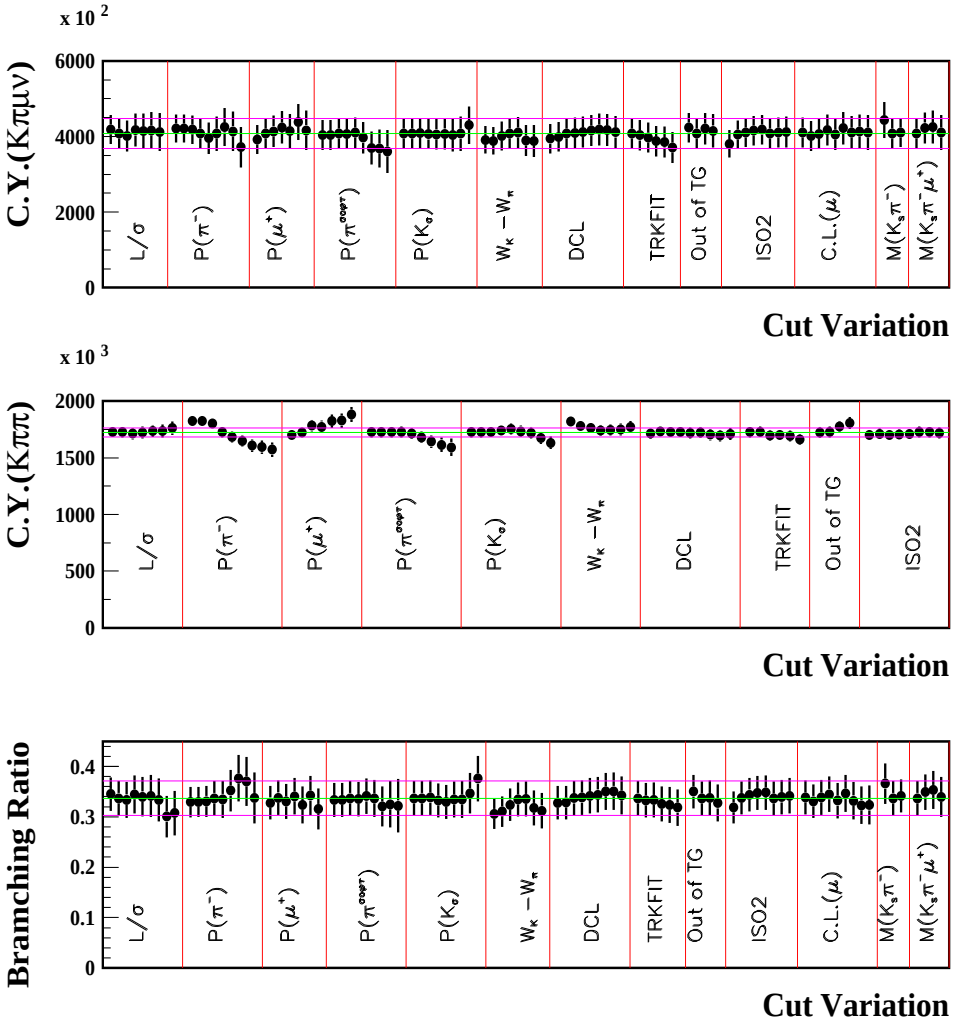

Figure 7.5: Results for different cut variations for a): $D^0 \to \overline{K}^0\pi^-\mu^+\nu$ efficiency corrected yield b): $D^0 \to \overline{K}^0\pi^-\pi^+$ efficiency corrected yield and c): ratio $\Gamma(D^0 \to K^*(892)^-\mu^+\nu)/\Gamma(D^0 \to \overline{K}^0\pi^-\pi^+)$. For each set the cut that is varied is indicated on the plot. The cuts are varied simultaneously whenever possible. The variations on C.L.(μ), $M(K^0_S\pi^-\mu^+)$, and $M(K^0_S\pi^-)$ are varied only for the semileptonic mode. The horizontal bands indicate the reference value obtained with baseline cuts.

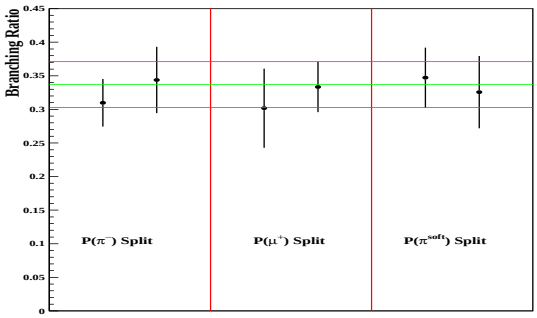

Figure 7.6: Branching ratio results for three sets of two independent samples. The sets are separated by vertical lines: first set: $p(\pi) < 23$ GeV/c and $p(\pi) > 23$ GeV/c, second set: $p(\mu) < 21$ GeV/c and $p(\mu) > 21$ GeV/c, third set: $p(\pi^{soft}) < 8$ GeV/c and $p(\pi^{soft}) > 8$ GeV/c. The standard result is represented by the horizontal band.

($p(\pi^+)$ for the hadronic mode) and $p(\pi^{soft})$ using the split sample technique described in Appendix C. Fig. 7.6 shows the branching ratio results for the three sets of two independent samples. The split sample technique reports no systematic bias from the simulation of the momenta.

7.3.2 Investigation of Bias from Fitting Choices

The bias on the branching ratio result due to fitting choices has been evaluated by varying the bin size (0.5 MeV/c^2 per bin and 1 MeV/c^2 per bin), and by varying the fit range. For $K\pi\pi$ the fit ranges 0.141 – 0.150 GeV/c^2 and 0.141 – 0.190 GeV/c^2 have been used in addition to the standard 0.141 – 0.165 GeV/c^2 range, and ΔM for $K\pi\mu\nu$ has been fit in the ranges 0.140 – 0.184 GeV/c^2 and 0.141 – 0.170 GeV/c^2 in addition to the standard 0.140 – 0.200 GeV/c^2 fit region. Fig. 7.7 shows the results for each variation. As all the measurements are *a priori* likely, the uncertainty is given by the variance of the measurement. We find:

$$\sigma(\text{fit})_{BR} = 0.002$$

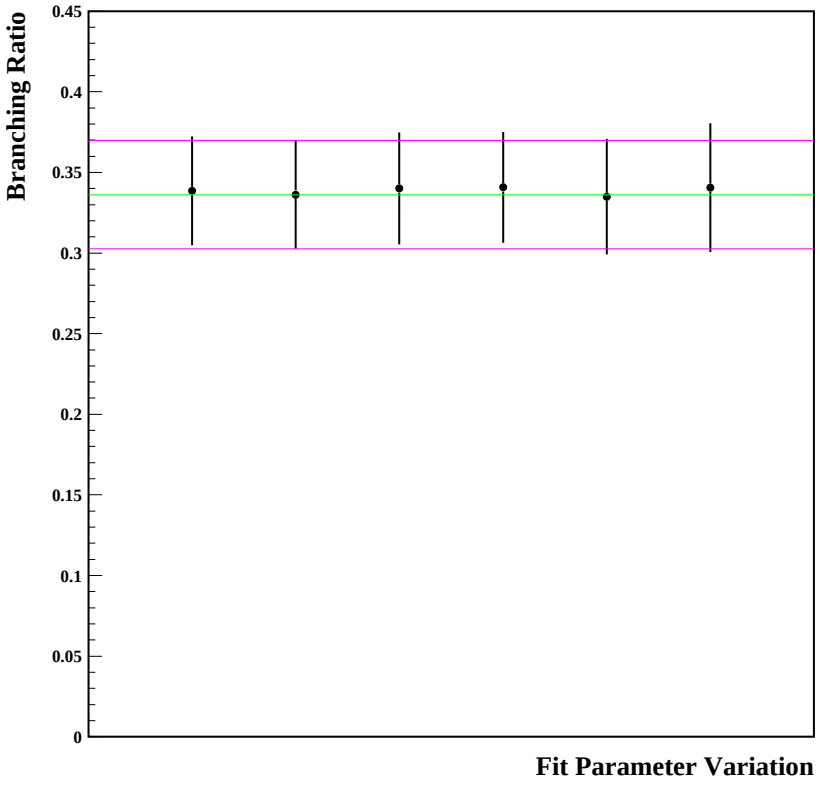

Figure 7.7: Branching ratio results for different choices of fitting parameters, from left to right: 0.5 MeV/c^2 per bin, 1 MeV/c^2 per bin, ΔM for $K\pi\pi$ fit range = 0.141 – 0.150 GeV/c^2 and 0.141 – 0.190 GeV/c^2, ΔM for $K\pi\mu\nu$ fit range = 0.140 – 0.184 GeV/c^2 and 0.140 – 0.170 GeV/c^2.

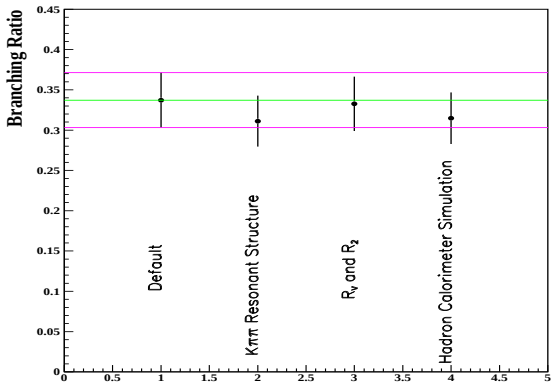

Figure 7.8: The branching ratio results for different input parameters in the Monte Carlo are compared to the result with default model used in the simulation.

7.4 Uncertainty from Monte Carlo Input Model

In order to run the Monte Carlo simulation, one has to choose different parameters. We call the standard choice the "input model". We have varied this input model in three different ways to estimate the systematic bias introduced by our choices.

The first variation concerns the description of the normalizing mode. The decay $D^0 \to \overline{K}^0\pi^-\pi^+$ occurs through different possible resonant structures which are determined experimentally. The different structures may have different reconstruction efficiency and we want to study how the efficiency changes within a range of reasonable alternatives for the different components. We recomputed the efficiency using a resonant structure that is more similar to the recent BaBar result [40]. The main difference consists of lowering the $K^*(892)^-$ component (from 63.8% to 60%), raising the $K^*(1430)^0$ component (from 6.7% to 9%) and the non–resonant component (from practically 0 to 1%). With the new resonant structure we find a small increase (from 0.27 to 0.29) in the relative efficiency of the semileptonic decay over the hadronic decay.

In order to determine the dependence of the branching ratio result on the value of the form factor ratios and of the S-wave parameters used in Monte Carlo, we run a

new simulation using a different set of values. The values for the variation (r_v= 1.733, r_2 =0.890, A=0.33, and δ=1.09) were chosen from an analysis when a slightly different set of cuts were used. A fit in which the S-wave phase was allowed to freely float was run, in order to determine the value used in the variation. We find no significant difference in the efficiency between the default input model and the varied input model.

The branching ratio measurement is performed using a hadronic and a semileptonic mode. The normalization channel is chosen in such a way that some possible systematic biases equally affect the two modes and cancel out in the ratio (for instance for the K^0_S). Nevertheless there is a substantial difference between the two modes in the amount of hadronic energy in the final state. Due to this difference, a possible bias in the Monte Carlo modeling of the trigger (which uses information from the hadronic calorimeter) may not cancel out in the ratio. We evaluate the size of this effect by using a different, more "crude" simulation of the hadronic calorimeter. The relative efficiency of the two modes changes from 0.27 to 0.29.

The branching ratio result with default Monte Carlo input model is compared to the three model variations in Fig. 7.8. All the results using a varied model are in excellent agreement with our measurement. We calculate the systematic uncertainty from the three sources combined to be:

$$\sigma(\text{model})_{BR} = 0.013$$

and we conclude that the bias introduced from the uncertainties on the $D^0 \to \overline{K}^0\pi^-\pi^+$ resonant structure, from the input values for the semileptonic decay amplitude, and from the simulation of the hadron calorimeter used for the trigger do not affect significantly our measurement.

7.4.1 Total Systematic Uncertainty

Three sources of systematic uncertainty have been evaluated, the Monte Carlo determination of acceptance and reconstruction efficiency, the choice of fit parameters, and the choice of input model for the Monte Carlo. These are independent sources and their contributions are summed in quadrature to find the total systematic uncertainty. We find:

$$\sigma(\text{sys})_{\text{BR}} = \sqrt{\sigma(\text{sim})^2 + \sigma(\text{fit})^2 + \sigma(\text{mod})^2} = 0.013$$

The systematic uncertainty results are summarized in Table 7.1. Including statistical and systematic errors, we measure the branching ratio to be:

$$\frac{\Gamma(D^0 \to K^*(892)^- \mu^+ \nu)}{\Gamma(D^0 \to \overline{K}^0 \pi^- \pi^+)} = 0.337 \pm 0.034 \text{ (stat)} \pm 0.013 \text{ (sys)}$$

Source	σ(BR)
Simulation	0.000
Fit	0.002
Model	0.013
Total	0.013

Table 7.1: The systematic uncertainties from the Monte Carlo efficiency and acceptance evaluation, the fitting condition, and from the input parameters and trigger simulation in the Monte Carlo are shown.

Chapter 8

Conclusions

In this chapter we discuss the importance of investigating semileptonic decays in the heavy quark sector and we summarize the results of the analysis of the decay $D^0 \to \overline{K}^0 \pi^- \mu^+ \nu$.

8.1 Semileptonic Decays in the Heavy Quark Sector

Semileptonic decays are accessible to experiment since they have relatively large branching fractions ($\sim 5\%$) and can easily be separated from backgrounds. In the last two decades the semileptonic decay of heavy mesons ($B \to D^{(*)} \ell\nu$, $D \to K^{(*)} \ell\nu$), have been extensively investigated both from experiments and from theory. These decays are an excellent environment for determining the Cabibbo-Kobayashi-Maskawa matrix elements in the heavy quark sector, since they depend on a single matrix element which can be factorized out of the decay amplitude:

$$\Gamma = |V_{Qq'}| \cdot \Gamma_0 \tag{8.1}$$

Semileptonic decays are also crucial for investigating QCD. Although the decay occurs through a weak interaction, the picture is complicated by QCD effects due to the fact that the quarks are confined into an hadron (both in the initial and final states). These decays are characterized by a low momentum transfer (q^2) between the parent and the daughter meson compared to the mass of the intermediate boson W. In this

energy range, Γ_0 can be written as a product of a well determined leptonic current times an hadronic current. The determination from first principles of the hadronic current is not completely possible, but it can be built as a $V - A$ weak current parameterized through the form factors, where all the QCD effects are confined.

Form factors can be calculated by theory (quark models [7, 8, 9, 10, 11, 12, 13], lattice QCD [14, 15, 16, 17, 18], and sum rules [19]). In the charm sector, where V_{cs} is well known, direct comparison between theory and experiment allows for arbitration between different assumptions and for the adjustment of input parameters. Also the measurements of semileptonic branching ratios are used as guidelines for theory (for instance, in quark models they are used to fit for the quark masses and their wave function parameters, which are then used to calculate the form factors). These comparisons between theory and experiment are necessary for constructing a successful model of hadrons. Once the theoretical tools have been built in the charm sector, they can be used in other sectors, such as in the semileptonic decay of the bottom hadrons, or in fully hadronic decays. In the bottom sector the calculation of form factors would allow, after comparison with the decay rates, a better estimate of $|V_{ub}|$ and $|V_{cb}|$. An improved hadron model is required in the fully hadronic decays. At the moment Heavy Quark Effective Theory (HQET) is the most reliable model applied to fully hadronic decays [41]. This model is based on the assumption that the mass m_Q of the heavy quark in the hadron is much larger than the scale of the momentum transfer to the light quark ($\Lambda_{QCD} \simeq 0.3$ GeV/c^2). In HQET the calculations are based on expansions in $1/m_Q$. The charm quark is light and it is at the limit of the approximation. Although HQET works well in the bottom sector, there is some evidence that even the bottom quark might be not heavy enough for the approximation.[1]

[1] One evidence comes from the lifetime of the bottom baryon Λ_b, which is lower than the expected value from HQET.

8.2 Summary of the Analysis of the Decay $D^0 \to \overline{K}^0\pi^-\mu^+\nu$

This thesis concerns the semileptonic decay $D^0 \to \overline{K}^0\pi^-\mu^+\nu$ using FOCUS data. Previous to the FOCUS experiment, the decay $D \to K\pi\ell\nu$ had been treated as a vector resonant decay $D \to K^*\ell\nu$. In the course of the FOCUS analysis of $D^+ \to K^-\pi^+\mu^+\nu$ [20, 27], clear evidence for a spin zero component of the $\overline{K}^0\pi^-$ system was reported. This high statistics study showed that a very good representation for the data was given by a model where the $K^*(892)^-$ interferes with an S-wave component with constant amplitude and phase over the M($\overline{K}^0\pi^-$) region around 0.892 GeV/c^2. The presence of the small S-wave component can be inferred from the interference with the $K^*(892)^-$. The main feature of this interference is that the decay amplitude is not symmetric with respect to $\cos\theta_V$, the angle between the π from the $K^*(892)^-$and the D in the $K^*(892)^-$rest frame

In studying the decay $D^0 \to \overline{K}^0\pi^-\mu^+\nu$ we have searched for the same evidence. Unfortunately, the D^0 sample has much lower statistics compared to the D^+ and the efficiency dependence on variables that are crucial for the S-wave investigation reproduces similar behavior to the one generated by the S-wave. We find the model including S-wave is only marginally better at describing our data than the model with pure $K^*(892)^-$. We decided to use a model that includes the S-wave component. Based on isospin symmetry, we fix the S-wave phase to 0.68, the value measured for the $D^+ \to K^-\pi^+\mu^+\nu$ decay. The possible bias due to assuming the presence of an S-wave contribution is included in the systematic uncertainty.

8.3 Measurements of r_v, r_2, and A

The form factor ratios and the S-wave amplitude have not been measured for the decay $D^0 \to \overline{K}^0\pi^-\mu^+\nu$. We extract their values from a simultaneous fit to the mass difference $M(D^*)-M(D) = \Delta M$ and the $\cos\theta_V \times \cos\theta_\ell \times q^2$ distributions. In this fit the

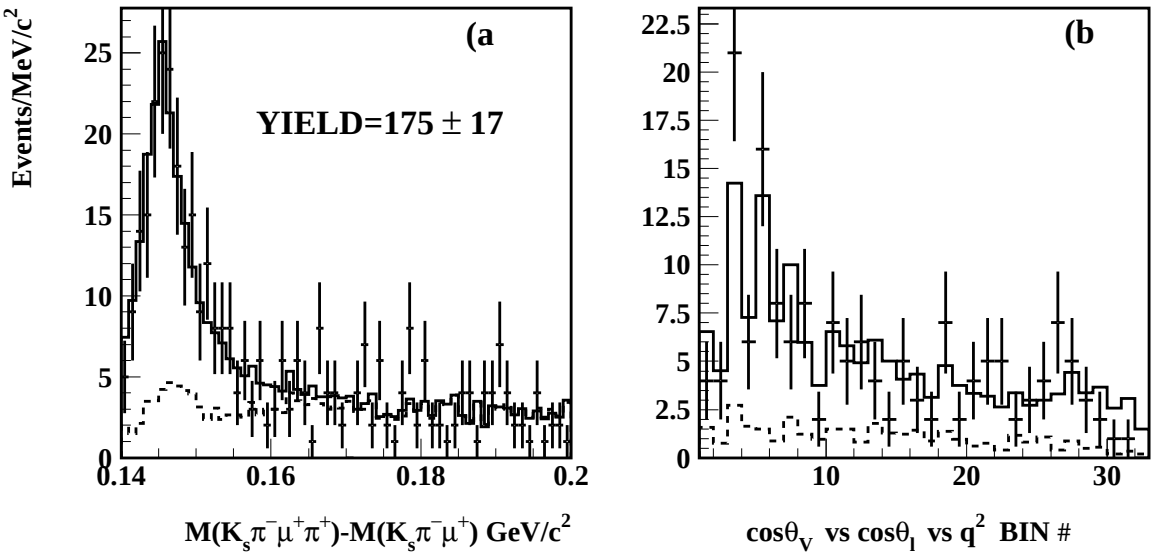

Figure 8.1: The results from the simultaneous fit to ΔM (a) and $\cos\theta_V \times \cos\theta_\ell \times q^2$ (b) are shown. Points with error bars are data, solid histogram is the fit, dashed histogram is the background component.

amplitude and phase of the S-wave are fixed to the values measured by FOCUS for the $D^+ \to K^-\pi^+\mu^+\nu$ decay, $A = 0.330$ and $\delta = 0.68$. The fit is shown in Fig. 8.1. We find 175 ± 17 events. The χ^2 per degree of freedom in Fig. 8.1b is 32/27 which corresponds to a confidence level of 22%. We then fix r_v and r_2 to the values we measure and we fit for A.

All results are stable within errors when the selection cuts are varied. The systematic uncertainty is determined by studying two possible sources of bias, the Monte Carlo evaluation of the acceptance and efficiency, and the fitting choices. Using the split sample method described in Appendix C we find no contribution to the uncertainty from Monte Carlo simulation. By varying the binning in the ΔM and the $\cos\theta_V \times \cos\theta_\ell \times q^2$ distributions and the fitting method, we evaluate a systematic uncertainty due to fitting choices.

We measure the form factor ratios and the S-wave amplitude to be:

$$r_v = 1.71 \pm 0.68 \pm 0.34 \tag{8.2}$$

$$r_2 = 0.91 \pm 0.37 \pm 0.10 \tag{8.3}$$

$$A = 0.35 \pm 0.22 \pm 0.05 \text{ GeV}^{-1} \tag{8.4}$$

where first error is statistical and second error is systematic. Using our result for A, we find that the S-wave component is 6% of the $\overline{K}^0\pi^-$ system.

As stated before all the measurements presented in this thesis are first measurements, but based on isospin symmetry we can compare the results with the measurements using the $D^+ \to K^-\pi^+\mu^+\nu$ decay. The S-wave amplitude has only been measured by the FOCUS experiment for the D^+ decay. The results from the two isospin conjugate modes, which are shown in Table 8.1, are in excellent agreement.

Several experiments have measured the form factor ratios for the decay $D^+ \to K^-\pi^+\mu^+\nu$ [20, 21, 22, 23, 24, 25, 26]. None of these measurements include the S-wave component, except for the FOCUS analysis. Fig. 8.2 shows a comparison of our

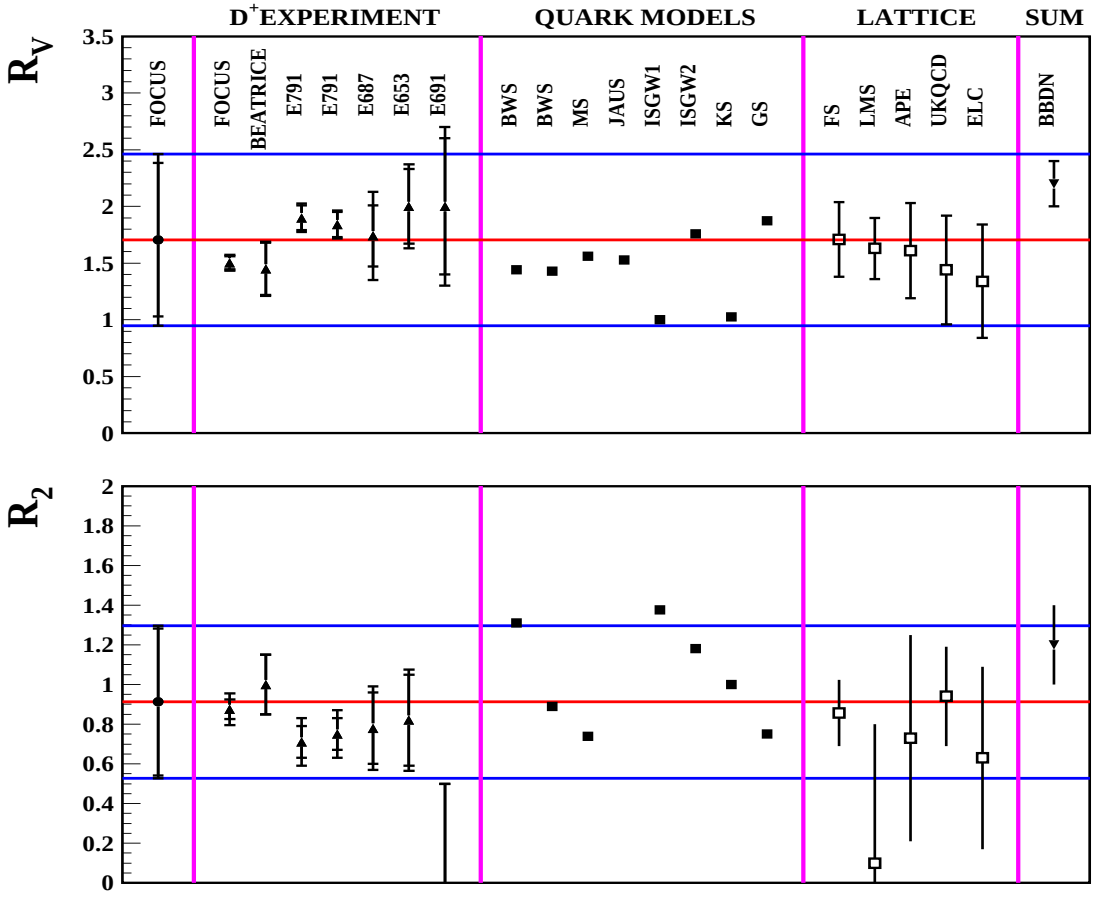

Figure 8.2: Our measurement of r_v and r_2 for the decay $D^0 \to \overline{K}^0\pi^-\mu^+\nu$ (first point) is compared to the measurements for the $D^+ \to K^-\pi^+\mu^+\nu$ decay [20, 21, 22, 23, 24, 25, 26], to theoretical calculations from quark models [7, 8, 9, 10, 11, 12, 13], from lattice QCD [14, 15, 16, 17, 18], and from sum rules [19]. We label the theoretical calculations from the authors or the collaboration name (see references). The error bars for experimental results include statistical and systematic errors (added in quadrature), the component from statistical uncertainty is indicated by the mark.

	$D^0 \to \overline{K}^0\pi^-\mu^+\nu$	$D^+ \to K^-\pi^+\mu^+\nu$
$A(\mathrm{GeV}^{-1})$	$0.35 \pm 0.22 \pm 0.05$	$0.330 \pm 0.022 \pm 0.015$

Table 8.1: The measurement of A presented in this thesis is compared to the FOCUS result for the decay $D^+ \to K^-\pi^+\mu^+\nu$. We fix the S-wave phase to 0.68, the value measured for the D^+.

results for r_v and r_2 to previous measurements and to theoretical predictions from quark models, lattice QCD, and sum rules. In all cases the agreement is excellent.

8.3.1 Measurement of $\Gamma(D^0 \to K^*(892)^-\mu^+\nu)/\Gamma(D^0 \to \overline{K}^0\pi^-\pi^+)$

In order to measure the semileptonic vector branching ratio, we use the normalization mode $D^0 \to \overline{K}^0\pi^-\pi^+$. This decay is similar to the semimuonic mode, since it contains a K^0_S in the final state and it has the same track multiplicity. This allows for us to apply most of the requirements used for the semileptonic mode to the hadronic mode, and therefore reduce possible bias due to poor Monte Carlo evaluation of the efficiency. For the $D^0 \to \overline{K}^0\pi^-\pi^+$ decay, we select events that lie within two standard deviations of the fit D^0 mass and we fit the ΔM distribution. This fit uses two Gaussian distributions for the signal events plus the threshold function in Eq. 7.2 for the background. The fit is shown in Fig. 8.3. We find 1918 ± 52 events.

In order to measure the branching ratio, we divide the efficiency corrected yields of the two modes. In the semimuonic mode we correct for the amount of $K^*(892)^-$ in the $\overline{K}^0\pi^-$ system. The systematic uncertainty is determined from careful studies of three different sources. The variance of a set of measurements obtained by varying the fitting range and bin size is taken as the bias due to the fit choices. We use the split sample method described in Appendix C to investigate bias due to poor momentum simulation. Finally, we determine a bias due to the input model for the Monte Carlo. For this study we investigate the $D^0 \to \overline{K}^0\pi^-\pi^+$ resonant structure, the hadron calorimeter simulation, and the input values of r_v, r_2, A, and δ (the S-wave-phase).

We measure the branching ratio to be:

$$\frac{\Gamma(D^0 \to K^*(892)^-\mu^+\nu)}{\Gamma(D^0 \to \overline{K}^0\pi^-\pi^+)} = 0.337 \pm 0.034 \pm 0.013 \tag{8.5}$$

where the first error is statistical and the second is systematic.

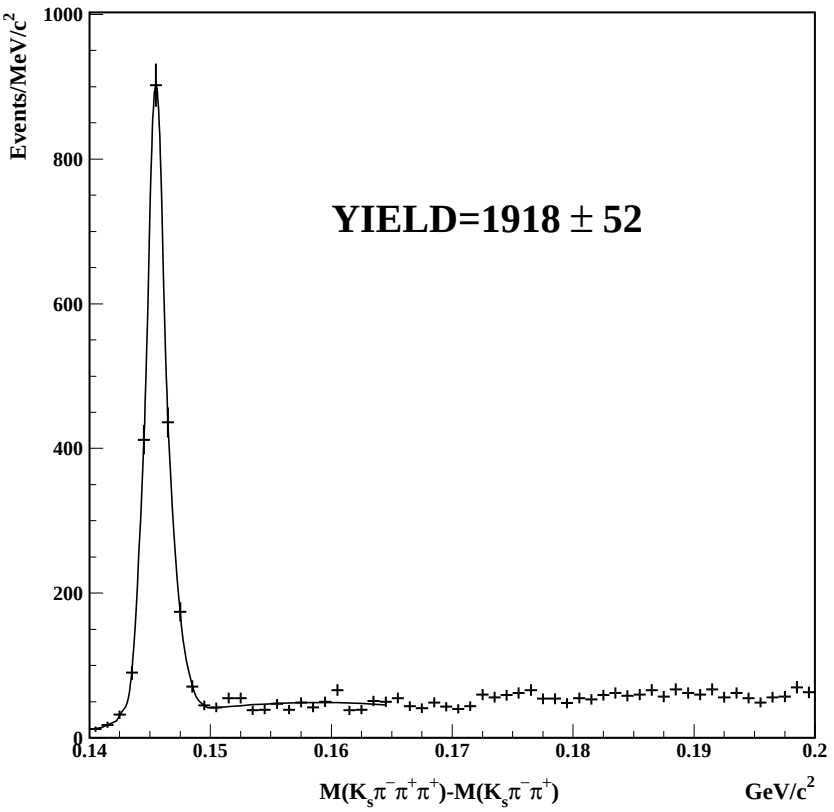

Figure 8.3: Fit to ΔM for the hadronic mode. The fit is to two Gaussian distributions for the signal plus a threshold function for the background.

This branching ratio has not been previously reported for the semimuonic channel, but the expected value can be calculated in different ways. Isospin symmetry gives:

$$\Gamma(D^0 \to K^{*-}\mu^+\nu) = \Gamma(D^+ \to K^{*0}\mu^+\nu) \tag{8.6}$$

For both charm species the absolute branching fraction can be written as:

$$\mathcal{B}(D^{0/+} \to K^*\mu\nu) = \frac{\Gamma(D^{0/+} \to K^*\mu\nu)}{\Gamma(D^{0/+})} \times \frac{\mathcal{B}(D^{0/+} \to K\pi\pi)}{\mathcal{B}(D^{0/+} \to K\pi\pi)} \tag{8.7}$$

Using equation 8.6 and 8.7, we find:

$$\frac{\Gamma(D^0 \to K^{*-}\mu^+\nu)}{\Gamma(D^0 \to \overline{K^0}\pi^-\pi^+)} = \frac{\Gamma(D^+)}{\Gamma(D^0)} \times \frac{\Gamma(D^+ \to K^{*0}\mu^+\nu)}{\Gamma(D^+ \to K^-\pi^+\pi^+)} \times \frac{\mathcal{B}(D^+ \to K^-\pi^+\pi^+)}{\mathcal{B}(D^0 \to \overline{K^0}\pi^-\pi^+)}$$

$$= \frac{410 \pm 1.9 \text{ fs}}{1039 \pm 8.2 \text{ fs}} \times (0.602 \pm 0.02) \times \frac{0.092 \pm 0.006}{0.0597 \pm 0.0035} \tag{8.8}$$

$$= 0.366 \pm 0.034$$

where we use the *Particle Data Group* [39] values for the D absolute branching fractions $\mathcal{B}(D^{0/+} \to K\pi\pi)$, and the FOCUS measurements for the D mesons lifetimes [42] and for the branching ratio $\Gamma(D^+ \to K^{*0}\mu^+\nu)/\Gamma(D^+ \to K^-\pi^+\pi^+)$ [43]. The systematic and statistical errors on the single measurements in Eq. 8.8 have been added in quadrature before determining the propagated error.

Another evaluation of the branching ratio value can be derived from the CLEO II measurement [44] of the branching ratio for the semielectronic channel:

$$\frac{\Gamma(D^0 \to K^{*-}e^+\nu_e)}{\Gamma(D^0 \to \overline{K^0}\pi^-\pi^+)} = 0.38 \pm 0.06 \text{ (stat)} \pm 0.03 \text{ (sys)}$$

The CLEO-c experiment recently measured the absolute branching fraction of $D^0 \to K^{*-}e^+\nu_e$ [45] to be $(2.07 \pm 0.23 \pm 0.18)\%$. This measurement can be used

along with the *Particle Data Group* value for the $D^0 \to \overline{K}^0\pi^-\pi^+$ branching fraction to calculate the semielectronic branching ratio:

$$\frac{\Gamma(D^0 \to K^{*-}e^+\nu)}{\Gamma(D^0 \to \overline{K}^0\pi^-\pi^+)} = \frac{\mathcal{B}(D^0 \to K^{*-}e^+\nu_e)}{\mathcal{B}(D^0 \to \overline{K}^0\pi^-\pi^+)}$$

$$= \frac{2.07 \pm 0.29}{5.97 \pm 0.35} = 0.35 \pm 0.06 \qquad (8.9)$$

where the branching fraction statistical and systematic errors have been added in quadrature before computing the propagated error. The decay dynamics of the semimuonic and the semielectronic modes are identical, differences in the decay amplitude are only due to the larger mass of the muon as compared to the electron. As the muon is more massive, there is a reduction in phase space and a more significant contribution from the term $\sim m^2$ of the decay amplitude (see equation 1.7). According to the *Particle Data Group*, the electron values must corrected by a factor of 0.952 to compare to the muon results.

The comparison of our branching ratio measurement with the semielectronic results and with the estimate from isospin invariance is shown in Fig. 8.4. Only the calculation from isospin symmetry includes the effects of the S–Wave component. We find excellent agreement between our measurements and all of the estimates, which come from different measurements.

8.4 Summary and Prospects

We have described in detail the analysis of the decay $D^0 \to \overline{K}^0\pi^-\mu^+\nu$ using FOCUS data. We report for the first time the measurements of the form factor ratios r_v and r_2, the S-wave amplitude and of the branching ratio $\Gamma(D^0 \to K^*(892)^-\mu^+\nu)/\Gamma(D^0 \to$

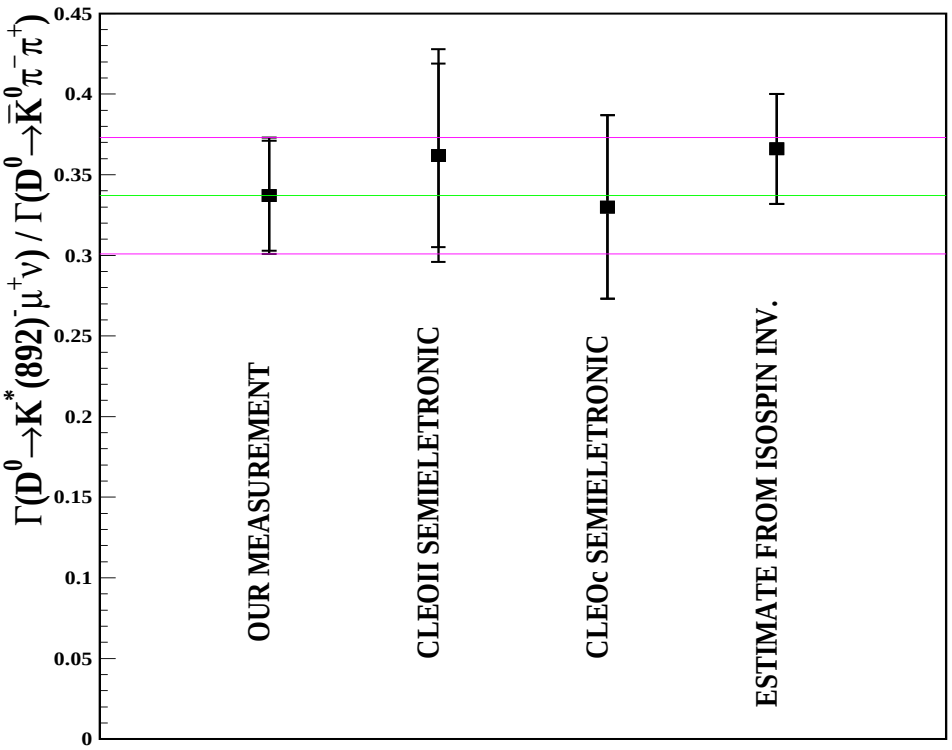

Figure 8.4: The $\Gamma(D^0 \to K^*(892)^-\mu^+\nu)/\Gamma(D^0 \to \overline{K}^0\pi^-\pi^+)$ FOCUS measurement is compared to the CLEO–II measurement of the semielectronic mode $(D^0 \to K^{*-}(892)e^+\nu/D^0 \to \overline{K^0}\pi^-\pi^+)$, with the CLEO–c measurement of $\mathcal{B}(D^0 \to K^{*-}e^+\nu_e)$ divided by the *Particle Data Group* average for $\mathcal{B}(D^0 \to \overline{K^0}\pi^-\pi^+)$, and to an estimate from isospin symmetry using the FOCUS measurement of $D^+ \to K^-\pi^+\mu^+\nu$. The semielectronic results are corrected to account for the smaller electron mass when compared to the muon, they do not include the S–Wave component. For the first two points the error bars indicate the sum in quadrature of the statistical and systematic error and the mark indicates the statistical error alone. The estimates in the last two points are determined using results from different experiments. To calculate the error we add in quadrature statistical and systematic uncertainty on each value used and we propagate such errors in order to determine the uncertainty on the estimate.

$\overline{K}^0\pi^-\pi^+$). We measure:

$$r_v = 1.71 \pm 0.68 \pm 0.34 \tag{8.10}$$

$$r_2 = 0.91 \pm 0.37 \pm 0.10 \tag{8.11}$$

$$A = 0.35 \pm 0.22 \pm 0.05 \text{ GeV}^{-1} \tag{8.12}$$

$$\frac{\Gamma(D^0 \to K^*(892)^-\mu^+\nu)}{\Gamma(D^0 \to \overline{K}^0\pi^-\pi^+)} = 0.337 \pm 0.034 \pm 0.013 \tag{8.13}$$

where first error is statistical and second is systematic. All of these measurements are in very good agreement with the expected values obtained from isospin symmetry and from results that use the semielectronic channel.

Although limited by statistics, these results are important confirmations of the expected values for the never before investigated mode $D^0 \to \overline{K}^0\pi^-\mu^+\nu$. The era of experiments fully dedicated to charm studies is close to its end. The future of charm physics resides in the experiments where particles containing the b quark are produced copiously (the so called "b–factories"). In these experiments charm particles can be produced either directly from the process $e^+e^- \to c\bar{c}$, or indirectly from the Cabibbo favored decays of bottom hadrons to charm hadrons. The study of the decay $D^0 \to \overline{K}^0\pi^-\mu^+\nu$ has just begun, but much higher statistics samples are necessary to extract additional information on the underlying physics. Using a higher statistics sample the S-wave model for the D^0 could be conclusively tested, and an adequate sensitivity to measure the r_3 form factor ratio could be reached. For this analysis we have assumed the q^2 dependence of the form factors is given by the pole mass form:

$$A_i(q^2) = \frac{A_i(0)}{1 - \frac{q^2}{M_A^2}} \tag{8.14}$$

$$V(q^2) = \frac{V(0)}{1 - \frac{q^2}{M_V^2}} \tag{8.15}$$

where M_A and M_V are the masses of two excited $c\bar{s}$ states with axial and vector quantum numbers ($J^P = 1^+$ and $J^P = 1^-$, respectively). This q^2 dependence has been

recently investigated by the FOCUS collaboration for the decay $D^0 \rightarrow K^-\mu^+\nu$ [46]. For this decay only M_V is a parameter of the decay amplitude. The study reports a pole mass that is more than 4σ lower than the expected pole mass. A modified pole mass dependence where the form factor $f(q^2)$ has the form:

$$f(q^2) = \frac{f(0)}{\left(1 - \frac{q^2}{M_V^2}\right)\left(1 - \alpha\frac{q^2}{M_V^2}\right)} \tag{8.16}$$

has also been investigated for such analysis. The parameter α, which measures the distortion from the pole mass ansatz, has been measured to be different from zero ($\alpha = 0.28 \pm 0.08 \pm 0.07$). Due to the limited statistics the q^2 dependence has never been tested for the decay $D^0 \rightarrow \overline{K}^0\pi^-\mu^+\nu$. As quark models assume a functional dependence on q^2 for the form factors, these experimental studies are extremely important. In the future we expect that they will be thoroughly investigated for the $D^0 \rightarrow \overline{K}^0\pi^-\mu^+\nu$ mode.

Bibliography

[1] S. Weinberg, Phys. Rev. Lett. **19**, 1264 (1967).

[2] S. L. Glashow, J. Iliopoulos and L. Maiani, Phys. Rev. D **2**, 1285 (1970).

[3] S. P. Martin, arXiv:hep-ph/9709356.

[4] J. H. Schwarz, Lectures given at 11th Advanced Study Institute on Techniques and Concepts in High Energy Physics, St. Croix, U.S. Virgin Islands, 15-26 Jun 2000. arXiv:hep-ex/0008017.

[5] P. Langacker, Phys. Rept. **72**, 185 (1981).

[6] M. Kobayashi and T. Maskawa, Prog. Theor. Phys. **49**, 652 (1973).

[7] M. Wirbel, B. Stech and M. Bauer, Z. Phys. C **29**, 637 (1985).

[8] D. Melikhov and B. Stech, Phys. Rev. D **62**, 014006 (2000).

[9] W. Jaus, Phys. Rev. D **53**, 1349 (1996) [Erratum-ibid. D **54**, 5904 (1996)].

[10] N. Isgur, D. Scora, B. Grinstein and M. B. Wise, Phys. Rev. D **39**, 799 (1989).

[11] D. Scora and N. Isgur, Phys. Rev. D **52**, 2783 (1995).

[12] J. G. Korner and G. A. Schuler, Z. Phys. C **38**, 511 (1988) [Erratum-ibid. C **41**, 690 (1989)].

[13] F. J. Gilman and R. L. Singleton, Phys. Rev. D **41**, 142 (1990).

[14] J. M. Flynn and C. T. Sachrajda, Adv. Ser. Direct. High Energy Phys. **15**, 402 (1998).

[15] V. Lubicz, G. Martinelli and C. T. Sachrajda, Nucl. Phys. B **356**, 301 (1991).

[16] C. R. Allton *et al.* [APE Collaboration], Phys. Lett. B **345**, 513 (1995).

[17] J. Nieves [UKQCD Collaboration], Nucl. Phys. Proc. Suppl. **42**, 431 (1995).

[18] A. Abada *et al.*, Nucl. Phys. B **416**, 675 (1994).

[19] P. Ball, V. M. Braun, H. G. Dosch and M. Neubert, Phys. Lett. B **259**, 481 (1991).

[20] J. M. Link *et al.* [FOCUS Collaboration], Phys. Lett. B **544**, 89 (2002).

[21] M. Adamovich *et al.* [BEATRICE Collaboration], Eur. Phys. J. C **6**, 35 (1999).

[22] E. M. Aitala *et al.* [E791 Collaboration], Phys. Lett. B **440**, 435 (1998).

[23] R. Zaliznyak [E791 Collaboration], *Prepared for 9th Annual Divisional Meeting (DPF 96) of the Division of Particles and Fields of the American Physical Society, Minneapolis, Minnesota, 11-15 Aug 1996.*

[24] P. L. Frabetti *et al.* [E687 Collaboration], Phys. Lett. B **307**, 262 (1993).

[25] K. Kodama *et al.* [E653 Collaboration], Phys. Lett. B **286**, 187 (1992).

[26] J. C. Anjos *et al.*, Phys. Rev. Lett. **65**, 2630 (1990).

[27] J. M. Link *et al.* [FOCUS Collaboration], Phys. Lett. B **535**, 43 (2002).

[28] P. L. Frabetti *et al.* [E-687 Collaboration], Nucl. Instrum. Meth. A **320**, 519 (1992).

[29] J. M. Link *et al.* [FOCUS Collaboration], Nucl. Instrum. Meth. A **516**, 364 (2004).

[30] J. M. Link *et al.* [FOCUS Collaboration], Nucl. Instrum. Meth. A **484**, 270 (2002).

[31] S. Bianco, *The Upgraded Outer EM calorimeter of FOCUS at Fermilab* (1999) [arXiv:hep-ex/9912066].

[32] L. Cinquini, J. P. Cumalat, E. Erdos, B. O'Reilly and E. Vaandering, *A Description of the Inner Electromagnetic Calorimeter for FOCUS*, http://www-hep.colorado.edu/∼focus/ie/ie.html

[33] G. Bonomi, *An iron/scintillator tile calorimeter for the FOCUS experiment at Fermilab*, *Prepared for Calorimetry in high energy physics. Proceedings, 7th International Conference, Tucson, USA, November 9-14, 1997.*

[34] G. Boca *et al.*, Nucl. Instrum. Meth. A **409**, 561 (1998).

[35] A. Kreymer and F. Prelz, "*DAQ architecture for E831*", FOCUS memo, http://www-focus.fnal.gov/papers/daq_main/daq_main/daq_main.html.

[36] J. M. Link *et al.* [FOCUS Collaboration], Nucl. Instrum. Meth. A **484**, 174 (2002).

[37] G. A. Akopdzhanov *et al.*, Nucl. Instrum. Meth. **140**, 441 (1977)

[38] D. M. Schmidt, R. J. Morrison and M. S. Witherell, Nucl. Instrum. Meth. A **328**, 547 (1993).

[39] S. Eidelman *et al.* [Particle Data Group Collaboration], Phys. Lett. B **592**, 1 (2004).

[40] B. Aubert *et al.* [BABAR Collaboration], arXiv:hep-ex/0408088.

[41] M. Neubert, arXiv:hep-ph/9610385.

[42] J. M. Link *et al.* [FOCUS Collaboration], Phys. Lett. B **537**, 192 (2002).

[43] J. M. Link *et al.* [Focus Collaboration], Phys. Lett. B **541**, 243 (2002).

[44] A. Bean *et al.* [CLEO Collaboration], Phys. Lett. B **317**, 647 (1993).

[45] K. Y. Gao *et al.* [CLEO Collaboration], arXiv:hep-ex/0408077.

[46] J. M. Link *et al.* [FOCUS Collaboration], arXiv:hep-ex/0410037.

Appendix A

D^* Cone

Let's consider a semileptonic decay $D \to X\nu$, where X is the collection of particles reconstructed in the final state, including a charged lepton ℓ^+. If the D meson comes from the decay $D^{*+} \to D^0\pi^+$, it is possible to evaluate the value of $q^2 = (p_\ell + p_\nu)$. The method, called "D^* cone", does not provide the exact solution for q^2 , but the best hypothesis for its value based on a χ^2 arbitration.

In the equations of this appendix, the quantities of π^{soft} will be labeled $\tilde{\pi}$ for convenience. By applying energy–momentum conservation we find an expression that relates the D^0 momentum and the angle between the π^{soft} and the D^0 direction:

$$\begin{aligned} p^2_{D^*} &= (p^2_D + p^2_{\tilde{\pi}}) \\ m^2_{D^*} &= m^2_D + m^2_{\tilde{\pi}} + 2(E_{\tilde{\pi}}E_D - |\vec{p}_{\tilde{\pi}}| \cdot |\vec{p}_D| \cos\theta) \\ \cos\theta &= \frac{1}{2|\vec{p}_{\tilde{\pi}}||\vec{p}_D|}(m^2_D + m^2_{\tilde{\pi}} + 2E_{\tilde{\pi}}E_D - m^2_{D^*}) \end{aligned} \tag{A.1}$$

In Fig. A.1 we show a schematic of the event in the X rest frame, which for the decay mode studied in this thesis is the $K^*\mu$ rest frame [1] . Let's define the z axis along the π^{soft} direction. This way θ is the polar angle. In this reference frame the D^0 and

[1] For the D^* cone method it is not necessary to know whether the $\overline{K}^0\pi^-$system is in fact in the $K^*(892)^-$ state or not. The sum of all the reconstructed particles in the final state is what really is used, without assumption on the resonant state.

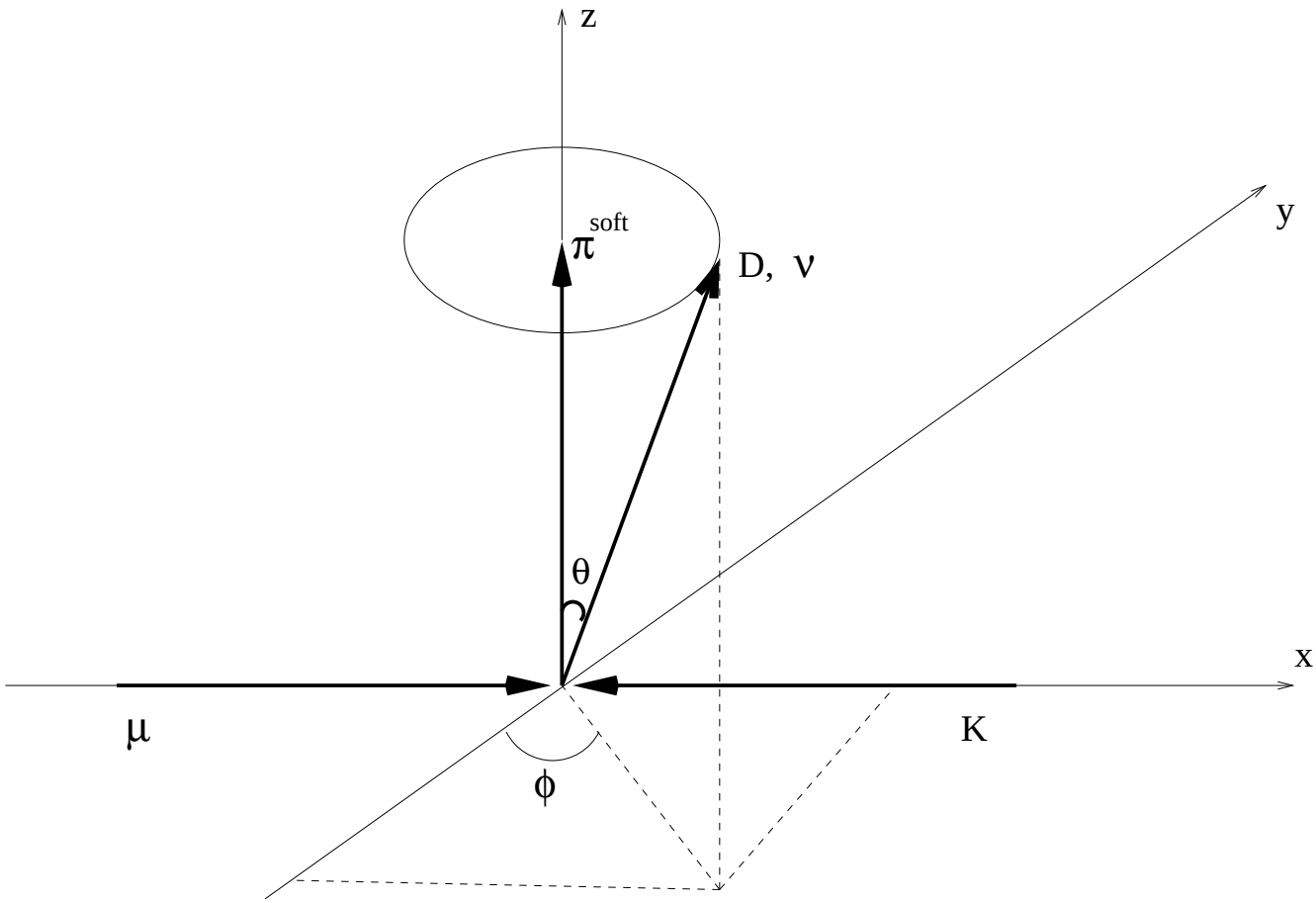

Figure A.1: A schematic for the D^* cone method is shown. In the $K^*\mu$ rest frame, $p_D = p_\nu$, and the angle θ between the D^0 and ν direction is determined. The Φ angle is not known, and the possible solutions lie on a cone.

the neutrino momenta are the same. It holds:

$$\begin{aligned} p_D^2 &= (p_{K\mu} + p_\nu)^2 \\ m_D^2 &= m_{K\mu}^2 + 2M_{K\mu}|\vec{p}_\nu| \\ |\vec{p}_\nu| = |\vec{p}_D| &= \frac{m_D^2 - m_{K\mu}^2}{2m_{K\mu}} \end{aligned} \tag{A.2}$$

Using the nominal mass of the D^* and D^0 mesons, and the reconstructed π^{soft} momentum, the magnitude of the D^0 (and neutrino) momentum and $\cos\theta$ are determined from Eq. A.1 and A.2. The angle ϕ is not determined though, so the possible solutions are infinite. The set of possible solutions lies on a cone, hence the name of the algorithm.

The momentum is evaluated by boosting a given solution [2] (corresponding to one value for the angle Φ) in the laboratory frame and comparing the direction of flight of the D^0 given by this solution to the line connecting the primary and secondary vertices previously reconstructed. The χ^2 between the two directions is used for arbitration. This way the best hypothesis for the neutrino momentum is found and the corresponding best hypothesis for q^2 is calculated. As stated before, this method is based on assuming the nominal mass for the D^0 and the D^* mesons, therefore it cannot be used to calculate the mass difference $\Delta M = m_D^* - m_D$.

[2] The algorithm uses 1000 Φ values equally spaced in the 2π range.

Appendix B

Neutrino Closure

Although the neutrino is not detected, the D^0 momentum in semileptonic decays can be calculated up to a two–fold ambiguity by imposing energy–momentum conservation. Let p_D be the D^0 momentum, p_ν be the neutrino momentum, and $p_{K\mu}$ be the four momentum of the detected particles in the final state, $p_{K\mu} = p(K^*) + p(\mu)$. Then it holds:

$$\begin{aligned} p_\nu &= p_D - p_{K\mu} \\ p_\nu^2 &= (p_D - p_{K\mu})^2 \\ m_\nu^2 &= m_D^2 + m_{K\mu}^2 - 2p_D \cdot p_{K\mu} \end{aligned}$$

Defining ρ as the magnitude of the D^0 three–momentum, and $\hat{p}_D$ its direction, we have:

$$\begin{aligned} m_\nu^2 &= m_D^2 + m_{K\mu}^2 - 2E_D E_{K\mu} + 2\rho\ \hat{p}_D \cdot \vec{p}_{K\mu} \\ E_D &= \frac{1}{2E_{K\mu}}(M^2 + 2\rho\ \hat{p}_D \cdot \vec{p}_{K\mu}) \end{aligned} \tag{B.1}$$

Where $M^2 = m_D^2 + m_{K\mu}^2 - m_\nu^2$. Eq. B.1 is a second order equation for ρ:

$$\begin{aligned} \sqrt{\rho^2 + m_D^2} &= \frac{1}{2E_{K\mu}}(M^2 + 2\rho\ \hat{p}_D \cdot \vec{p}_{K\mu}) \\ \left[\left(\frac{\hat{p}_D \cdot \vec{p}_{K\mu}}{E_{K\mu}}\right)^2 - 1\right]\rho^2 &+ \left[\frac{M^2\rho\ \hat{p}_D \cdot \vec{p}_{K\mu}}{E_{K\mu}^2}\right]\rho + \left[\left(\frac{M^2}{2E_{K\mu}}\right)^2 - m_D^2\right] = 0 \end{aligned} \tag{B.2}$$

In general solving this equation requires knowing the D^0 direction ($\hat{p}_D$). In the $K\mu$ rest frame, where $\vec{p}_{K\mu} = \vec{0}$, it is not necessary to know $\hat{p}_D$ and Eq. B.2 assumes the simple form:

$$\rho^2 = \left(\frac{M^2}{2E_{K\mu}}\right)^2 - m_D^2$$

Of the two possible solutions one is sometimes unphysical, so it can be discarded. Monte Carlo studies show that the solution that gives the lower value of ΔM is most often the real one.

Appendix C

Split Sample

We use the split sample technique in order to estimate the systematic bias on the parameter x (e.g. r_v) due to poor Monte Carlo simulation of a certain variable (e.g. the momentum). The split sample technique starts by dividing the sample into N subsamples based on the value of the variable under study, for instance into high and low momentum regions. From the subsamples we obtain N statistically independent measurements of the parameter, x_i, with their errors, σ_i. If the simulation is correct, then the only differences among the N measurements are due to statistical fluctuations.

We compute the weighted average $< x >$:

$$< x > \; = \sum_{i=1}^{N} \frac{(x_i/\sigma_i)^2}{1/\sigma_i^2}$$

and we formulate the hypothesis that the N measurements can be fit by a single parameter, the weighted average. The confidence level of the consistency hypothesis is given by a χ^2 per $(N-1)$ degrees of freedom. The χ^2 is given by:

$$\chi^2 = \sum_{i=1}^{N} \frac{(x_i - < x >)^2}{\sigma_i^2}$$

If $\chi^2/(N-1) \leq 1$, then we consider the measurements statistically consistent, and we estimate the systematic bias to be null. If $\chi^2/(N-1) > 1$, we calculate new errors σ_i' on the N measurements by scaling σ_i in the following way:

$$\sigma_i' = \sigma_i \cdot \frac{\chi^2}{N-1}$$

With this definition it automatically holds $\chi^2/(N-1) = 1$. The statistical error σ on the average is also scaled:

$$\tilde{\sigma} = \sigma\sqrt{\frac{\chi^2}{N-1}}$$

We compare the scaled error on the average, $\tilde{\sigma}$, to the statistical error that the fit reports on the whole sample, $\sigma_\circ$. If $\tilde{\sigma} < \sigma_\circ$, then we conclude that there is no systematic bias. If $\tilde{\sigma} > \sigma_\circ$, then we estimate the systematic error by subtracting in quadrature the statistical error from the scaled error on the weighted average measurements. To summarize, we have:

$$\sigma(\text{sys}) = 0 \qquad \text{for } \tilde{\sigma} < \sigma_\circ$$

$$\sigma(\text{sys}) = \sqrt{\tilde{\sigma}^2 - \sigma_\circ^2} \qquad \text{for } \tilde{\sigma} > \sigma_\circ$$

This method allows for us to separate effects due to statistical fluctuations from effects due to possible bias from poor simulation. Moreover, the algorithm is independent of the number of subsamples N, since as N increases, variance $< x^2 > - < x >^2$ also increases proportionally to N because the statistics of each sample are reduced by a factor $1/N$.